Network Formation in Mixtures of Nematic Liquid Crystal and Colloids

Julie Cleaver

Thesis submitted for the degree of Doctor of Philosophy

The University of Edinburgh

2004


EX BIBL. UNIV. EDINBURGH

Abstract

Mixtures of thermotropic liquid crystal (5CB) and colloid (polymethylmethacrylate) particles have been studied. When these composites are cooled through the isotropic-nematic (IN) phase transition an optically switchable material is formed with an unusually high storage modulus. Previous studies have shown that the particles form into an interconnected network. In this thesis the mechanism of network formation, and the morphological and mechanical properties of the network are explored.

Time-resolved laser scanning confocal microscopy (LSCM) is used to achieve near-single-particle resolution and observe the kinetics of the network formation upon cooling from the initial isotropic dispersion. As the mixture is cooled below the IN transition temperature (T_{IN}), the particles are expelled by growing droplets of nematic liquid crystal to form the walls of a three dimensional network. This process takes the order of 30 seconds (dependent upon cooling rate), but the IN transition of the pure liquid crystal is much quicker. The presence of impurities adsorbed onto the particles before they are dispersed in liquid crystal could be responsible for this. These impurities open up a biphasic region in the phase diagram and slow down interface movement. Calorimetric data are consistent with this interpretation.

Microscopy observations show that upon heating above T_{IN} single particles become free and exhibit Brownian motion. As the sample is heated deep into the isotropic phase the network is broken up but clusters of particles remain. Sedimentation of these clusters causes a density gradient of particles to form across the sample with varying height and upon cooling a new network of particles or 'clusters of particles' is formed.

Rheological measurements as a function of temperature show that upon forming the network the composite becomes much stronger than pure LC and is stress bearing. Most importantly, below T_{IN}, $G' > G''$ and the mixture is a solid - as observed macroscopically.

LSCM reveals that the network structure formed when mixtures of PMMA and 5CB are cooled through the IN transition is that of a cellular foam. This network is found to be cooling-rate and particle concentration dependent. With increasing cooling rate a decrease in cell size is observed. At high cooling rates, a hierarchical cellular structure is formed with small cells appearing within the walls and nodes of big cells. Except

for the slowest cooling rate studied the mean cell diameter is found to be inversely proportional to the weight fraction, ϕ_w, of particles present. With an increase in particle concentration the number of perforations in the cell walls decreases and the cells become more spherical in shape, with the fraction of particles in the cell edges increasing.

Similarly, preliminary rheological measurements show that the mechanical properties of the network are influenced by these factors. A decrease in G' with cooling rate is observed for all ϕ_w investigated. These values are not inconsistent with those predicted by open-cell foam theory in which the increasing degree of hierarchy present in the networks is responsible for the decrease in mechanical strength. With an increase in ϕ_w an increase in G' is observed, possibly because the cell walls begin to play a role in determining the mechanical properties.

Declaration

This thesis has been composed by myself and has not been submitted in any previous application for a degree. The work reported within was performed by me unlesss otherwise stated.

Acknowledgements

I would like to thank numerous people for their support over the last few years. If it was not for them my progress and motivation would have suffered considerably.

Firstly I would like to thank my supervisor Wilson Poon for challenging me to do the best that I could. His vital critism, enthusiasm and advice made many productive meetings and discussions.

I must thank Andy Schofield for making the colloids, without which this work would not have been possible, Andy Garrie for all his technical help and Jochen Arlt for his microscopy assistance. I am thankful to Doris Vollmer for her help and advice throughout much of my first year. I would like to thank Paul Clegg and Mike Cates for useful discussions and Paul particularly for being so approachable for advice with writing and analysis. Thanks to Lorna and Paul for proof reading.

I must thank fellow PhD students for their friendship and Lorna for making the office such a nice place to be. I am grateful to friends elsewhere that have helped me to 'switch off' and get in touch with the real world every now and again.

Special thanks to Joe who put up with me, read endless drafts, and never failed to offer support and advice.

Finally, I would like to thank my family who have encouraged and supported me all the way.

Contents

Chapter 1

Introduction

This thesis is concerned with examining the behaviour of dense suspensions of polymethylmethacrylate (PMMA) colloid particles in nematic liquid crystal 5CB. Independently, colloids and liquid crystals (LCs) have been active areas of research. The motivation for LC studies [1] has been mostly due to their applications for displays: such products include displays in watches, calculators, laptops and personal computers. Industrial applications for colloid research [2] have been equally great. Colloidal systems appear naturally in fogs and opals and have been developed commerically for use in shampoos, paints, toothpaste and food products. Areas of ongoing research include colloid polymer mixtures [3] and surfactant systems. The information gained from these colloidal systems helps the understanding of a range of other systems including molecular and biological systems.

Mixing two well understood components together is a route to making a novel third material. New and challenging physics appears which can help to further develop the understanding of the individual components. This is the case for mixtures of LC and colloids. In colloidal systems a rich variety of interaction forces are observed resulting in complex phase behaviour. If colloids are added to an anisotropic fluid rather than a simple fluid the forces and behaviour are modified and broadened. Furthermore if the

solvent is a thermotropic LC then this interaction is tunable with temperature.

Dilute dispersions of colloids in LC have been well studied recently [4]. Much effort has been made to understand how the LC is organised around the dispersed particle and how this varies with the type of LC and particle. The surface properties of the particle determine how the LC molecules order at the surface and if the anchoring energy is high enough defects can occur in the arrangement of the LC molecules. The influence of the LC on the arrangement of colloids have been investigated in order to better understand the interaction between particles dispersed in an anisotropic fluid and the resulting configuration of the LC molecules. These disruptions in the director field often result in particle expulsion. The first dense suspension in which macroscopic phase separation was not observed was studied by Poulin *et al.* [5] in which droplets of latex particles remained stable in lyotropic LC just below the transition. Later, Meeker *et al.* [6] studied a dense suspension of PMMA particles in thermotropic LC 5CB which resulted in a long lived metastable state deep into the nematic. In this state the particles formed the walls of a space spanning network, imparting surprising mechanical strength. Subsequent studies of these mixtures have attempted to determine the origin of this strength [7, 8, 9]. A literature review of particle and anisotropic solvent studies is given in greater detail in the next chapter.

Another active area of research is the effort to produce flat panel liquid crystal displays (LCDs) by industry [11, 10]. Initially, a twisted-nematic (TN) display [12, 13] was introduced, Figure 1.1, in which nematic LC is sandwiched between transparent electrodes and crossed polarisers. The LC molecules that are near the surface are aligned by surface treatments to be parallel to the surface and the two alignment layers are arranged such that the directions of alignment are perpendicular to one another. In the on state, Figure 1.1 (a), the direction of polarisation of the incident light is rotated by the LC molecules which twist round as a result of the orientation of the alignment layers; the light subsequently passes through the second polariser. In the off state, Figure 1.1 (b), a sufficiently high electric field is applied across the cell to orient the molecules

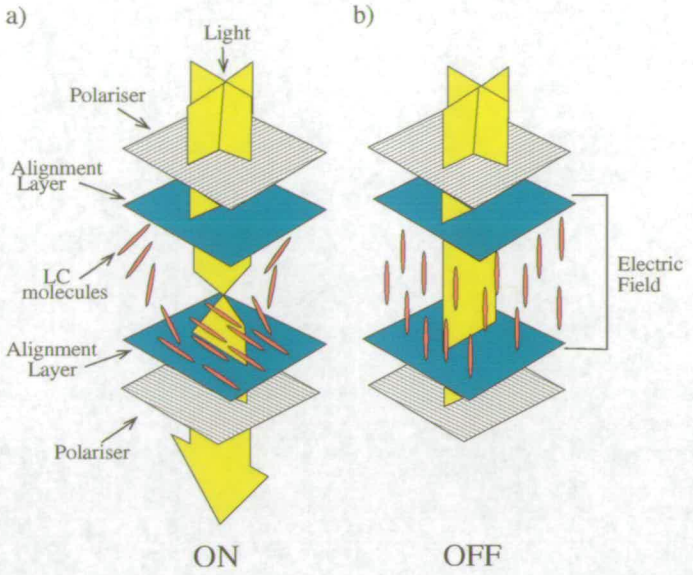

Figure 1.1: Twisted nematic liquid crystal cell. a) The on state in which the polarisation direction is rotated by the LC molecules enabling light to pass through and b) the off state in which the LC molecules align due to the applied electric field and light is blocked [10].

parallel to the axis of the cell and as a result the polarised light passes through the cell unchanged and is blocked by the second, crossed polariser. Research efforts then moved on to developing scattering devices made up of two phase systems of LC and polymer (polymer dispersed liquid crystals, PDLCs) [14, 15] or an inorganic phase [16, 17]. In both situations, Figure 1.2, misaligned domains of LC enclosed by the second phase were formed[1]. There is a mismatch between the refractive indices of the LC domains and also with the second phase and this causes incident light to be scattered, Figure 1.2 (a), and the material to appear opaque[2]. Upon application of a sufficient electric field the LC domains align and the material becomes translucent, Figure 1.2 (b). Aspirations have now extended to constructing larger and flatter displays and even flexible displays. The systems discussed so far have used rigid substrates in order to contain the LC. Recently flexible polymeric substrates have been developed for use

[1]In the inorganic system the small ($R \sim 10$nm) particles form a network and this leads to multiple, misaligned domains.

[2]Sometimes the refractive index of the second phase is matched to one of the refractive indices of the LC.

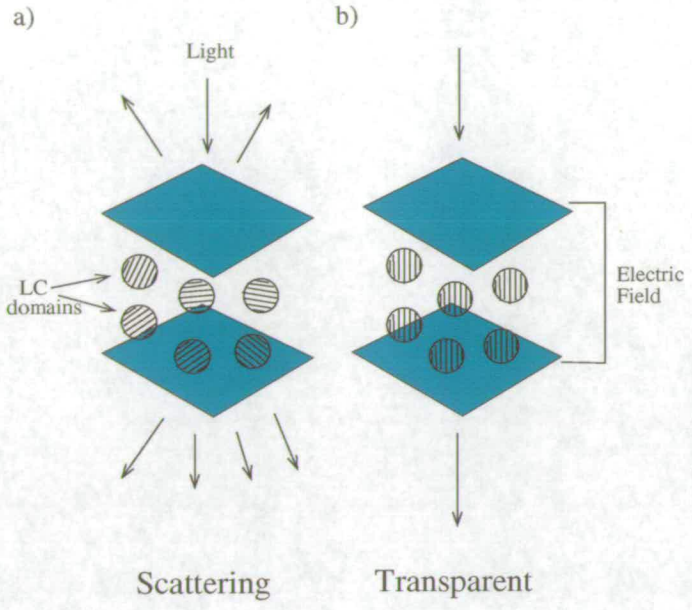

Figure 1.2: Two-phase scattering display with nematic liquid crystal. a) The scattering state in which the LC domains are randomly orientated and b) the transparent state in which the LC domains are aligned by application of an electric field [10].

with PDLCs [18, 19].

Studies have shown that the LC in the PMMA and 5CB suspensions initially investigated by Meeker *et al.* retains the optical switchable properties exploited in LCDs [20], even in this frustrated state. The mixture has been reported as a viable medium for use in TN cells [21, 22] and scattering displays [23]. This, coupled with the mechanical properties, makes these composites a realistic possibility for flexible displays. A flexible substrate can be used as an alternative to the rigid structures needed in typical LCDs. It is therefore essential to have control over the morphology of the network structure that is formed and to be able to tune the mechanical strength. In order to do this the process of network formation and the factors affecting the network structure and its strength need to be well understood.

The aims of this thesis are to explore the kinetics of the network formation in PMMA and 5CB mixtures, and to gain an insight into why a network is formed rather than ob-

serving macroscopic phase separation. The thesis then aims to examine the morphology of the network that is formed and the effects of this on the mechanical properties of the composites.

1.1 Thesis Layout

This thesis presents the results of a study of the network formation in mixtures of PMMA and 5CB. First, experiments are carried out as a function of temperature in order to study the process of network formation. Second, the mixtures are studied after cooling and the morphology and mechanical properties of the network that is formed are examined. The contents of each chapter are as follows:

Chapter 2: An introduction to colloids and liquid crystals are given independently and then a review of attempts to combine the two is presented. A literature review of studies of single particles in anisotropic solvents and the interaction between particles is given. Next an overview of dense suspensions of such mixtures is presented. The current understanding of the dense system studied in this thesis is presented and discussed.

Chapter 3: The experimental techniques used in the thesis, mainly laser scanning confocal microscopy (LSCM), differential scanning calorimetry (DSC) and rheological techniques, are introduced. The principles of these techniques are outlined and the methodology used is described.

Chapter 4: The mechanism of network formation is examined using LSCM, DSC and visual techniques. The speeds of the isotropic-nematic (IN) interfaces in these mixtures are measured from time-resolved microscopy data and these speeds are analysed and discussed alongside the thermal data. The reversibility of this process of network

formation is then investigated.

Chapter 5: The morphology of the network that is formed is imaged used LSCM and from these images and three-dimensional reconstructions of these images, it is characterised. The variation of this morphology with cooling rate and particle concentration is then investigated.

Chapter 6: Preliminary rheological measurements are made in an attempt to investigate the mechanical properties of the network. The variation of this strength with cooling rate and particle concentration are investigated. These results are then discussed alongside the morphological data extracted from the imaging study discussed in Chapter 5.

Chapter 7: The results of Chapters 4, 5 and 6 are summarised. Areas of future work arising from this thesis are discussed.

Chapter 2

Background

2.1 Introduction

This thesis is a study of mixtures of liquid crystal and colloids. Separately these have been well studied and the literature on combinations of the two is growing [24, 4]. The first two sections of this chapter discuss colloids and liquid crystals independently. The later sections review attempts to combine the two.

2.2 Colloids

Colloid systems are a part of everyday life and are an important model system for investigating equilibrium and non-equilibrium statistical physics. Such systems consist of a disperse phase (particles of solid, liquid or gas) finely distributed in a continuous phase (solid, liquid or gas) [25]. Colloid systems that we are familiar with include beer, paint, fog, smoke, milk and blood to name but a few. The dispersed components lie within the range $10^{-9} - 10^{-6}$m, ensuring that they are larger than the size of the molecules forming the dispersion medium and have a definable size and shape, and

small enough that thermal energy (Brownian motion) dominates over the effects of gravity.

Dispersed colloids are often metastable rather than in equilibrium. Attractive interactions among the particles can cause them to aggregate. In order to maintain the stability of the dispersion coulombic or steric stabilisation needs to be introduced. Coulombic stabilisation occurs if there are like charges on the surfaces of the colloids. Steric stabilisation is achieved by attaching long chain polymers to the surface of the particle, introducing a large repulsive force if two particles come into close enough range that these polymer layers overlap. The ideal hard sphere model is realised when there is no interaction between particles until they come into contact [25].

This delicate balance of forces determines the stability and usefulness of systems and understanding this is of both industrial (cosmetics, foods) and academic benefit. Colloids move consistently with the temperature and come to thermodynamic equilibrium in a similar manner to atoms and molecules. This analogy makes them ideal for probing Brownian motion and for understanding the interactions between particles [26]. As a result this area of research is both active and fruitful [3, 26, 27, 28].

The forces between colloid particles often depend on the nature of the solvent they are dispersed in. The colloids interact through an 'effective' potential which involves an average over the solvent-colloid interaction [29]. By exchanging the isotropic host for an anisotropic medium, such as liquid crystals, the interactions between the dispersed particles change significantly.

2.3 Liquid Crystals

We are all familiar with the states of matter gas, liquid and solid but what of the "fourth state of matter"? Certain materials such as liquid crystals (LCs) do not show a single transition from solid to liquid but instead show a series of transitions between new

phases with physical properties intermediate between the liquid and the crystal state. Molecules in a liquid have no long range order and are isotropically orientated, whereas in a solid the molecules are fixed on sites giving three dimensional long range order and the orientation of the molecules is fixed [30]. The partial positional and orientational ordering of the LC molecules classifies the phase of the LC [1]. These LC materials can be obtained in two ways: increasing the temperature of some crystals causes them to form intermediate LC phases before becoming liquid and these are known as thermotropic LCs. Secondly, if certain solvents are added to the crystal lattice it can be disturbed. Materials that form LC phases by altering the concentration of these solvents are called lyotropic LCs.

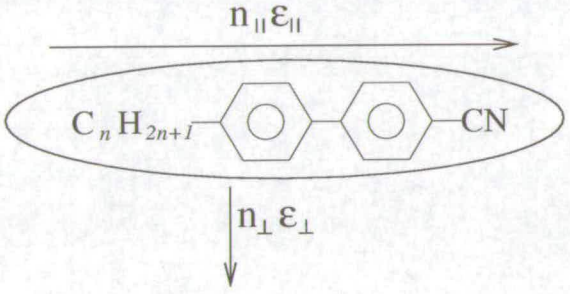

Figure 2.1: Structural formula of a rod like LC molecule - 5CB, with different optical constants parallel ($n_{||}$) and perpendicular ($n_{\perp}$) to the long axis of the molecule.

A typical liquid crystalline material is made up of anisotropic molecules; the aspect ratio is such that to a good approximation they can be modelled as rods or discs. This physical anisotropy gives the molecules the tendency to align. The molecules are optically anisotropic: a different refractive index is measured along the director of the LC ($n_{||}$) to that perpendicular to the director ($n_{\perp}$) as shown in Figure 2.1. This results in birefringence and enables textures in the LC to be observed with polarising microscopy. The dielectric anisotropy of the molecules means that they can be aligned by the application of an electric field and such electro-optical properties are exploited in liquid crystal displays.

2.3.1 The Nematic Phase

In the nematic phase the LC molecules show orientational ordering but have no positional order as shown in Figure 2.2. The centres of mass of these molecules, also known as nematogens, are disordered as in an isotropic fluid, but their long axis aligns itself parallel to an average direction. This direction that they align along is given by the nematic director $\hat{n}$ and $\hat{n}$ and $-\hat{n}$ are indistinguishable. In this phase the LC flows like a liquid but possesses anisotropic physical properties similar to that of a crystalline solid.

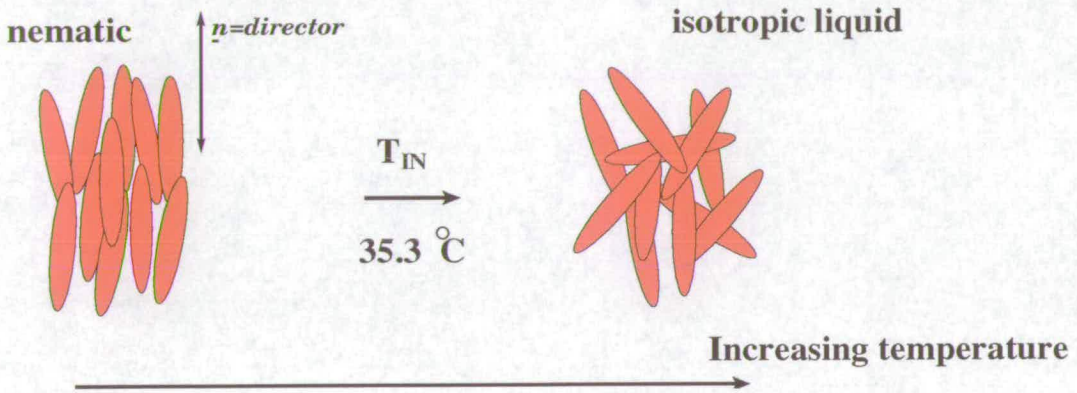

Figure 2.2: The phases of the nematic LC 5CB. The director arrow represents the average direction of the molecules. T_{IN} is the temperature of isotropic to nematic transition.

Describing the orientational order is mathematically complicated [30]. On a microscopic length scale, if the long axis of each molecule or 'rod' makes an angle θ with the director then a measure of order in the nematic phase is given by the scalar order parameter S [31]:

$$S = < \cos^2 \theta - \frac{1}{3} >, \tag{2.1}$$

where $< ... >$ denotes averaging over all molecules.

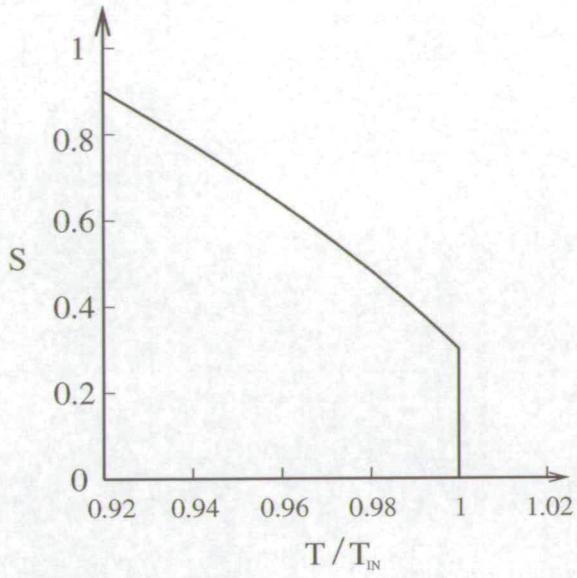

Figure 2.3: Typical variation of order parameter with temperature for a thermotropic LC. T_{IN} is the isotropic to nematic transition temperature.

For a thermotropic LC this scalar order parameter typically varies with temperature as shown in Figure 2.3 [1], where it is large deep in the nematic phase to signify order and zero in the isotropic phase to represent a disordered state.

Many of the macroscopic properties of the LC, such as the magnetic moment, are tensor properties and a tensor order parameter Q_{ij} is useful in describing their behaviour. Q_{ij} is real, symmetric and of zero trace. Choosing the z-axis parallel to the nematic axis this tensor can be defined by the scalar order parameter S and the nematic director $\hat{n}$;

$$Q_{ij} = \frac{1}{2}S(3\hat{n}_i\hat{n}_j - \delta_{ij}). \tag{2.2}$$

In this simplified view, nematic order is described on short length scales by S and on longer length scales by $\hat{n}$, which is useful in describing the elastic properties of the nematic structure.

2.4 Colloids and Liquid Crystals

Dispersing colloids in liquid crystalline materials distorts the order in the anisotropic medium and gives rise to new effective interactions between particles. As the volume fraction of colloids is increased the character of the perturbation changes. The low and high concentration cases will be described in turn.

2.4.1 Dilute Dispersions of Colloids in a Liquid Crystalline Medium

Over recent years a very good understanding has been established of the behaviour of colloids in isotropic media [26, 3]. It is of great interest to apply this experience to new and more complex situations - in this case dispersions in anisotropic media.

There have been a number of theoretical studies concerning single particle dispersions in LC [4, 32, 33, 34, 35] and the interactions introduced between the particles by the anisotropic media [36]. Experimental systems used to study these effects have usually comprised emulsions of an isotropic liquid in a thermotropic LC [37, 38, 39].

It is evident that the addition of a particle will disturb the nematic ordering in the LC and it will be energetically unfavourable. The energy cost depends upon the extent of the elastic distortion of the nematic field and this depends upon the Frank free energy of the LC (the bulk term F_b) and the anchoring energy of the LC molecules to the surface of the particle (the surface term F_s) [4, 32, 34].

The one constant approximation of the Frank free energy and the surface term add to give the free energy of the system:

$$F = F_b + F_s = \int \frac{1}{2} K[(div\hat{\mathbf{n}})^2 + (curl\widehat{\mathbf{n}})^2]d^3r - \oint \frac{1}{2} W(\hat{\mathbf{n}}.\widehat{\nu})^2 dS, \qquad (2.3)$$

where W is the anchoring energy, $\widehat{\nu}$ is the unit vector normal to the surface of the particle, K is the average Frank elastic constant of the LC and $\hat{n}$ is the nematic director. From equation 2.3 it is estimated that the surface term has a characteristic energy of the order WR^2 and the elastic cost of distortion around a single particle is $\sim KR$. A typical thermotropic LC has $K \sim 10^{-11}\text{Jm}^{-1}$ [6, 40] and so for a particle with $R \sim 1\mu\text{m}$ this elastic energy cost $\sim 2500K_BT$. Hence the elastic energies involved are large enough that configurations will remain stable against thermal fluctuations.

The dimensionless parameter:

$$\frac{WR}{K}, \tag{2.4}$$

compares the surface anchoring energy to the elastic distortion energy. When $\frac{WR}{K}$ is small the anchoring is weak in relation to the bulk deformation energy and only small distortions of the director field are expected. As the dimensionless parameter increases to 1 the crossover from weak to strong anchoring occurs and the energy cost for the director to deviate from the anchoring alignment at the surface of the particle is high. Hence large distortions of the director field are expected for strong anchoring. For particles with anchoring $W \sim 10^{-6}\text{Jm}^{-2}$ the crossover point occurs when $R \sim 10\mu\text{m}$.

The orientation of the LC molecules at the particle surface determines how the director field is distorted close to the particle. When the LC molecules orient such that their principal axis is parallel to the surface of the particle this is known as planar or tangential anchoring. Homeotropic or normal anchoring occurs when the molecules align with their long axis perpendicular to the surface. In experiments this alignment can be controlled by surface treatments of the particles [38].

The director field is aligned at large distances and at the surface of the particle. The system can be forced to respond to these alignments by forming topological defects (this is where the order of the LC and the continuity of **n** breaks down [35]).

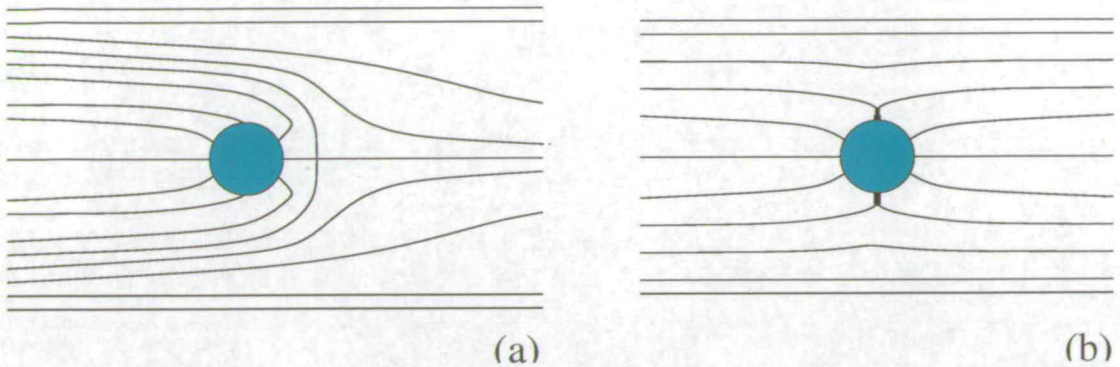

Figure 2.4: Schematic of the director field around a single spherical particle with homeotropic anchoring in a uniform nematic matrix. In the case of strong anchoring there are two possibilities: a) the dipolar structure with a satellite monopole defect and b) the quadrupolar disclination ring.

The case of homeotropic anchoring: when strong anchoring occurs ($\frac{WR}{K} >> 1$) topological defects are formed. Figure 2.4 shows the possible forms that the LC director field can take in this regime. One possibility is that a hyperbolic hedgehog point defect occurs forming a dipolar structure with the particle (a) in Figure 2.4). This defect has been commonly observed in experiments [37, 38]. The other possibility is the *Saturn-ring* configuration (b) in Figure 2.4), where a disclination ring encircles the spherical particle at it's equator. However, this has been found to have a higher energy and the dipolar structure is the preferred one [41].

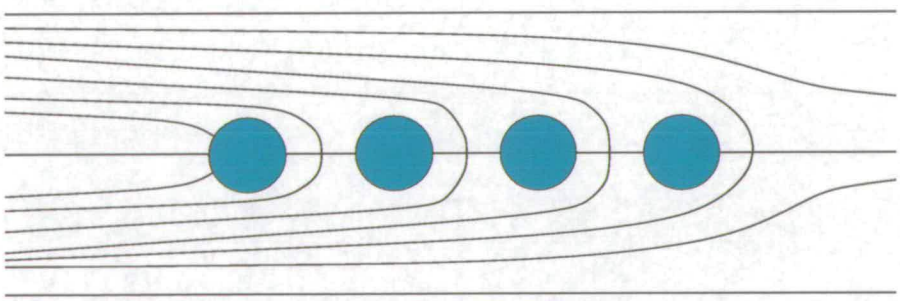

Figure 2.5: Schematic of the director field for a chain of droplets formed by interaction between the topological dipoles.

These elastic distortions of the director field cause strong anisotropic elastic interac-

tions between particles. Measurements and predictions show a long range attractive interaction between the particles [38, 39, 36, 32]. When multiple particles form a dipole configuration the defect stabilises the particles and prevents coalescence, causing the particles to align in chains [38] as shown in Figure 2.5.

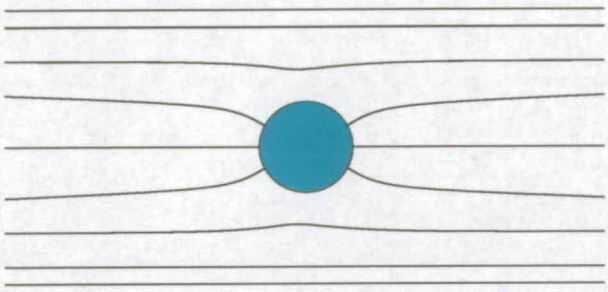

Figure 2.6: Schematic of the director field around a single spherical particle with homeotropic anchoring in a uniform nematic matrix. In the case of weak anchoring the director field has quadrupolar symmetry but does not have topological singularities.

In the regime of weak anchoring ($\frac{WR}{K} << 1$) only small perturbations to the director field are expected as shown in Figure 2.6. The director field has quadrupolar symmetry but no topological defects.

In the case of planar anchoring a pair of topological defects, known as boojums, are observed at the poles of the particles [38, 4], Figure 2.7 a). Interactions between particles in this configuration cause the particles to align along a line that makes an angle of 30°with the director, shown schematically in Figure 2.7 b) [36, 38].

Experimentally, water droplets have been dispersed in nematic LC by shaking. The particles are randomly distributed in the isotropic phase but show different configurations in the nematic phase, enabling these defect structures and particle interactions to be observed and studied [37, 38, 39].

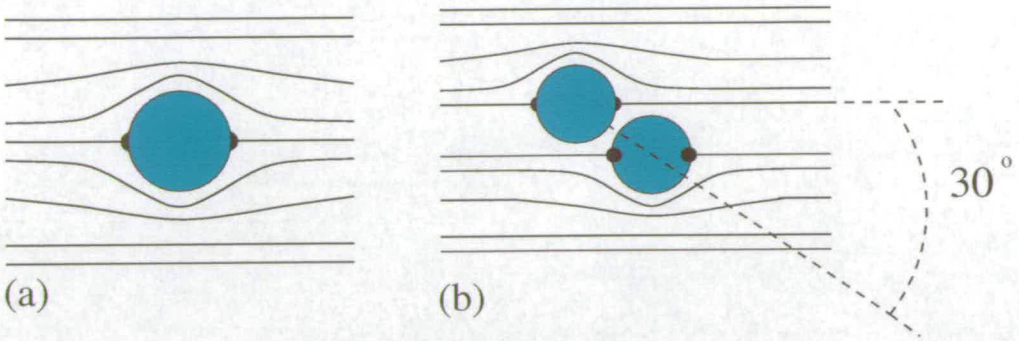

Figure 2.7: a) Schematic of the director field formed around a particle with planar anchoring conditions. Two surface defects, called boojums are formed on the surface of the particle. b) Schematic of the director field and interaction between two particles with planar anchoring conditions. The particles align at an angle of 30°to the director.

2.4.2 Dense Suspensions of Colloids in a Liquid Crystalline Medium

Over recent years there has been a steady progression toward the creation of new composite materials by dispersing significant amounts of colloids in LC.

This began with attempts to disperse finite volume fractions of particles in LC. Often this results in particle expulsion or particle coagulation because of the energy cost of disrupting the alignment of the LC molecules with the director. When isotropic and nematic phases coexist, particles are expelled into the isotropic phase to reduce the free energy, resulting in phase separation into a particle rich isotropic phase and a particle poor nematic phase [5, 42].

By using a lyotropic LC rather than a thermotropic LC the Frank elastic constant and hence the elastic energy cost of adding a particle can be reduced and phase separation on the macroscopic scale can be avoided [5, 43]. Poulin *et al.* [5] dispersed $R = 30$nm latex particles in lyotropic LC and observed homogeneous distribution in the nematic phase close to T_{IN}. But further reduction of temperature, and increase in order parameter, (see Figure 2.3) saw the particles aggregate, in order to minimise the elastic

distortion. In the same study, $R = 60$nm particles were expelled from the nematic phase; this could be attributed to the larger particle size and stronger anchoring (Equation 2.4) and therefore the greater distortion of the director field (compare Figures 2.4 and 2.6). Later, Raghunathan and co-workers [43] dispersed up to 10% by weight (ϕ_w) of $R = 60$nm particles without expulsion and they were unable to align the LC with $\phi_w \gtrsim 2\%$ of particles, suggesting a change in the rheological properties of the mixture. However the authors point out that they tried many LCs and types of latex and only this combination did not result in expulsion. A surfactant and thermotropic LC system that forms micelles with $R \sim$2nm phase separates into an isotropic micelle-rich phase and nematic micelle-poor phase [44, 42].

More recent studies of dispersed particles in LC's have shown that macroscopic phase separation can be avoided and that instead, a range of different configurations can result. The behaviour of platelets in nematic LC has been studied and stacking behaviour was observed [45]. Up to 3% volume fraction dispersions of silicone oil droplets [46] in nematic LC did not phase separate but formed highly ordered arrays of chains [46, 47]. When silica particles with $R \sim 1\mu$m ($\phi_w = 0.2\%$) were dispersed in isotropic LC and quenched into the cholesteric phase the particles stabilised the network of defects formed in the LC. An increase in the elasticity by up to a factor of four from that of the pure LC was observed [48]. Up to 4% of $R \sim$4nm silica particles when dispersed in nematic LC formed aggregates which formed a loosely connected network [16], introducing new possibilites for scattering displays [49]. The possible effects of an anisotropic medium [50] were shown when 31.5% of $R \sim 5\mu$m anisotropic zeolite particles were added to a nematic LC and rheological measurements revealed a dramatic difference between the isotropic and nematic phases.

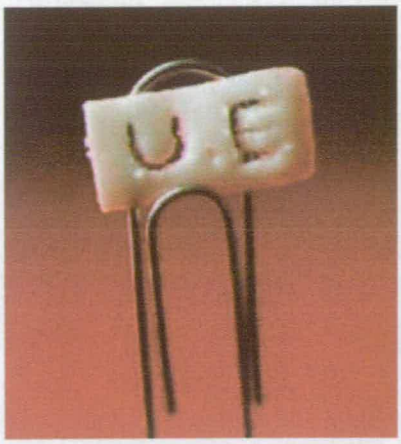

Figure 2.8: A slice of ϕ = 20% composite at room temperature. Taken from [6].

2.4.3 PMMA and Nematic LC Mixtures

Meeker *et al.* [6] succeeded in dispersing up to 20% volume fraction(ϕ) of larger (R ~250nm) particles in thermotropic nematic LC without observing macroscopic phase separation. Upon cooling into the nematic phase an opaque, waxy soft solid (see Figure 2.8) comprising a metastable network of particles was formed with an unexpectedly high storage modulus ($G' \sim 10^5$Pa). The polymethylmethacrylate (PMMA) particles involved were sterically stabilised so that homeotropic anchoring of the LC molecules is expected in the nematic phase. Typical parameters for W and K give $\frac{WR}{K} \sim 0.02$, in the regime of weak anchoring [7, 6, 40].

In this frustrated nematic state the LC retains its switchable optical properties [21, 20] and the composite has been investigated as a possibility for significantly less complicated display manufacturing than that of current LC displays [23, 22].

The birefringent nature of the LC makes bright field microscopy of these mixtures possible only in the isotropic phase, but observations suggest that as the sample is cooled from the isotropic into the nematic phase the particles are expelled from the growing nematic domains, Figure 2.9, to form the network [6].

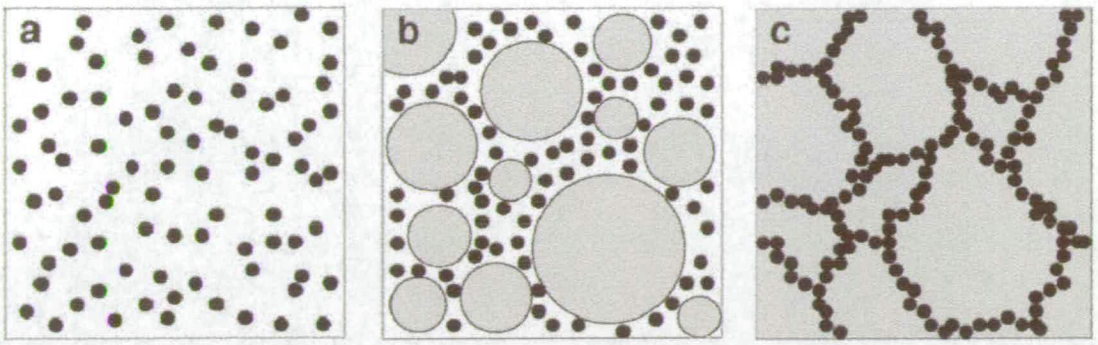

Figure 2.9: The suggested stages of formation of the network morphology. The black dots represent the PMMA particles, the grey represents nematic LC and the isotropic LC is shown as white. Taken from [6].

Reflection confocal microscopy [7] shows that, after cooling a cellular structure of very thin but densely packed particle interfaces surrounding pure nematic domains (of dimension l) is formed. A $\frac{1}{\phi}$ dependence of l is obtained from imaging [7], however this is based upon a two dimensional slice of the network rather than three dimensional information. With increasing colloid concentration a decrease in T_{IN} and broadening of the transition is observed. This is as expected for impurities in LC [51], however the particles are approximately two orders of magnitude larger than typical impurites.

It is proposed [8] that the mechanical rigidity originates from the high effective surface tension (γ) of the particle interfaces and that two contributing factors create this surface tension (see Figure 2.10):

a) LC trapped between the close packed particles in the walls is frustrated and assumed to be isotropic, causing a local increase in energy density.

b) The imbalance in thermodynamic free energy densities of the nematic in the cells and the isotropic in the walls induces an effective pressure on the walls ΔF_n. This acts from cells on either side to compress the walls and increase the particle concentration.

The contribution from the melted nematic gives a linear dependence of G' on ϕ and $\frac{T}{T_{IN}}$ and the second term gives a $\frac{1}{R^2}$ dependence. At 15° below the measured T_{IN} of

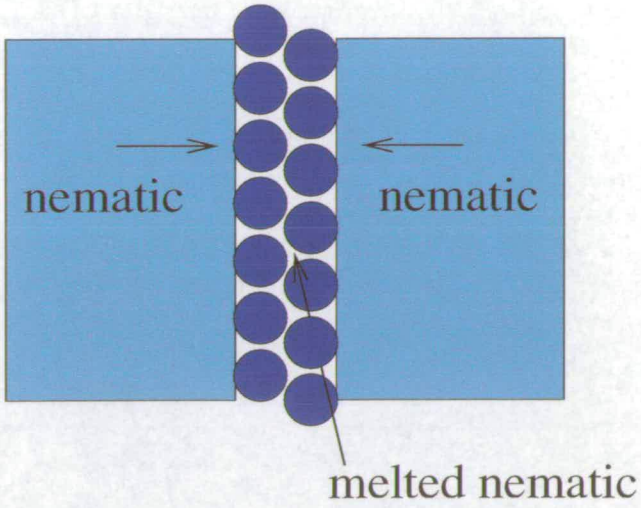

Figure 2.10: Schematic of the particle interfaces. LC between the closed packed particles is melted and the surrounding domains are nematic.

the composite and for particles with $R \sim$150nm this gives;

$$G' \sim (5 \times 10^4)\phi + 10^5 \mathrm{Pa}. \tag{2.5}$$

However rheological measurements made at the same temperatures on composites of the same particle size [8] tentatively suggest a $G' \sim (2 \times 10^5)\phi$ Pa relationship.

Experimental rheological and thermal data gathered by Petrov *et al.* [9] suggests that the system undergoes two successive first order phase transitions and inspired by this they propose the following process of network formation (Figure 2.11).

Firstly, the LC undergoes the isotropic to nematic transition and growing nematic domains expel the particles. This results in particle rich isotropic regions and particle poor nematic regions. Secondly, as T continues to decrease, the growing nematic pressure on the isotropic regions causes them to compactify into the walls of the network, expelling isotropic LC into the nematic domains where it then undergoes the transition

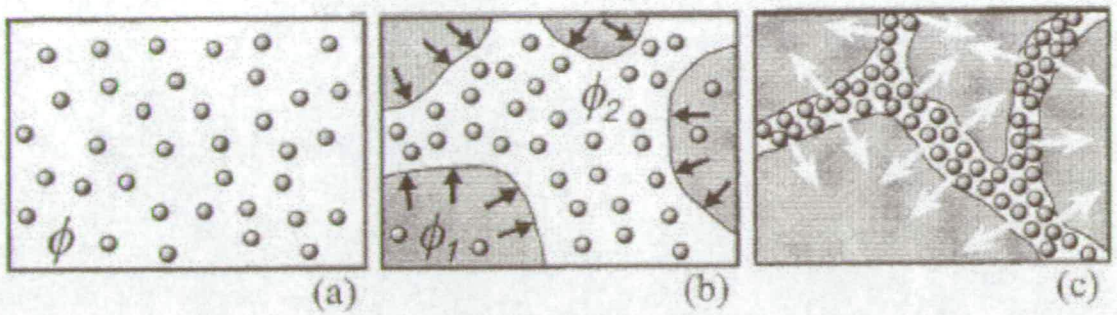

Figure 2.11: Schematic representation of the phase behaviour of the LC colloid upon cooling: a) evenly dispersed particles in isotropic LC ($T > T_{IN}$); b) intermediate state of the phase-separated system; black arrows denote the "nematic pressure" exerted by the liquid crystalline fraction (shaded areas) on the more concentrated colloid regions; c) lower temperatures and respectively higher "nematic pressure" cause the swollen wall structure to collapse and release of the remaining mesogenic liquid (white arrows). Taken from [9].

into the nematic phase. However, similar thermal measurements [7] failed to reveal the same supporting features.

Although the available amount of experimental data on these composites is growing, reproducibility and agreement between results are poor. This is not unusual in the study of properties which depend on thermal history. A prediction of the network's mechanical strength has been discussed. However, the mechanism of network formation and origin of its rigidity are still a growing subject of discussion. The work reported in the remainder of this thesis is a contribution to this field.

Chapter 3

Experimental Methods

3.1 Introduction

In this chapter the experimental techniques used to study network formation in mixtures of polymethylmethacrylate (PMMA) particles and nematic liquid crystal 5CB are outlined. The multiple birefringent domains of liquid crystal (LC) cause a significant amount of scattering of the incident light making observation of the particles within these composites difficult. Fluorescent laser scanning confocal microscopy (LSCM) is used to overcome this. Differential scanning calorimetry (DSC) is used to examine the thermal properties of phase transition in these mixtures and rheological techniques are used to probe the mechanical strength of the network that is formed.

3.2 Materials

Colloids

The particles used consist of nearly monodisperse PMMA cores [52] tagged with the fluorescent molecule 7-nitrobenzo-2-oxa-1,3-diazole (NBD)[1] [53, 54]. This molecule is excited at a wavelength of $\sim$ 488nm and fluoresces at $\sim$ 525nm. The PMMA particles were sterically stabilised by chemically grafting poly-12-hydroxystearic acid (PHSA) 'hairs' onto the surface of the particles [52]. These stabilising molecules are $\sim 10 - 15$nm in length and have an anticipated molecular volume of $\sim$ 10000 Å^3 [55]. Experiments estimate that they must have a minimum packing of $\sim$ 390 Å^2 per chain to produce stable PMMA particles and most hairs have an area of ~ 200Å^2 per chain [55]. When suspended in non-aqueous solvents these particles behave as hard spheres [53]. The particle size was determined by static light scattering and particles with radius $R = 390$nm were used.

Liquid Crystal

The thermotropic LC, 5CB (pentylcyanobiphenyl), was used as purchased from Merck. Below 22.5°C 5CB is crystal; at temperatures above this it exhibits a nematic LC phase until at T_{IN} = 35.3°C it becomes an isotropic liquid [56]. The structure of a 5CB molecule and the phase sequence of 5CB are shown in Figure 3.1 a) and b) respectively.

3.3 Sample Preparation

As synthesised, the particles were dispersed in a mixture of dodecane and hexane and were then washed at least 6 times in hexane or heptane, which have lower boiling

[1]The particles were prepared by Dr Andy Schofield at the University of Edinburgh.

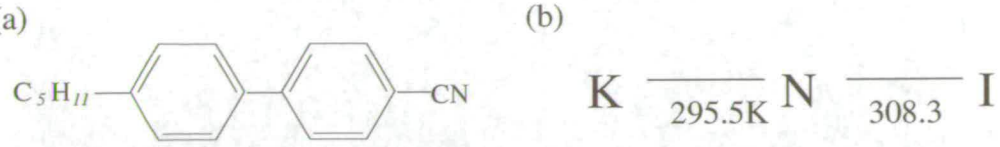

Figure 3.1: a) Molecular structure of pentylcyanobiphenyl (5CB). b) The phase sequence of 5CB : with increasing temperature the liquid crystal goes through a transition from crystal (K) to nematic (N) and then a second first order phase transition from nematic to isotropic (I).

points, to enable better solvent evaporation. The particles were then dried in a vacuum oven ($\approx 10^{-2}$ mbar) at 45°C for up to 72 hours. The dried particles were added to 5CB, at room temperature, to make up mixtures with weight fraction $\phi_w = 0.025$ to 0.15 of particles.

The mixture was heated into the isotropic phase and stored in an oven at 45°C where it was homogenised using a magnetic stirrer for at least three days prior to use. The sample was extensively shaken on a whirl mixer within the oven for at least an hour before an experiment, in order to disperse the particles in the isotropic LC.

3.3.1 Microscopy Sample Preparation

Sample cells were constructed from a microscope slide and a cover slip held apart by $\sim$ 0.3 mm spacers. The components of the cell were fixed in place with UV curing glue. A sample cell and dropper were pre-heated in an oven at 45 °C. To ensure that the sample remained in the isotropic phase the sample cell was filled within the oven. The sample was placed at the edge of the cell by the dropper and drawn into the cell by capillary force.

A Linkam LTS350 temperature stage was used with a LNP 93 liquid nitrogen cooling pump and TMS 93 temperature controller to control the sample temperature, see Figure 3.2. The sample sits on a silver plate, which has an internal platinum thermocouple and into which liquid nitrogen is pumped at a rate determined by the temperature controller.

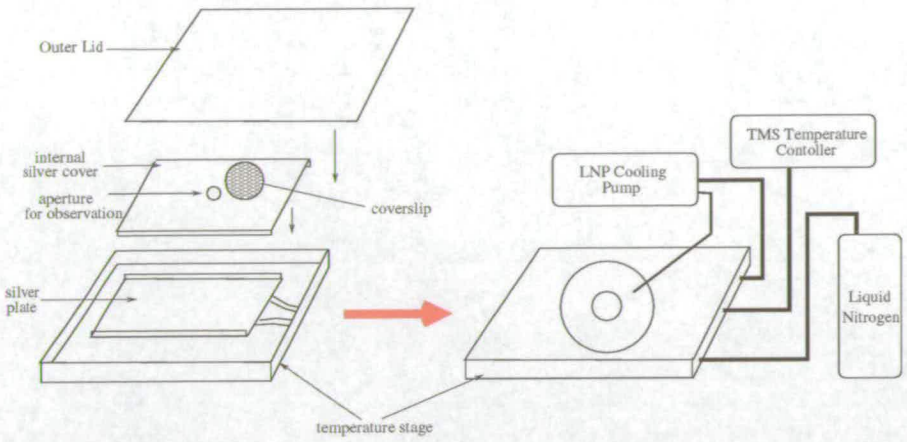

Figure 3.2: A schematic diagram of the temperature stage used to prepare microscopy samples.

A silver cover, with an aperture to enable observation, is placed over the sample to form a small 'furnace'. An outer lid is fixed in place and an outlet pipe of liquid nitrogen is placed at the window of it, to control the cooling from above the sample as well as below.

3.4 Microscopy

3.4.1 Principles of Microscopy

To resolve details on the colloidal length scale a compound microscope, made up of more than one imaging component is required [57]. In such a microscope an objective lens is used to form a real magnified image of the specimen in the primary image plane (PIP) and this image is then further magnified by the eyepiece (see dashed line in Figure 3.3).

An infinity corrected objective is designed to form an image at at an infinite distance. If such an objective is used a parallel beam of light is formed behind the objective (shown as the solid line in Figure 3.3) and a tube lens is necessary to form the image at

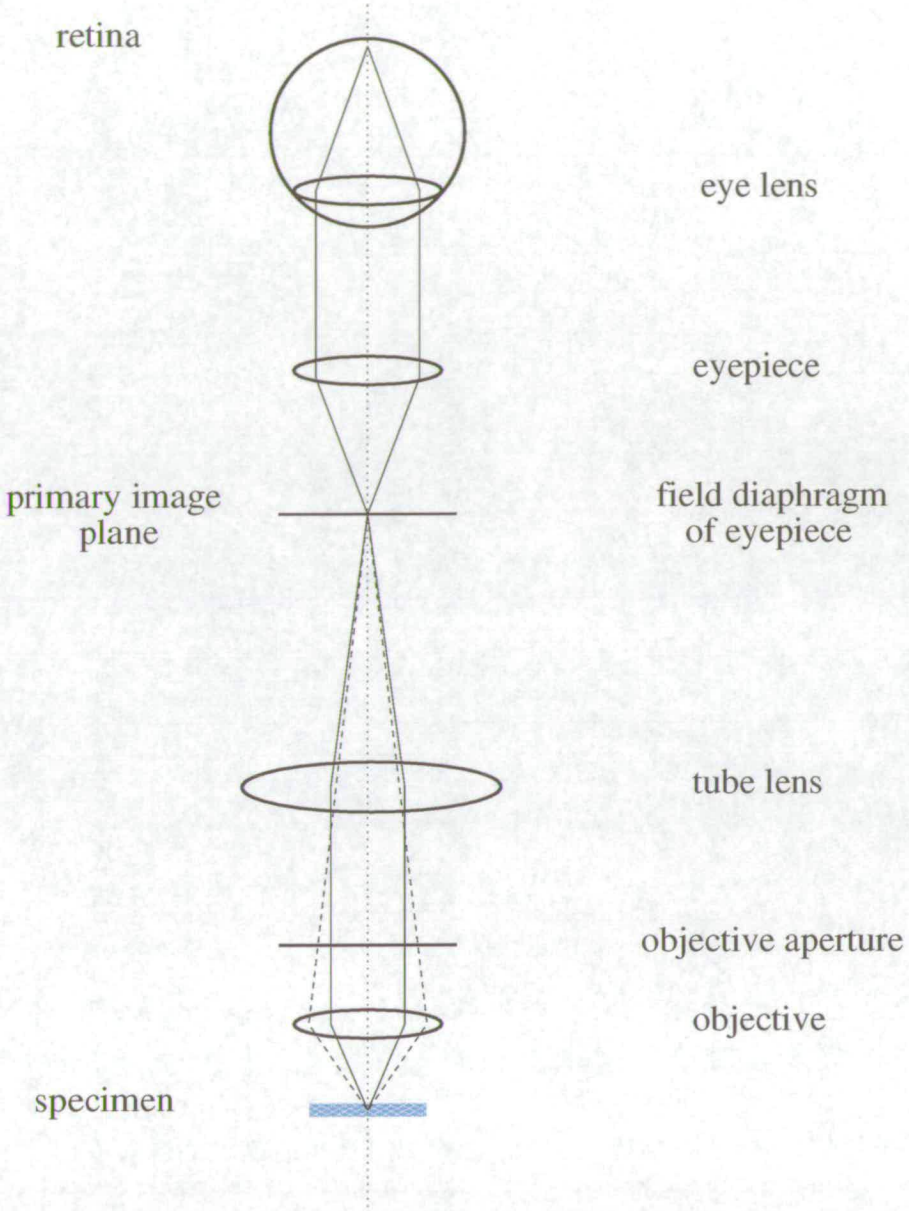

Figure 3.3: A schematic diagram of the compound microscope. In an actual micrscope each of the lenses would actually be a complex combination of lenses correct for aberrations. Two sets of rays are shown : the solid line represents the case of an infinity corrected microscope and the dashed line represents that of one that is not.

the PIP. This allows extra optical components, which require a parallel beam of light, to be added into the system without causing aberrations [58].

Each microscopy manufacturer uses a specific tube length and their objectives are added to the optical path so that the total magnification of the microscope (M_{mic}) is given by the magnifications of the objective(M_{ob}) and the eyepiece(M_{ep}) as expressed in Equation 3.1.

$$M_{mic} = M_{ob} \times M_{ep}. \tag{3.1}$$

In the case that an imaging device is used rather than the eye, then the magnification of the device's lens replaces that of the eyepiece in determining the total magnification of the microscope.

In order to obtain useful images, the contrast of the image and the level of detail that the microscope can determine must be sufficient. The magnification of the optical system must be such that it ensures that the points imaged fall upon separate pixels in the CCD camera or separate cones in the retina of the eye; otherwise they are not distinguished. Magnification beyond the point that the smallest detail distinguishable is equal to a few elements in the detector will not reveal more information. To image within these limits it is necessary to understand the relevance of the numerical aperture (NA) of the objective and resolution.

The Objective

The angular aperture (θ) as shown in Figure 3.4 is the angle that the cone of light captured by the objective makes with the vertical, and it is important in determining the scale of detail that is detected. The refractive index of the medium, n, between the objective lens and the specimen also plays a role in this. When imaging a sample through a coverslip differences in the refractive index of the glass and the medium cause light to be refracted at the interface between them. Points A and B in Figure 3.4

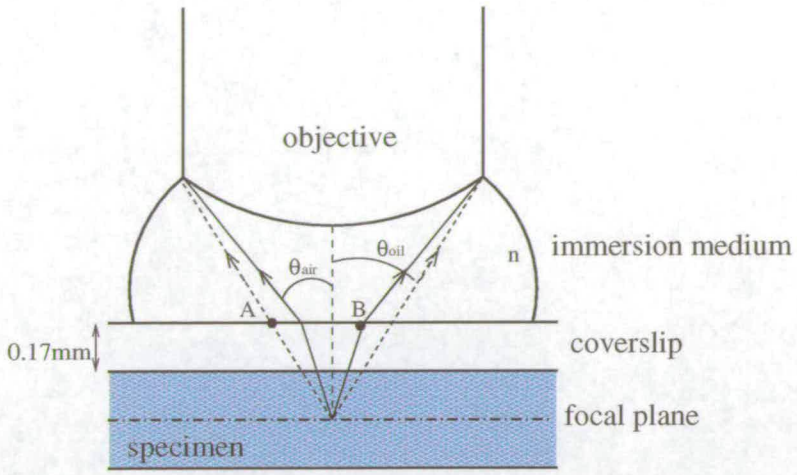

Figure 3.4: A schematic diagram of the cone of light captured by an objective. The dashed lines represent the outermost rays of the cone of light for an oil immersion objective and the solid lines these rays for a dry objective. θ_{oil} and θ_{air} are the angles between these outermost rays and the vertical for the oil and air immersion mediums respectively. A and B are the points on the interface between the glass coverslip and the medium where the outermost ray passes for oil or air respectively.

are the points that the outermost rays gathered by the objective meet the interface with oil or air respectively. The closer the refractive index of the medium to that of the glass the less a ray of light is refracted and the larger the size of the cone of light collected by the objective.

These two factors determine the numerical aperture (NA) of the objective by,

$$NA = n \sin \theta. \tag{3.2}$$

This is a measure of the system's ability to capture light and is perhaps the most important factor in determining the resolution of the objective.

Microscopy immersion oil has a refractive index $n_{oil} = 1.515$ and coverslip glass has $n_{cs} = 1.515$, maximising the light input and making the NA as high as 1.4. For

comparison the refractive index of air $n_{air} = 1$, making the maximum NA for a dry lens ~ 0.95.

Note that an objective will be depth corrected for the different refractions occuring due to the refractive index differences between the medium and the coverslip and using the incorrect thickness of glass will introduce spherical aberrations in the image.

Resolution

Resolution is the ability to discern fine details. The resolution of a microscope objective is defined as the shortest distance between two points on a specimen that can be distinguished as separate. This is diffraction limited; an aperture in an imaging system will lead to diffraction effects and the image of a pin hole will not be a point spot but instead a three dimensional diffraction pattern.

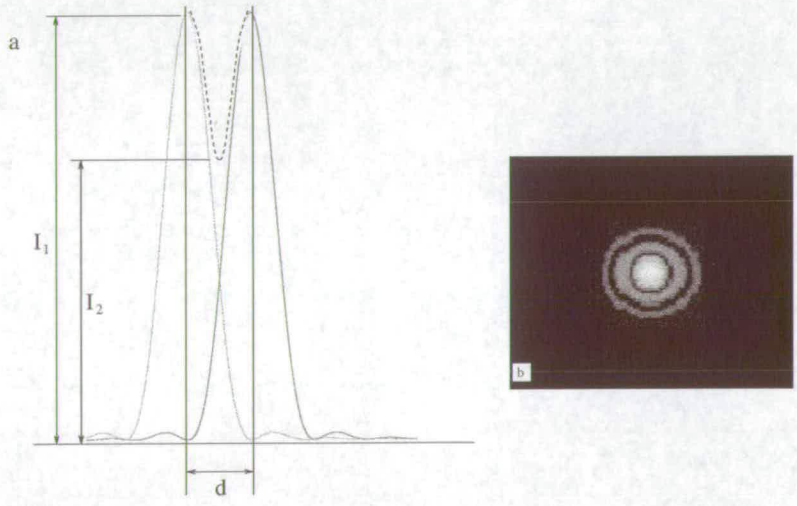

Figure 3.5: a) The PSFs of two circular lenses. These points are separated by d, which just satisfies the Rayleigh criterion and they are just resolved. The dotted line is the resultant intensity observed when the illuminating light is incoherent. I_2 is $\sim 74\%$ of I_1. Taken from [58]. b) The intensity distribution observed in the focal plane for one circular lens, known as the Airy disc. Taken from [59].

The point spread function (PSF) of a lens is the intensity pattern illuminated or observed by a lens at its focal plane [60, 57]. For a circular aperture this intensity distibu-

tion takes the form of one of the single traces shown in Figure 3.5 a). This two dimensional diffraction pattern consists of a bright circular disc surrounded by an alternating series of bright and dark higher order diffractions rings whose intensity decreases as the distance from the central disc increases, see Figure 3.5 b), called the Airy disc.

The interference of light and therefore the resulting intensity distribution differs for coherent and incoherent light: as a result the resolution of the system differs.

The limit of resolution of a microscope objective refers to its ability to distinguish between two closely spaced Airy discs in the diffraction pattern. This is defined by the **Rayleigh Criterion**:

If two points are to be resolved the dark ring of the Airy disc of one must coincide with the bright point of the other, giving an image with two bright peaks and a local minimum between them, with a dip of $\sim 26\%$.

This is demonstrated in Figure 3.5 which shows a plot of the PSFs of two incoherent point light sources separated by a distance d, which just satisfies the Rayleigh criterion. It is evident that the maximum of one Airy disc (I_1) falls at the same point as the minimum of the other. The resultant intensity of the two PSFs has a minimum (I_2) that is $\sim 74\%$ of I_1.

This pattern is dependent upon the NA of the objective and the wavelength of the light, λ. As the numerical aperture increases and the angle of the cone of light increases the central peak and diffraction rings of the Airy disc pattern decrease in diameter. This decreases the spacing necessary between objects to discern them and the resolution increases. This spacing is the radius of the first dark fringe in the PSF.

The angular aperture of the objective, the immersion medium, the coherence of and the wavelength of the illuminating light all contribute to the resolution, R, of the system:

$$R = \frac{K\lambda}{n \sin\theta} = \frac{K\lambda}{NA}, \tag{3.3}$$

where is K is a constant that depends upon the coherence of the illumination. A mathematical analysis gives $K = 0.61$ for incoherent and $K = 0.82$ for coherent illuminating light [57].

Real resolution is often lower than the theoretical limit; the better the specimen quality, the closer one can approach the theoretical limit.

Köhler Illumination

Conjugate planes are defined as planes within an optical system which are equivalent; an object placed in one of then will appear sharply imaged in each subsequent plane in that series. In the microscope there are two separate sets of conjugate planes; the 'field set' and the 'aperture set' as shown in Figure 3.6. Note that these sets are completely separate and an image in one set never appears in the other set of planes. A good knowledge of these planes is essential to achieve even illumination and hence high contrast images.

In Köhler illumination the lamp filament is conjugate to the aperture planes, so that the field set of conjugate planes will be uniformly lit.

The following steps describe how to set up a microscope for Köhler illumination which is vital for transmitted light microscopy [58, 57]:

1) Place the sample on the stage and using a low magnification objective (x10) bring the sample into focus.
2) Move the condenser until the greatest light intensity is observed in the focal plane.
3) Close down the field iris (or field diaphragm) until the edge of the illumination is visible.
4) Move the condenser until the outline of the field iris is in focus.
5) Use the centering screws on the condenser to centre this image.
6) Open up the field iris until the area of illumination is just greater than the field of

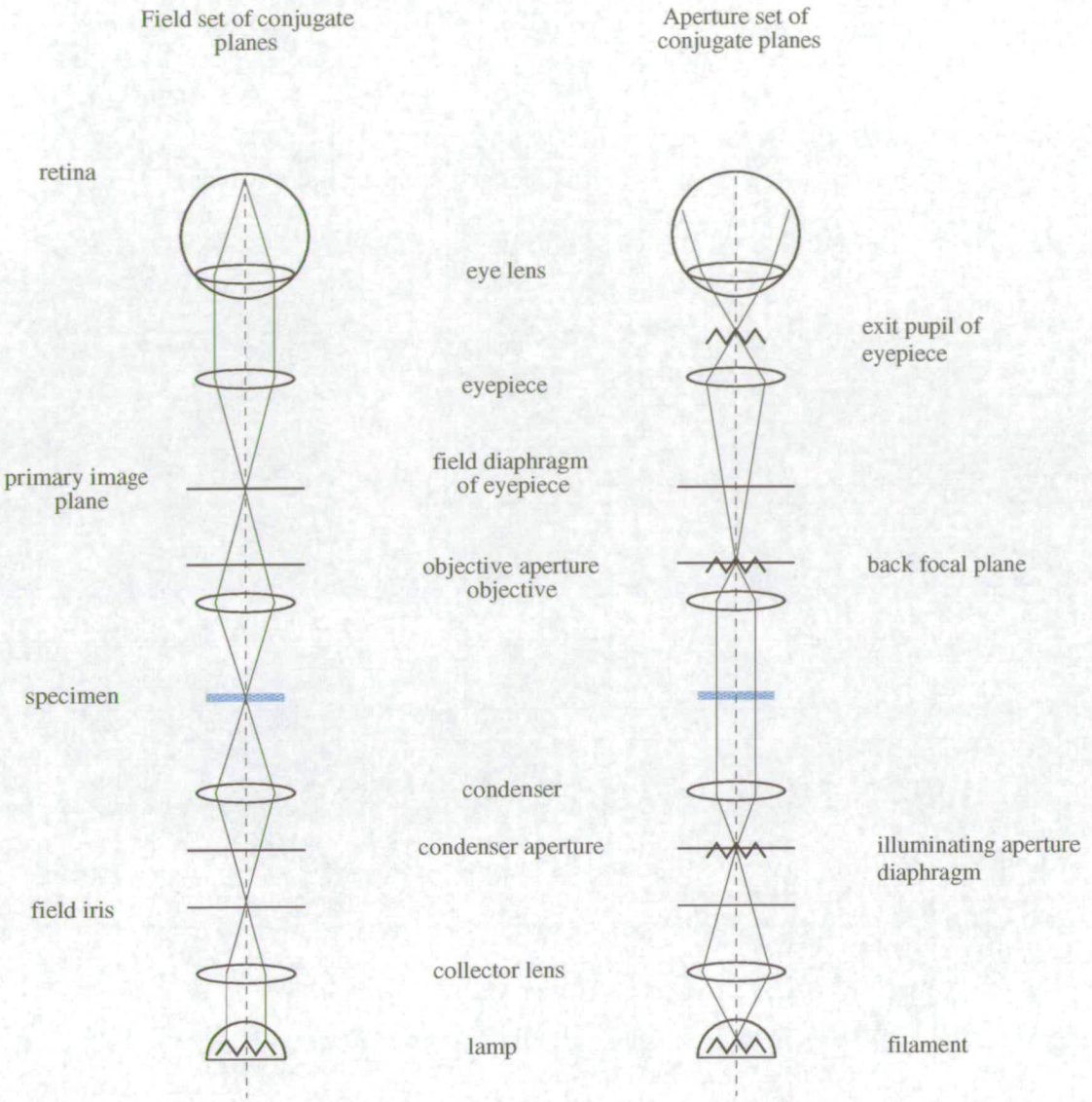

Figure 3.6: The field set (imaging rays) and aperture set (imaging rays) of conjugate planes used in Köhler illumination.

view. This controls the area of illumination in the focal plane and this is best when only the area that is under observation is illuminated [57]. This reduces stray light and glare.

7) Adjust the aperture diaphragm until the image of the specimen is sharpest: when closing it down from fully open this occurs just before the field of view goes dark. This controls the angle of the illuminating cone of light. Some of the rays will be

scattered by the sample and in order to enable the objective to collect them all the best results are obtained when the angle of the illuminating light cone is $\sim 70\%$ of that of the objective.
8) If a higher magnification objective is required the aperture diaphragm will need to be adjusted for its numerical aperture.

Optimising the illumination of the sample and choosing the correct objective can produce good quality images of the specimen at the surface of the sample, but what about deeper into the sample? In conventional microscopy light scattered from the different planes is imaged alongside the focal point and this reduces the contrast of the image. In mixtures of colloid and LC the different birefringent domains of LC cause multiple scattering and as a result observation within the sample is degraded. The use of confocal microscopy improves this contrast.

3.4.2 Confocal Microscopy

Principle of Confocal Microscopy

A confocal microscope is unique in that is allows a 'slice' from within the sample to be observed. It eliminates out of focus blur and allows the observation of three dimensonal information by non-invasive optical sectioning [60, 61].

In Figure 3.7 the confocal planes that are exploited in a confocal microscope are shown. Light from a point source (or an array of point sources) is imaged in the object and that is then imaged on a small pinhole making all points confocal. A point that is not in the focal volume may not be illuminated at all and if it is, it is unlikely that the emitted light will enter the pinhole and be detected (see dotted line), enhancing the contrast of the image.

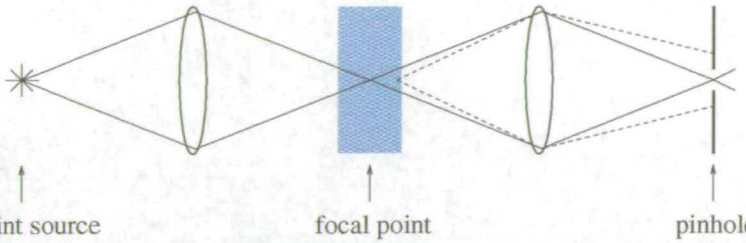

Figure 3.7: The confocal planes utilised in confocal microscopy. The solid line shows the imaging rays on the focal point and the dashed line shows the imaging of a point not within the focal volume. In the later case the light would have reduced the contrast of the image but it is blocked by the pinhole.

This improvement in image quality is illustrated in the PSF of the confocal microscope (PSF_{conf}). While in conventional microscopy the resolution is dependent on the objective, in a confocal microscope the optics used for illumination and observation determine the PSF:

$$PSF_{conf} = PSF_{obj} \times PSF_{ill}, \tag{3.4}$$

where PSF_{obj} and PSF_{ill} are the point spread functions of the objective and the illuminating optics respectively. This gives a PSF that has a sharper central peak and much smaller residual peaks as shown in Figure 3.8. These residual peaks are important when imaging bright objects near dim objects as background light is likely to be contributed and spoil the contrast; a dim object can then be resolved.

The PSF of the confocal microscope causes the resolution to be defined by the observing and illuminating optics as shown in Equation 3.5. This can be up to a factor of two smaller than the resolution of a bright field microscope [60, 62] used with the same coherence of illumination and objective.

$$R_{conf} = \frac{K\lambda}{NA_{obj} + NA_{ill}}. \tag{3.5}$$

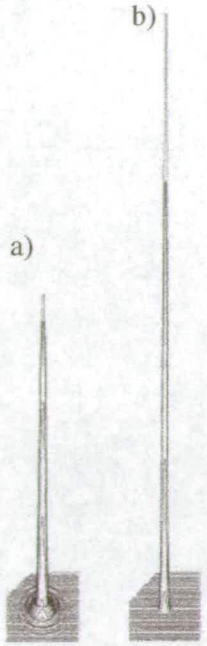

Figure 3.8: The three dimensional PSF in the focal plane for a) a conventional microscope and b) a confocal microscope. Taken from [60].

Fluorescence Microscopy

In fluorescence microscopy fluorophores are excited by the illuminating light in the plane of focus and the weaker emitted fluorescence is separated from the excitation light by a filter or dichroic mirror and brought to a focus at the confocal aperture in the PIP of the objective [63]. A dichroic mirror reflects light selectively according to its wavelength.

For use with the NBD dye that is attached to the PMMA particles a long pass filter was put in the optical path. This blocked out all wavelengths longer than 500nm, including the illuminating laser light and allowed the emitted flourescence to pass to the detector. In fluorescence microscopy the resolution is determined by the mean of the illuminating and emission wavelengths.

Laser Scanning Confocal Microscopy

In laser scanning confocal microscopy(LSCM) a focused laser beam is the light source which is rastered across the sample using scanning mirrors to deflect the beam as shown in Figure 3.9. At the focal point the specimen is illuminated and fluoresces. The emitted light is collected by the objective, passes through the dichroic mirror and is focused on the pinhole. This light then falls on the detector and this allows an image to be built up electronically point by point using software.

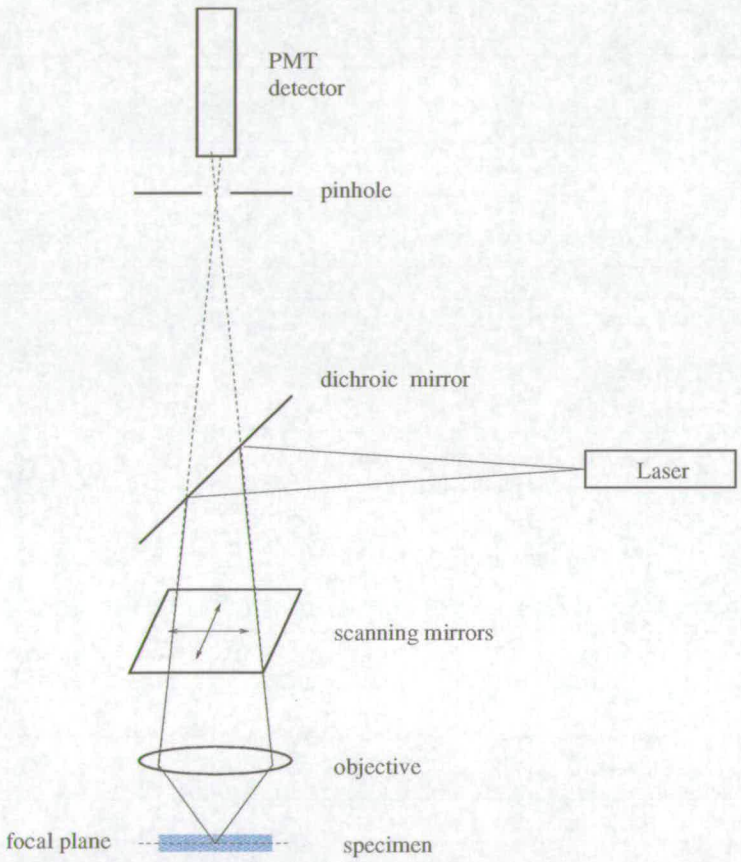

Figure 3.9: The optical system of a laser scanning confocal microscope. The solid line represents the short wavelength excitation laser light and the dashed line the longer wavelength emitted fluorescence.

In this system the objective is used for both observation and illumination and the NA plays a greater role in determining the resolution of the system.

Optical Sectioning

As shown in Figure 3.7 points not in the confocal volume will not be imaged. Points along the optical axis at different depths to the focal plane will not be imaged and this leads to optical sectioning. By moving the focal plane along the optical axis in predefined steps a stack of optical slices can be gathered and using image analysis software a three dimensional image of the sample can be constructed.

Conventional vs. Fluorescent LSCM

The network formed in a composite is imaged with bright field microscopy and fluorescent LSCM. As shown in Figure 3.10 the degredation with depth is apparent in both cases but it is considerably worse with the conventional technique.

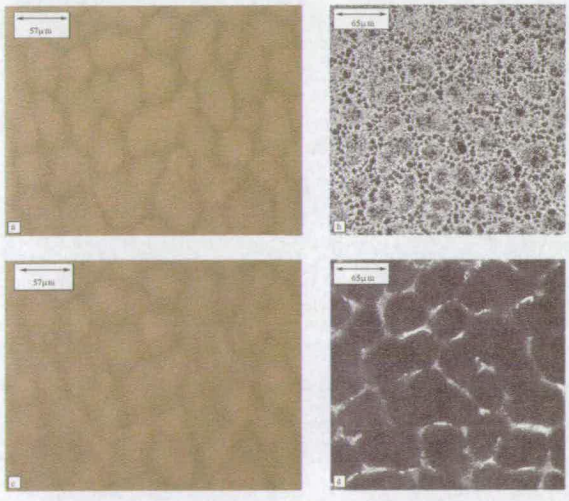

Figure 3.10: Images of $\phi_w = 0.10$, R=390nm particles with a $40\times$ lens. a) and c) using conventional bright field microscopy at the surface of the coverslip and 10μm into the sample respectively. b) Using LSCM at the coverslip and d) at 10μm into the sample respectively.

Transmitted Light Microscopy

When observed between crossed polarisers the birefringent nature of the nematic LC can be utilised to observe the kinetics of the phase transition. After setting the system up with Köhler illumination, a polariser is placed in the plane of the field iris and an analyser with its axis at 90° to that of the polariser is placed in the primary image plane. Linearly polarised light enters the sample, is unaffected by the isotropic LC and it is all blocked by the crossed analyser. However in the nematic phase the birefringent properties of the nematic domains cause the polarisation of the light to be rotated and light with a component with the same polarisation as the analyser is created. This component is allowed to pass through the analyser and a coloured texture is observed. As a result growing nematic domains are observed as light areas and the isotropic as dark.

Operated in transmission mode the original PMT (see Figure 3.9) becomes redundant and instead the transmitted scanned laser light is focused by mirrors onto a separate PMT on the other side of the sample [64]. In this case the optics for illumination and observation are different and the resolution is often degraded by the numerical aperture of the condenser (see Equation 3.5).

3.4.3 Apparatus

An upright Nikon TE300 microscope equipped with a Biorad Radiance 2000 laser scanning confocal head was used. An argon ion laser with light of wavelength 488nm was used for illumination. The highest resolution images, capable of resolving single particles, were obtained using a $\times 100$ oil-immersion objective ($NA = 1.4$). A time series of LSCM images could be gathered, and by adjusting the speed at which the sample is scanned and the sample area that is scanned the time between successive images can be adjusted. Observation between crossed polarizers and with transmitted

light was also possible in the same microscope.

3.5 Differential Scanning Calorimetry (DSC)

The thermal properties of the phase transitions in LC mixtures were studied using differential scanning calorimetry (DSC), a dynamic experimental method that measures the heat changes that occur during controlled increases (or decreases) in temperature.

3.5.1 Principles of DSC

The typical apparatus used in DSC is shown in Figure 3.11. This consists of two cells: one filled with the sample being tested and one with a reference material. These two materials must have approximately equal specific heats and the reference material must not undergo any phase transitions in the temperature range required.

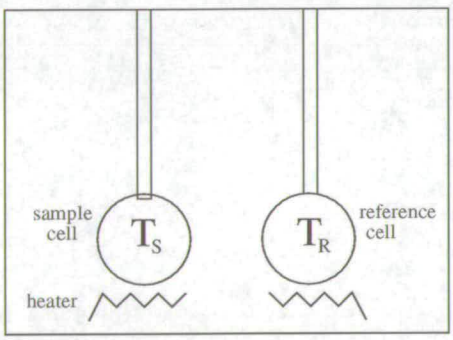

Figure 3.11: Schematic diagram of the apparatus used in DSC. T_S is the sample temperature and T_R is the temperature of the reference material.

The cells are maintained at the same temperature ($\Delta T = T_S - T_R = 0$) throughout the experiment, and are heated at a specified rate. Differences in the necessary heat flow that is supplied separately to the sample and reference cells are measured as a function of temperature [65, 66, 67].

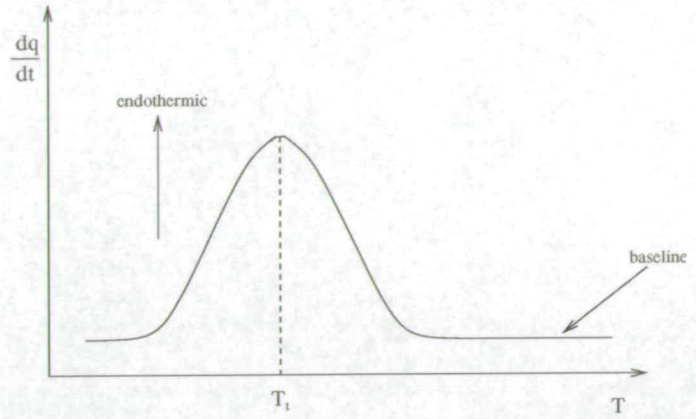

Figure 3.12: Typical DSC trace with an endothermic peak. T_t is the temperature at which the peak occurs. Taken from [65].

A typical DSC trace, as shown in Figure 3.12, is produced and deviations from the baseline in the DSC trace produced are indicative of a phase transition. The nematic to isotropic transition disrupts orientational order and is endothermic : this is characterised by an increase in the thermal energy that needs to be supplied to the sample to maintain the temperature, compared to the energy supplied to the reference material. In Figure 3.12 T_t is the temperature at which the peak in the difference in energy flow occurs, and in this thesis it is taken as the transition temperature of the composite.

3.5.2 Apparatus and Method

The measurements were made with a VP-DSC Microcalorimeter (Microcal Inc.) which has two coin shaped cells of volume 0.52ml. These are fixed in place enabling the cells to be heated accurately with an internal peltier heating mechanism. Narrow tubes allow the cells to be cleaned and filled. The cells were cleaned with toluene and then ethanol and allowed to air dry before loading the sample. The sample (in the isotropic phase) was loaded into the preheated cell using a syringe that was also heated to approximately 45°C. Generally measurements were made in the range 45 - 15°C, with a cooling rate of 6K/h and a heating rate of 30K/h. The reference material used was

water.

3.6 Rheology

Rheology or 'the science of the deformation and flow of matter' [68] is used to study how a material deforms when acted on by a force. For example it is used to understand what is happening as paint is spread or beer is poured. Dynamic rheological techniques are used to probe the mechanical properties of the network that is formed within the composites. The basic concepts of rheology and an introduction to the technique that is used are presented here.

3.6.1 Viscous and Elastic Behaviour

In the seventeenth century Newton formulated the basic laws of viscous flow in liquids and Hooke the theory of elasticity for solids [68]. Newton hypothesised that an ideal liquid flows in response to a stress and that this flow persists as long as the stress is applied : when removed the material remains altered from its original state. In the case of a Hookean solid an instantaneous deformation is observed and upon removing the stress the body returns to its original configuration.

Most materials cannot be described solely by one of these laws but simultaneously show properties that are viscous and elastic. The properties exhibited depend upon the timescale with which the material is probed : in that while they maintain their shape for a time they eventually flow. An example of this is silly putty. At short times (e.g. when it is dropped and hits a surface quickly) it rebounds unchanged, although a deformation did occur while it was in contact with the surface: this is elastic behaviour. However at long times (e.g. the putty is left to sit on the surface) it will 'flow' to spread out over the surface, thus behaving in a viscous manner.

These materials are known as viscoelastic. The characteristic timescale for the crossover in behaviour varies with material.

3.6.2 Simple Shear

Consider a force F applied to a cube of side d and area A under simple shear, as shown in Figure 3.13. The resulting shear stress σ is given by [69, 70],

$$\sigma = \frac{F}{A}. \tag{3.6}$$

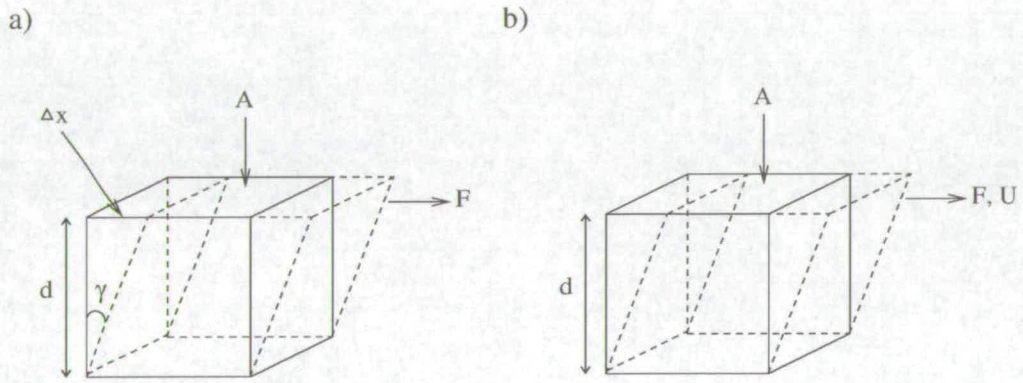

Figure 3.13: Simple shear of a cube of height d and surface area A. The solid lines represent the initial shape of the sample and the dashed line the shape when a force F is applied. Upon application of the force a) a Hookean solid exhibits a strain γ, where Δx is the displacement in the direction of shear, or b) an ideal liquid 'flows', where U is the velocity of the sample adjacent to the top plate.

One can imagine that the sample is actually a stack of slices of material. When sheared each slice is displaced by a bit more than the one below and the whole sample is distorted as shown in Figures 3.13 a) and b).

When a solid is subject to this simple shear a deformation or shear strain γ is produced as shown in Figure 3.13 a). This shear strain is related to the distortion and the thickness of the sample by,

$$\gamma = \frac{\Delta x}{d}, \tag{3.7}$$

where Δx is the displacement of the top layer along the direction of shear. Hooke proposed that this strain is proportional to the stress applied and that the constant of proportionality is G the modulus of rigidity of the material;

$$\sigma = G\gamma. \tag{3.8}$$

In the case of a newtonian fluid, such as glycerine or water, the material flows in response to the shear as shown in Figure 3.13 b). The top plate moves with constant velocity U while the bottom plate remains stationary. The top layer of the material is assumed to move with the same velocity as the upper plate. The shear rate or strain rate is defined as $\dot{\gamma}$ and in the case of uniform shear it is equal to the velocity gradient, $\frac{\Delta \dot{x}}{d}$. Therefore in the case of uniform shear,

$$\dot{\gamma} = \frac{\Delta \dot{x}}{d} = \frac{U}{d}. \tag{3.9}$$

The stress is proportional to the shear rate and the viscosity η of the liquid is the constant of proportionality;

$$\eta = \frac{\sigma}{\dot{\gamma}}. \tag{3.10}$$

A viscoelastic material responds in a more complicated way that will be dependent upon the timescales with which it is probed.

3.6.3 Oscillation

In order to investigate the viscoelastic properties of a substance an oscillatory technique can be used. A sinusoidal stress, σ, of amplitude σ_0 and frequency of oscillation ω, as shown in Equation 3.11, is applied[2].

$$\sigma(t) = \sigma_0 \sin(\omega t). \tag{3.11}$$

This amplitude σ_0 must be small enough in order not to significantly deform the material's structure. When this oscillatory stress is applied to a Newtonian fluid, the fluid exhibits a strain that is exactly 90° out of phase with the stress (refer to Equation 3.10) [69],

$$\gamma(t) = -\gamma_0 \cos(\omega t), \tag{3.12}$$

where γ_0 is the amplitude.

Alternatively for a Hookean solid the strain produced is in phase (refer to Equation 3.8),

$$\gamma(t) = \gamma_0 \sin(\omega t). \tag{3.13}$$

When a viscoelastic material is subject to a sinusoidal stress the strain will be out of phase with the stress by more than 0° and less than 90°. This is captured by the use of a frequency dependent complex shear modulus, G*.

[2]If operated in controlled-strain mode then a sinusoidal shear strain is applied instead of a sinusoidal shear stress.

In the linear viscoelastic regime, where the strain amplitude γ_o is small ($\gamma_o \ll 1$) G* is independent of the stress, or strain[3], that is applied [71, 72] and,

$$\sigma = G^*\gamma, \tag{3.14}$$

where G^* is,

$$G^* = G' + iG''. \tag{3.15}$$

Here $G'(\omega)$ is the in phase elastic component known as the elastic or storage modulus and represents the storage of elastic energy. $G''(\omega)$ is the out of phase viscous component called the viscous or loss modulus and represents the viscous dissipation of energy.

As already discussed the behaviour of the material is dependent upon the timescale at which it is probed. A typical measurement of G' and G'' as a function of frequency shows a crossover from viscous behaviour at low frequencies to elastic behaviour at high frequencies (see Figure 3.14). ω_c is the frequency at which the material makes the transition from 'solid-like' to 'liquid-like' behaviour, and it approximates to one over the characteristic relaxation time τ_c. τ_c is the longest time required for elastic structures within the material to relax [72].

A strain scan (a series of exploratory runs covering a range of strain amplitudes, γ_0) was run on the composite to determine the linear viscoelastic range (i.e. the range over which the linear relation 3.14 applies) and a strain from within this region was chosen for oscillatory measurements. As high a strain as possible should be chosen

[3]Provided the measurement is made in the linear viscoelastic region the same information is recovered whether a strain-controlled or stress-contolled method is used.

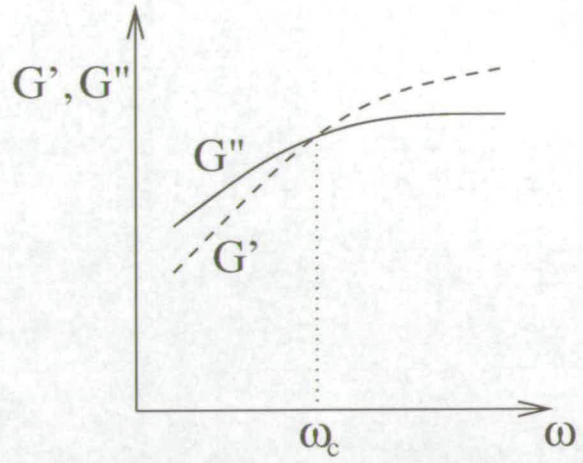

Figure 3.14: Schematic of the storage and loss moduli as a function of frequency of a typical viscoelastic material. ω_c is the characteristic frequency at which the material changes from 'liquid-like' behaviour to 'solid-like' behaviour.

to obtain less noisy data, but as low a strain as possible should be chosen to avoid damage to the network formation or cause slippage from the plates. This necessitates a compromise. For most measurements a strain of 0.5% and a frequency of 1Hz was found to be suitable for studying the response of the network.

3.6.4 Apparatus and Method

A TA CSL^2 100 Rheometer operated in controlled strain mode was used with a cone and plate geometry (see Figure 3.15). The cone, supported by an air bearing to reduce friction effects, undergoes forced harmonic oscillations about its axis. The subsequent angular displacement in the sample, which sits between the plate and the cone, is measured by an optical device. Software is used to calculate the resulting strain. The sample temperature is controlled from below by an internal Peltier plate system with a recirculated water cooling bath.

The majority of these meaurements were carried out with a 4cm 2° cone. The cone is truncated and the distance from this point to where the apex of the cone would touch

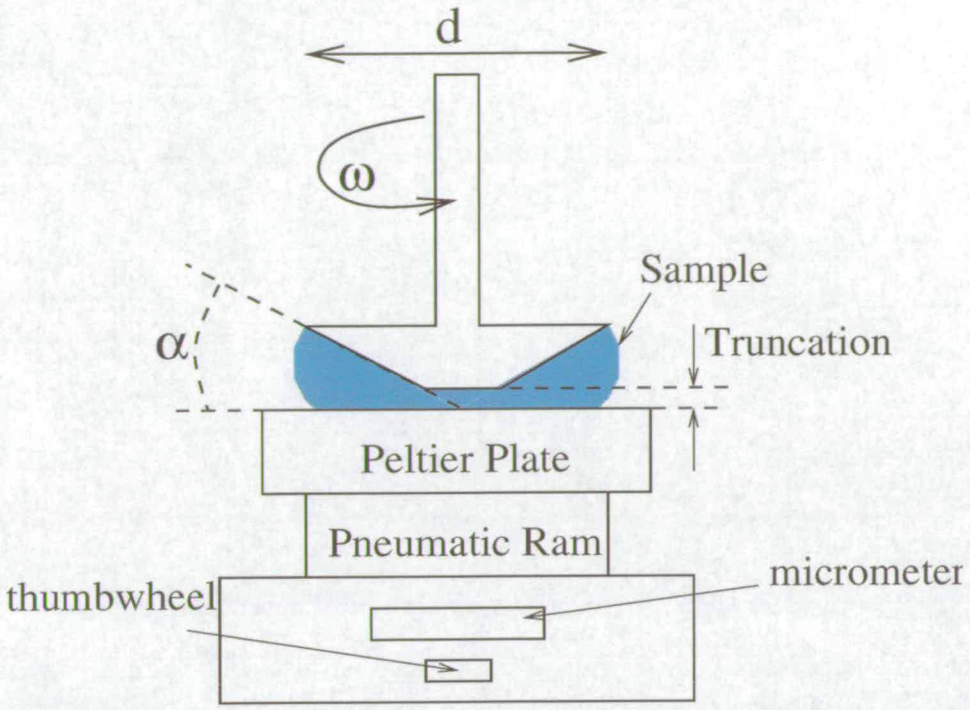

Figure 3.15: Schematic diagram showing the cone and plate geometry cone used with the rheometer. The truncation, diameter d and angle α of the cone moving with angular velocity ω are shown. Note that the angle α is shown grossly exaggerated.

the plate is known as the truncation or gap. For this cone the truncation is 49μm. A wider (6cm) cone is more sensitive to stress changes and would have been better suited to the low viscosity of the sample in the isotropic phase, however the 4cm cone was more suitable for measuring the properties of the composites in the nematic phase. The large cone also had a smaller gap (0.5°) and hence errors due to thermal expansion would have become important.

The gap between the cone and the plate was set at 20°C using a deceleration method as follows [69].

1) A small stress was applied to the cone to set it spinning slowly.

2) The plate was raised slowly by turning the micrometer thumbwheel until the cone had stopped and the micrometer reading was noted.

3) The plate was lowered and the process was repeated more slowly in order to obtain

a more acurate reading of the zero-point.

4) The gap is now set by adjusting the plate position until the micrometer reading = zero-point + truncation.

The sample was loaded as follows :

1) The rheometer was heated to 65°C and the cone was brought into contact with the plate to heat the geometry for a minimum of 5 minutes. Due to thermal expansion the plate must be lowered below the zero-point.

2) The ram was lowered, the plate temperature was lowered to 45°C, and the sample was loaded onto the plate using a preheated syringe. This was to ensure that the sample remained in the isotropic phase while loading.

3) The micrometer thumbwheel was adjusted to lower the plate to the gap setting.

4) The ram was raised and the sample (maintained at 45°C) came into contact with the preheated cone.

The sample loading had to be performed as quickly as possible to ensure that the cone did not cool below 45°C. Care needed to be taken when loading the sample to ensure that no air bubbles were present as this could seriously affect the measurements. It was also important that the sample volume, which for this geometry was ~0.5ml, was accurate. Overfilling could allow the sample to migrate onto the top of the cone and underfilling would effectively reduce the diameter of the cone; both of which would alter the measurement. The ideal sample volume is depicted schematically in Figure 3.15, in which the sample fills the available volume but does not flow out beyond the edge of the cone. To reduce errors the measurements were repeated several times.

The procedure for a sample measurement was as follows:

Measurement of G^* After Network Formation

Cooling Procedure

1) The sample was presheared at 45°C for 10 seconds. This was to remove history

effects of loading.

2) The sample equilibrated for 10 seconds: Waited for zero velocity to be reached.

3) The temperature was decreased from 45°C to 15°C in a prescribed time; this determined the cooling rate.

The sample sat for 5 minutes at 15°C.

Meaurement of G*

1) The temperature was raised to 20°C and equilibrated for 1 minute.

2) For 30 minutes 0.5% strain was applied to the sample at 1Hz.

In order to measure G* as a function of temperature the following sample procedure was used:

Measurement of G* During Network Formation

1) The sample was presheared at 45°C for 10 seconds. This was to remove history effects of loading.

2) The sample equilibrated for 10 seconds.

3) For a period of $\frac{30}{cooling\ rate}$ seconds, an oscillatory strain of amplitude 0.5% and at frequency 1Hz was applied as the sample was cooled from 45°C to 15°C at a constant rate.

A new sample was loaded for each measurement.

3.7 Summary

In this chapter the basic principles of LSCM, DSC and dynamic rheological techniques have been outlined. In the following chapters, first, time resolved microscopy, DSC and rheological techniques are used to examine the process of network formation. Next the results of microscopy and rheology studies of these network structures are presented.

Chapter 4

Network Formation

4.1 Introduction

Mixtures of sterically stabilised PMMA particles and thermotropic liquid crystal when cooled through the isotropic to nematic (IN) phase transition have been shown to form a three dimensional network of particles [6]. Microscopy images of this network structure have been shown before for the LCs 5CB and MBBA [7]. Models for the kinetics of the network formation have been proposed [6, 9]. As discussed in Chapter 2, however a direct observation of the process has still to be obtained.

In this chapter the kinetics of the network formation are examined by observing particle motion under cooling from the isotropic to the nematic phase. This was achieved using fluorescent laser scanning confocal microscopy (LSCM), allowing almost single particle resolution within the composites. The nucleation and growth of the nematic domains are observed with polarising microscopy and the thermal properties of the phase transition are studied using differential scanning calorimetry (DSC).

These techniques are further employed to examine the reversibility of this network formation process and the evolution of these mixtures with successive cooling through

the IN transition.

Finally, the mechanical properties of the composite as this network is formed are examined using oscillatory rheological techniques.

4.2 Mechanism of Network Formation

In order to observe the kinetics of the initial network formation, samples were quenched from the well mixed isotropic state at $\sim$ 50°C to room temperature while being observed under the microscope. The mixture was cooled to $\sim$ 20°C in $\sim$ 30 minutes; therefore it is estimated that the cooling rate was $\sim$ 1°C/min. A sequence of images taken during the network formation in a sample with $\phi_w = 0.10$ of $R = 390$nm particles is shown in Figure 4.1. The fluorescent particles appear as white dots and the LC as black.

Figure 4.1(a) shows an image of the mixture in the isotropic phase in which individual particles can be resolved. Individual particles and sometimes doublets and triplets of particles are observed undergoing Brownian motion. After passing through T_{IN}, circular domains begin to nucleate, seen as black droplets in Figure 4.1(b). It is natural to assume that these domains contain nematic LC; it is shown later using polarising microscopy that this is indeed the case. These regions of LC then begin to grow as seen in Figure 4.1(c), and locally the particle density increases. Particles expelled from these nematic regions accumulate at and are pushed along by the isotropic-nematic (IN) interface of growing nematic droplets. That the particles remain in the isotropic phase when isotropic and nematic phases coexistence has been observed previously in mixtures of particles and LC [5]. Nematic domains separated by boundaries of particles are soon observed, Figure 4.1(d). Initially nematic domains coalesce by breaking thinner boundaries as shown in Figures 4.1(e) to (f), leading to more elongated domains. From the original nucleation to this stage only requires $\sim$ 10 seconds. From

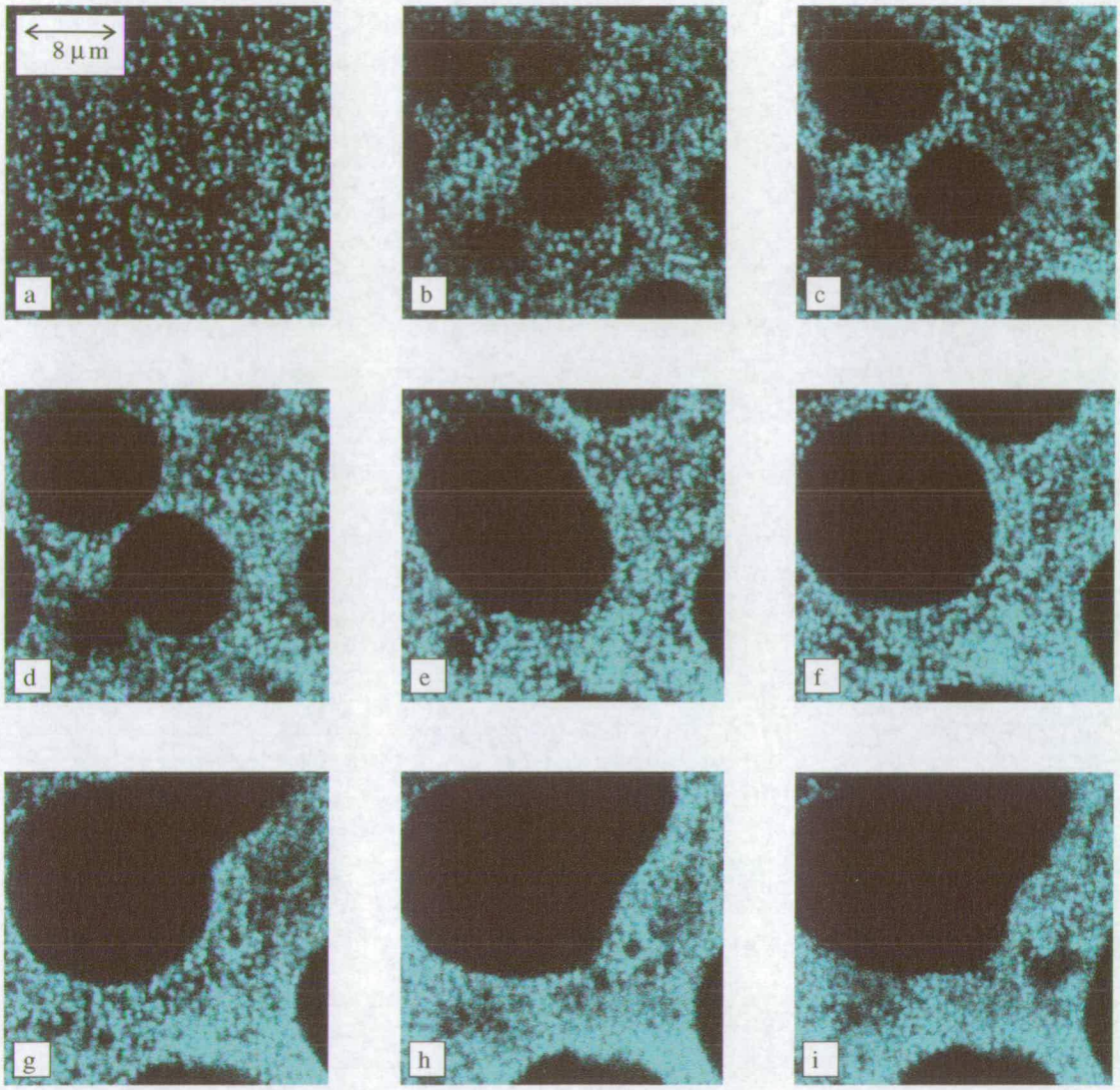

Figure 4.1: Network formation in a sample of 5CB with $\phi_w = 0.10$ of $R = 390$nm PMMA particles cooled at $\sim 1°$ C/min through T_{IN}. (a) just above T_{IN}, (b) $t = 0$ just below T_{IN}, (c) t =1.2s, (d) 2.4s, (e) 3.6s, (f) 7.2s, (g) 9.6s, (h) 16.8s and (i) 33.6s.

this point onwards, however, the kinetics of the phase separation are dominated by a slower process. The particle packing at the boundaries increases as the walls compactify (see Figures 4.1(g) to (i)) until motion becomes arrested and the particles remain frozen in position. This process observed with LSCM confirms what Meeker *et al.* [6] speculated should be the case based upon limited observations using bright field microscopy.

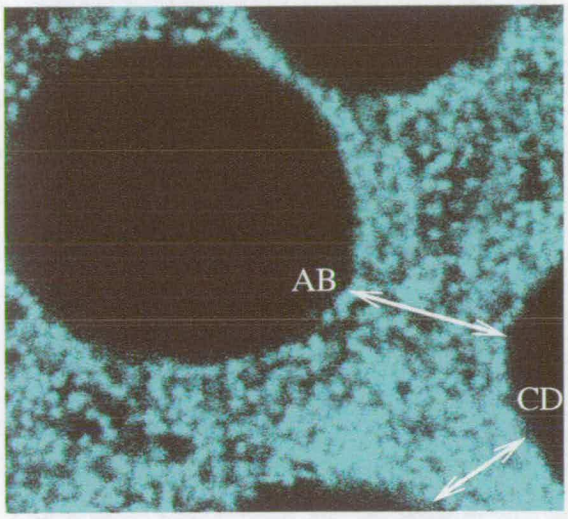

Figure 4.2: Microscopy image taken from sequence shown in 4.1. The scale remains the same. AB and CD denote positions where the thickness of the walls was measured.

In order to examine the compactification of the walls more closely imaging software was used to measure the thickness of the walls as a function of time. Using successive images from the sequence shown in Figure 4.1 the thickness of the walls at AB and CD (as shown in Figure 4.2) were measured. This was carried out from the stage where the original walls were formed until the network appeared to be frozen. The results are shown in Figure 4.3. The Figure reveals that there is a fast decrease in wall thickness over the first 10 seconds and a slower decrease over the next 10 seconds and it is almost constant thereafter.

The general features of this process of network formation have been observed for all particle sizes, concentrations and cooling rates that have been studied. A feature basic

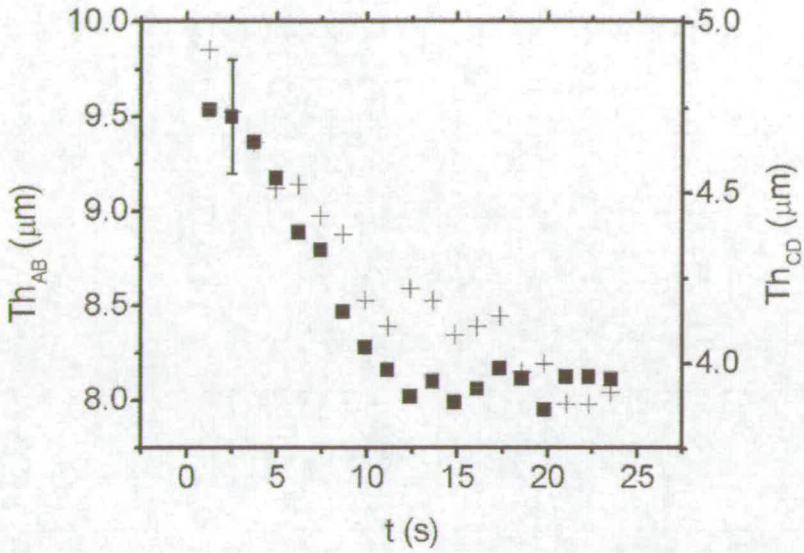

Figure 4.3: The thickness of the walls AB(solid squares) and CD(+) (see Figure 4.2) with time. Sample with $\phi_w = 0.10$ of $R = 390$nm particles.

to this process of network formation appears to be the ability of an IN interface to 'sweep along' particles that it passes.

4.3 Interface Velocity

The ability of an IN interface to sweep along particles has recently been examined experimentally by West *et al.* [40]. They studied the spatial distribution of particles of a range of sizes ($\sim$ 10 nm -8μm) subject to an IN interface travelling at various speeds, Figure 4.4. Particles were pushed along by the IN interface while remaining in the isotropic phase and they observed that only an interface moving slowly enough could capture the particles. Upon calculating the total drag force acting on a particle at such an interface by balancing the hydrodynamic, elastic and surface tension forces acting,

West *et al.* estimated the linear momentum that must be transferred to the particle to sweep it along. The maximum speed (v_{crit}) at which the interface can move and still sweep particles along is then found to be

$$v_{crit} \sim \frac{W}{\sqrt{K\rho}}, \tag{4.1}$$

where W is the anchoring energy of the LC at the surface of the particles, K is the average Frank elastic constant (see section 2.4.1) of the LC and ρ is the particle density. When West *et al.* evaluated this critical speed for their experimental system they found $v_{crit} \sim 1$ mm/s, which agreed with their experimental observations.

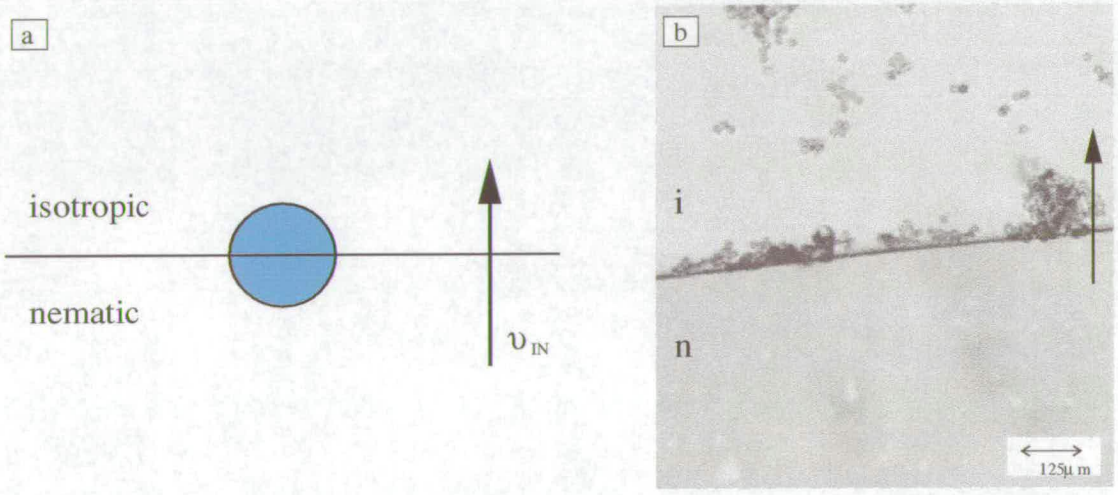

Figure 4.4: (a) Schematic diagram of a particle at isotropic-nematic interface, (b) Snaphot of an IN interface moving at $v_{IN} \approx 3\mu$m/s studied by West *et al.* [40]. n and i are the nematic and isotropic phases respectively. $R = 8\mu$m polymer particles were used. Taken from [40].

For mixtures of PMMA and 5CB Equation 4.1 gives $v_{crit} \sim 1$ mm/s - 1 cm/s using typical values $K \sim 10^{-11}$ J/m [40, 6], $W \sim 10^{-6} - 10^{-7}$ J/m^2 [40, 7] and $\rho \approx 1180$ kg/m^3 [73]. Using the image sequence in Figure 4.1 it was possible to estimate the speed of the IN interface in PMMA and 5CB mixtures when cooled at ~ 1°C/min through the transition. Measurements of growing nematic domains before coalescence

were made giving the interfacial speed in the range $v_{IN} \approx 1$ to 10μm/s. Hence, the interface does indeed travel significantly slower than the critical speed ($v_{IN} \ll v_{crit}$) that is predicted by West *et al.* to allow particles to be swept along.

The data in Figure 4.3 give $v_{IN} \approx 0.2\mu$m/s, which is outside this range. However, this reflects the interface movement at a later stage during which the walls are compactifying and interfacial movement is impeded by other nematic domains.

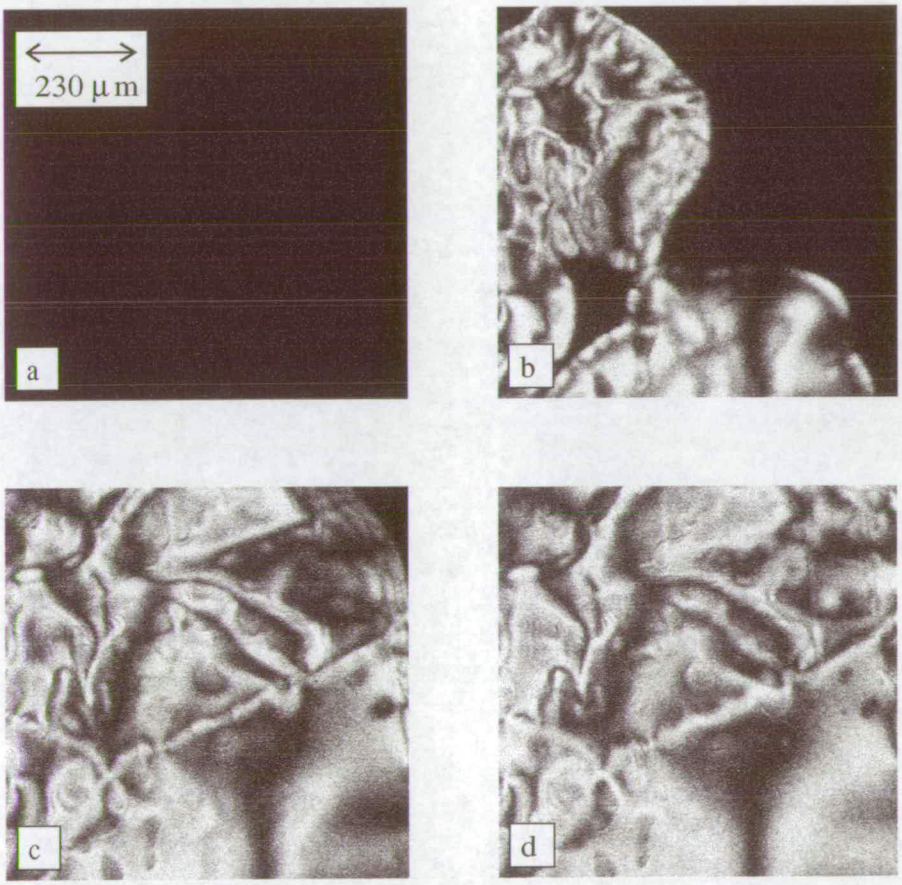

Figure 4.5: Formation of nematic phase in pure 5CB observed between crossed polarizers. Here and in all subsequent image sequences, the time t is measured from the moment T_{IN} was reached: $t =$ (a) 0 s, (b) 1 s, (c) 2 s and (d) 3 s. Cooling rate = 0.1°C/min.

Next, it is asked whether such slow interfacial speeds are expected at the IN transition for 5CB. Microscopy imaging of pure 5CB between crossed polarisers allows the nucleation and growth of the nematic domains during the IN transition to be observed,

Figure 4.5. The predominantly bright, textured areas are the birefringent nematic domains and the homogeneously dark domains are regions of isotropic LC. For a sample of pure 5CB cooled at ~ 1°C/min the interface speed was measured from the sequence of images in Figure 4.5 and it was found to be far greater than that possible to measure with the time resolution and field of view of the imaging system. As a result only a lower bound could be estimated: $v_{IN}^{pure} \gg 100\mu$m/s. Theory predicts [74] that the interface speed of pure 5CB during the IN transition $v_{IN}^{pure} \sim 1$ cm/s for undercooling $= 0.35$°(speed linearly dependent upon undercooling). This is much greater than the range of v_{IN} observed in PMMA+5CB mixtures ($v_{IN} \approx 1 - 10\mu$m/s) and it is $\gtrsim$ the critical speed v_{crit} ($v_{crit} \approx$ 1mm/s - 1cm/s) calculated for the PMMA + 5CB system. It is therefore questionable whether the IN interfaces would be able to sweep along particles in pure 5CB and permit network formation in the way described (Figure 4.1).

Why then is the speed of the interface in a mixture of PMMA and 5CB so much slower than that in pure 5CB?

It is suggested that the slow speed of the interface in mixtures of PMMA and 5CB is due to the presence of alkane impurities. The PHSA chains or 'hairs' (see Figure 4.6) that are chemically-grafted to the surface of the particles to sterically stabilise them could act as 'traps' for the alkane molecules in which the particles were dispersed before drying. Experimental evidence suggests that solvent molecules do penetrate the stabilising layer of PMMA particles [55]. These solvent molecules could subsequently be liberated when the particles are dispersed in 5CB. It will now be demonstrated that it is indeed reasonable to infer the presence of solvent impurities in the LC, and the effect of such impurites on the interfacial dynamics will be considered.

4.3.1 Impurities

The phase diagram of LCs mixed with dilute concentrations of non-mesogenic solutes has been studied [75, 76, 77]. Oweimreen *et al.* [51] have examined the effects of

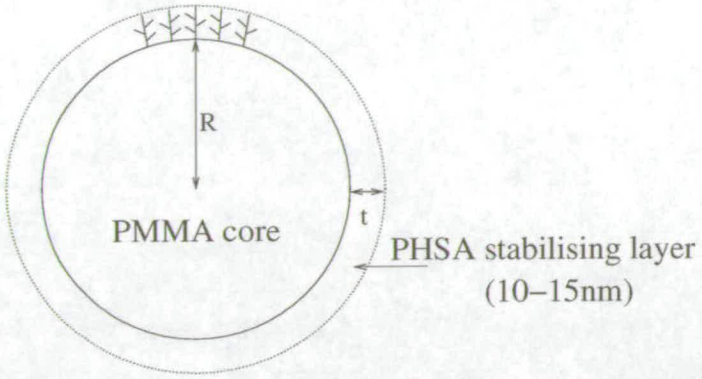

Figure 4.6: Schematic diagram of PMMA particle of radius R, with a PHSA stabilising layer of thickness t [55].

short-chain alkanes on the isotropic-nematic phase transition in 5CB. The presence of finite amounts of these alkanes depresses T_{IN} and introduces a two phase region in the phase diagram. In this region alkane-rich isotropic and alkane-poor nematic phases coexist over a temperature range of order 1°, Figure 4.7. Pure 5CB ($x = 0$) undergoes an IN transition at T_{IN}. When a composition of 5CB and mole fraction x_0 of alkane is cooled (dashed arrow) the nematic phase begins to appear at T_i and the isotropic phase disappears completely at T_n. As the temperature is decreased through the biphasic region there will be solvent repartitioning. A small amount of the alkane-rich isotropic phase will become nematic with the alkane component remaining in the isotropic phase. As a result the hexane concentrations of the isotropic and nematic phases will increase and decrease respectively[1]. The lines β_i and β_n given by,

$$\beta_i = \frac{dT_i}{dx} \tag{4.2}$$

and

$$\beta_n = \frac{dT_n}{dx} \tag{4.3}$$

[1]This will be discussed in section 4.4.

denote the extremes of the biphasic region opened up [78]. At a fixed temperature T_0 and composition x_0 the equilibrium state (point C on the phase diagram) is a coexistence of nematic and isotropic phases. The line AB is an isothermal line that connects the two phases (tie line) and using the lever rule the relative fractions of each phase can be calculated. For this temperature (T_0) and composition (x_0) the equilibrium state is the coexistence of the fractions AC/AB of isotropic and CB/AB of nematic, where AB, AC and BC denotes the lengths of the lines.

The presence of a finite biphasic region in the phase diagram should broaden the width of the peak in differential scanning calorimetry compared to the case of pure 5CB.

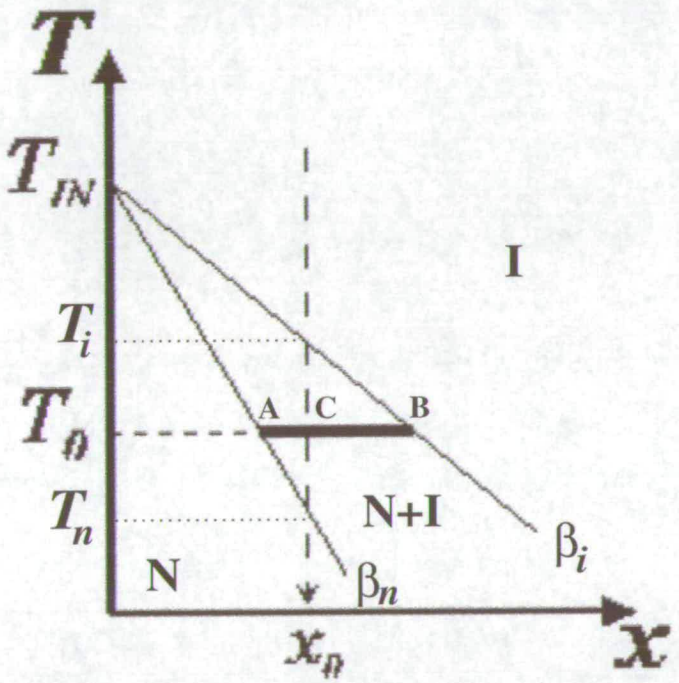

Figure 4.7: Schematic phase diagram of 5CB with small amounts (mole fraction x) of short-chain alkanes. The lines β_i and β_n denote the extremes of the biphasic region opened at finite values of x. When a sample of composition x_0 is cooled (dotted arrow) the nematic phase begins to appear at T_i and the isotropic phase disappears completely at T_n. The equilibrium state (point C) of a mixture with average composition x_0 at temperature T_0 can be read off the thick horizontal 'tie line' (of total length AB): a fraction CB/AB of nematic coexists with a fraction AC/AB of isotropic.

Differential Scanning Calorimetry (DSC) Results

A typical DSC scan of the composite under cooling is shown in Figure 4.8. The thermogram of pure 5CB (continuous line)[1] remains constant until ~ 35.2°C, where there is a sharp peak of $\sim 0.2°$ width. The transition temperature of pure 5CB was measured to be 35.2°C, the temperature where the peak in the heat flow occurred. The scatter graph (diamonds) shows the cooling of a composite with $\phi_w = 0.05$ of $R = 607$nm particles. The curve is constant until there is a peak at ~ 33.7°C of width $\sim 1.5°$. The broadening of the peak (from $\sim 0.2°$ for pure 5CB to $\sim 1.5°$ for the composite) and the decrease in T_{IN} by $\sim 1.5°$ is consistent with the presence of impurities that open up a biphasic region. However one may question whether this is caused by residual alkane molecules or the particles themselves?

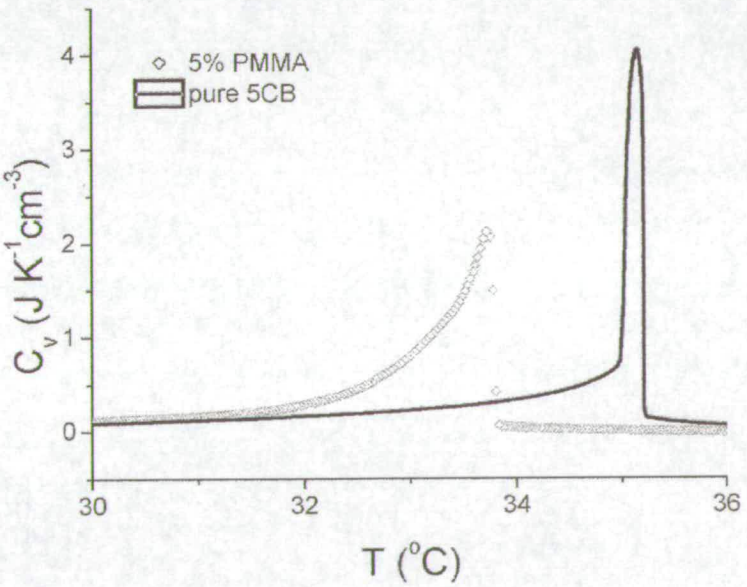

Figure 4.8: DSC scans with decreasing temperature. Composite with $\phi_w = 0.05$ of $R = 610$nm PMMA particles (◇) and pure 5CB (-). Cooling rate ≈ 4°C/h.

[1]This measurement was carried out by Dr. Doris Vollmer, an EU Marie Curie Fellow working in our laboratory during the first half of my thesis work.

In order to examine this DSC measurements, Figure 4.9, were carried out on (a) samples with $\phi_w = 0.10$ of $R = 460$nm PMMA particles and 5CB ($\diamondsuit$), (b) pure 5CB (-) and (c) a sample with $\phi_w = 0.009$ hexane and 5CB (solid diamond)[2]. When compared to pure 5CB the thermograms of the samples with PMMA and the samples with hexane show broader peaks of $\sim 1.9°$ and $\sim 1.5°$ at ~ 31.6°C and ~ 32.9°C respectively. The sample with particles has a decrease in transition temperature of $\sim 2.3°$ compared to pure 5CB and the hexane sample transition temperature decreases by $\sim 3.6°$. This similar decrease in transition temperature and broadening of the peaks supports the theory that the hexane is the cause of this decrease in transition temperature and opening up of a biphasic region.

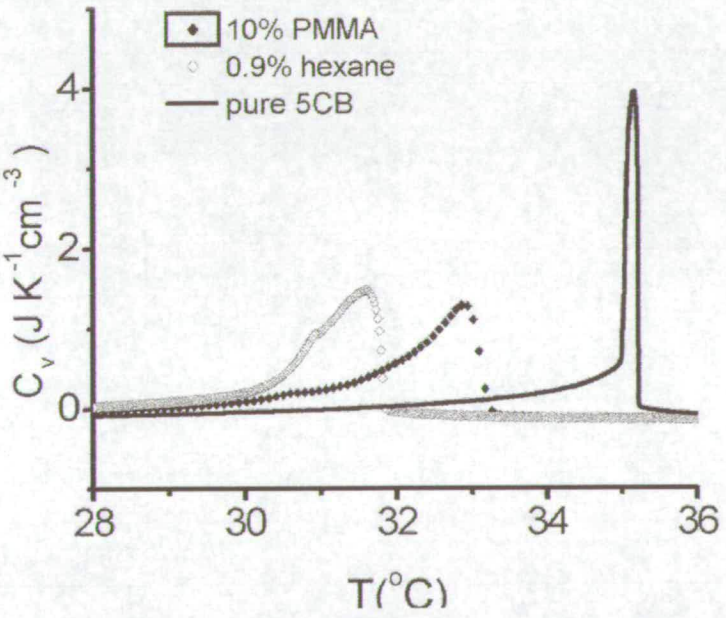

Figure 4.9: DSC scans with decreasing temperature of (a) a sample with $\phi_w = 0.10$ of $R = 460$nm PMMA particles and 5CB (solid diamond), (b) a sample with $\approx \phi_w = 0.009$ hexane and 5CB ($\diamond$) and (c) pure 5CB (-). Cooling rate ≈ 4.5 °C/h and measurements were taken from 45°C.

Particles were usually dried at 40°C at 10^{-2}Pa but in order to investigate the effects

[2]These measurements were carried out in collaboration with Doris Vollmer.

of hexane and the possibility of solvent retention the same particles were dried more rigorously at 60°C at 10^{-3}Pa. The resulting DSC curve ($\diamond$) can been seen alongside that of pure 5CB in Figure 4.10. The position of the composite curve relative to pure 5CB shows a transition temperature difference of only $\sim$ 0.1°C. The width of the composite peak is still wider ($\sim$ 0.5° compared to $\sim$ 0.2°), however it is considerably narrower than that of the 'wet' particles ($\sim$ 1.9° wide). The transition temperature of the LC is almost unaffected by the presence of the rigorously dried PMMA particles. This demonstrates that sample preparation and the retention of solvent impurites on the surface of the particle plays an important role in the behaviour of the LC as it passes through the IN transition.

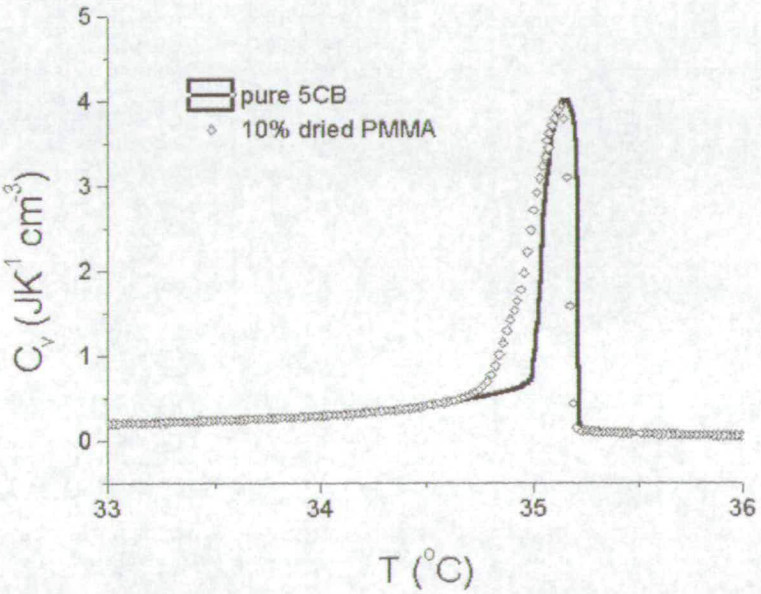

Figure 4.10: DSC scans with decreasing temperature of a sample with $\phi_w = 0.10$ of $R = 460$nm particles and 5CB($\diamond$) and pure 5CB (-). The particles were dried at 60°C at 10^{-3}Pa. Cooling rate $\approx$ 4.5 °C/h and measurements were taken from 45° C.

These thermograms suggest that hexane retained on the surface of the particle before dispersion in the LC is responsible for the decrease in transition temperature of the composite. In order to investigate this further T_{IN} as a function of hexane concentra-

tion and PMMA concentration was measured. Samples of $R = 240$nm particles and 5CB were made up with weight fraction $\phi_{PMMA} = 0.01 - 0.20$. Samples of hexane and 5CB were made up with $\phi_{hex} = 0.005 - 0.02$. The resulting DSC scans were analysed and the peak position was recorded as the transition temperature. The results are shown in Figure 4.11, along the top axis for hexane and the bottom for PMMA[3]. A linear dependence of T_{IN} with both ϕ_{PMMA} and ϕ_{hex} is observed, in agreement with the experimental results of Anderson *et al.* [7] and Oweimreen *et al.* [51] respectively. Previously the decrease in T_{IN} in these mixtures of PMMA and 5CB was attributed to the elastic energy surrounding the particles [7].

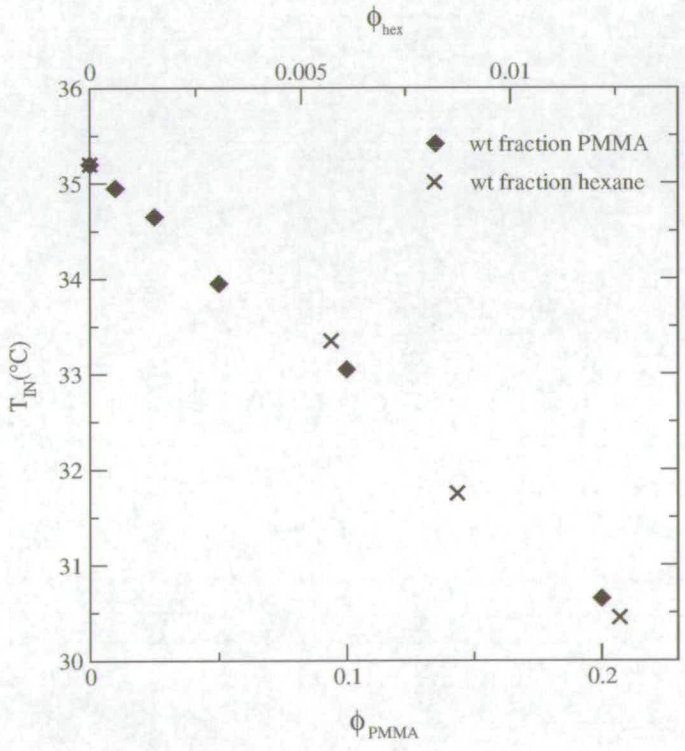

Figure 4.11: The variation of transition temperature with ϕ_{hex}(x) and ϕ_{PMMA}(solid diamond). The particles used were of radius 240nm.

Now the reduced temperature T^* is defined by

[3]These measurements were carried out in collaboration with Doris Vollmer

$$T^* = \frac{T}{T_{NI}}, \tag{4.4}$$

where T is the transition temperature of the composite and T_{IN} is the transition temperature of pure 5CB, in Kelvin. T^* was plotted against molefraction of hexane (mf_{hex}) and ϕ_{PMMA}, Figure 4.12.

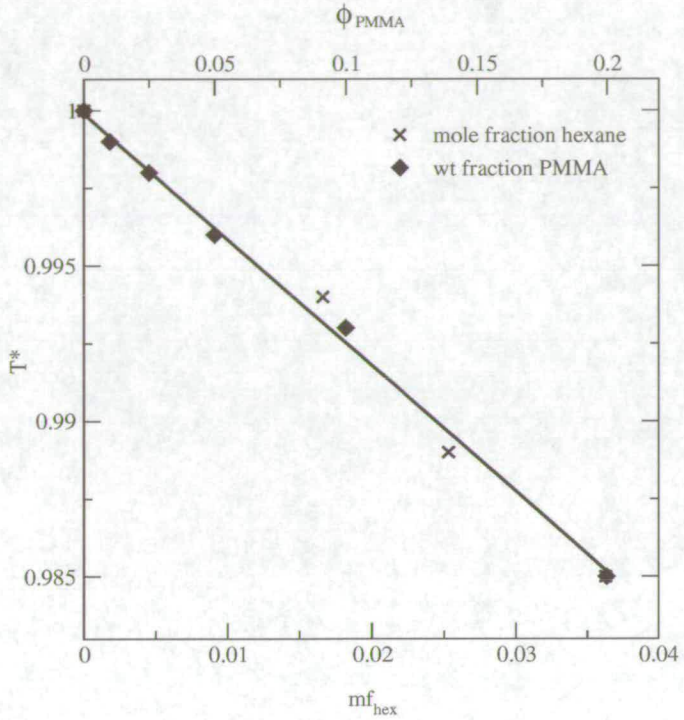

Figure 4.12: The variation of transition temperature with mf_{hex}(x) and ϕ_{PMMA} (solid diamond). Particles of radius 240nm were used.

Taking the temperature at which the nematic phase begins to appear (T_i) as the point where the thermogram begins to rise to form the peak gives $\frac{dT_i^*}{dx} = \beta_i^* = 0.423$ where x is the molefraction of hexane[4]. Values of $\frac{dT_i^*}{dx}$ have been measured for a number of alkanes [51], but not of hexane itself, Figure 4.13. As shown in the figure odd-numbered alkanes are slightly more disruptive than even ones in 5CB. Extrapolating

[4]Measuring T_n from calorimetric data is difficult because the peaks tend to have long tails and the completion of the peak is difficult to determine.

these values for the even alkanes leads one to expect $\frac{dT_i^*}{dx} = \beta_i^* = 0.434$ and $\beta_n^* = 0.504$ for $n = 6$. This value of β_i^* is slightly higher than that measured calorimetrically for these mixtures. These extrapolated values give a biphasic region of width $(T_i - T_n)$ ~ 0.42°for a composition of 0.02 mole fraction hexane and 5CB. This is considerably smaller than the width of the DSC peak observed for mixtures of PMMA, hexane and 5CB. Vollmer *et al.* have suggested that the particles may be responsible for the extra lowering of the transition temperature [79].

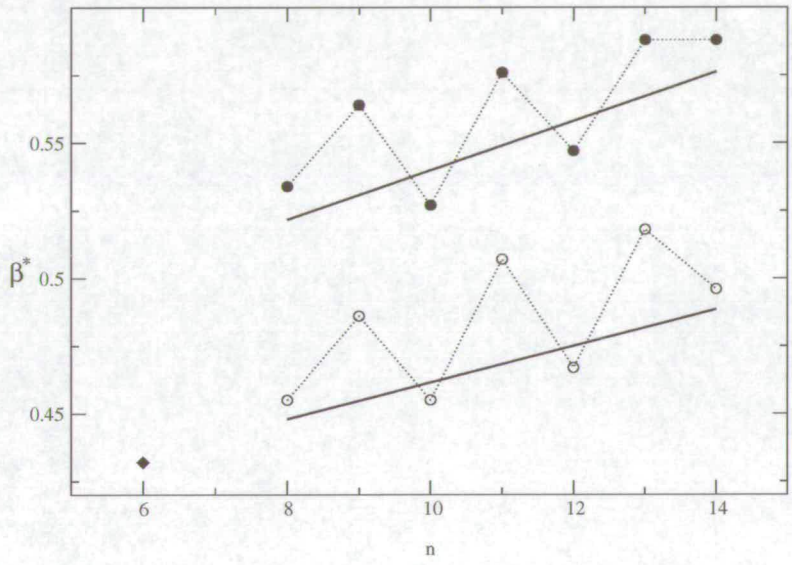

Figure 4.13: The variation of β_i^* (○) and β_n^* (solid circles) with solute carbon number n measured by Oweimreen *et al.* [51] and β_i^* for hexane, PMMA and 5CB mixtures (solid diamond).

An investigation of the variation of T_{IN} with particle size was tempting. However, the drying procedures for different batches of PMMA were not exactly the same and such a comparison was not possible.

4.3.2 Is This Amount of Hexane Reasonable?

It is possible to estimate the amount of hexane required per particle to cause a decrease in T_{IN} by the amounts measured. The best fit line for the data points displayed in

Figure 4.12 was found to be $T* = 1 - 0.074\phi_{PMMA}$ and $T* = 1 - 0.438\text{mf}_{hex}$. For these best fit lines to lie on top of each other the mass of hexane required per particle (of radius 240nm) is $\sim 4 \times 10^{-15}$g. Hence the number of hexane molecules[5] required per particle of radius 240nm is $\sim 3 \times 10^{7}$. But is this a reasonable amount of hexane to be retained on the surface of the particle in the 'hairs'?

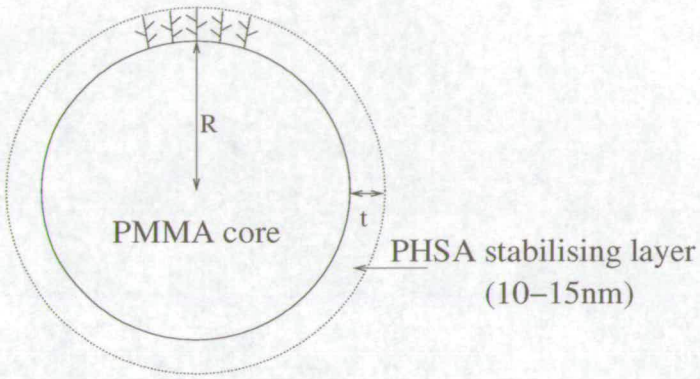

Figure 4.14: Schematic diagram of PMMA particle of radius R, with a PHSA stabilising layer of thickness t [55].

The PHSA hairs, Figure 4.14, packed on the surface of the PMMA particle are $\sim 10 - 15$nm in length and taking into account the branching of the chain the estimated molecular volume is $\sim 10000\text{Å}^3$ [55]. Assuming complete coverage of the chains on the surface of the particle and a surface area per chain of $\sim 200\text{Å}^2$, as estimated by experiments [55] the hairs can be modelled as cyclinders of height 150Å, base area $\sim 66\text{Å}^2$ and volume 10000Å^3. The space available to hexane between the cyclinders can be calculated, Figure 4.15, and dividing this space by the molecular volume of hexane [81] gives 3.6×10^7 hexane molecules per particle of 240nm radius. Hence the 3×10^7 molecules per particle required by the DSC data is reasonable. For a mixture with $\phi_w = 0.20$ of R=240nm particles the calculation estimates $\phi_{hex} \sim 1.52\%$ [81]. Calorimetric measurements, Figure 4.11, give $\phi_{hex} \approx 1.21\%$ in a sample with $\phi_w = 0.20$ of R=240nm particles. Therefore the hexane needed per particle is already

[5]The mass of a hexane molecule is 1.44×10^{-22}g [80].

achieved by filling the stabilising layer with alkane. It is therefore conceivable that hexane retained at the surface of the particle from drying is the cause of the decrease in T_{IN} and the broadening of the DSC peak.

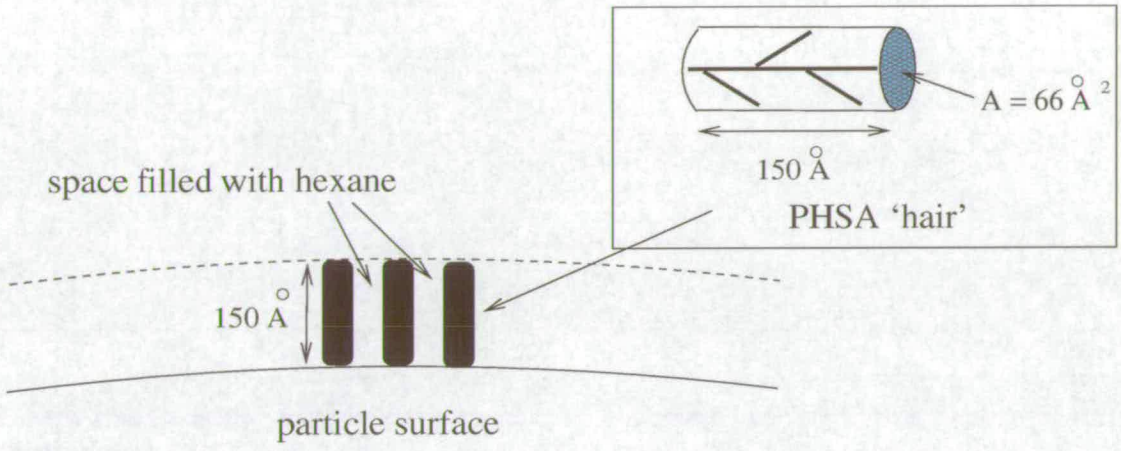

Figure 4.15: The surface of the PMMA particle; the PHSA 'hairs' are modelled as cylinders of height 150Å, base area $\sim 66\text{Å}^2$ and volume $\sim 10000\text{Å}^3$ [55]. The space between the hairs (cylinders) available to hexane is calculated.

These calorimetry measurements have demonstrated that the retention of hexane on the surface of the particles prior to dispersion in 5CB plays an important role. Their presence leads to the coexistence of isotropic and nematic domains when cooling through the IN transition. I now go on to demonstrate that this has important effects on the interfacial dynamics across the transition, and therefore on the possibility of forming particle networks.

4.3.3 Kinetics of Nucleation

It is possible to observe the interfacial movement in mixtures of hexane and 5CB as the sample is cooled through the IN transition. Figure 4.16 shows the nucleation and then growth of nematic domains in a 0.02 mole fraction hexane and 5CB mixture. This is the amount of hexane that a sample with $\phi_w = 0.09$ of $R = 240$nm particles should carry if the PHSA stabilising layer is filled [55]. Several small domains nucleate:

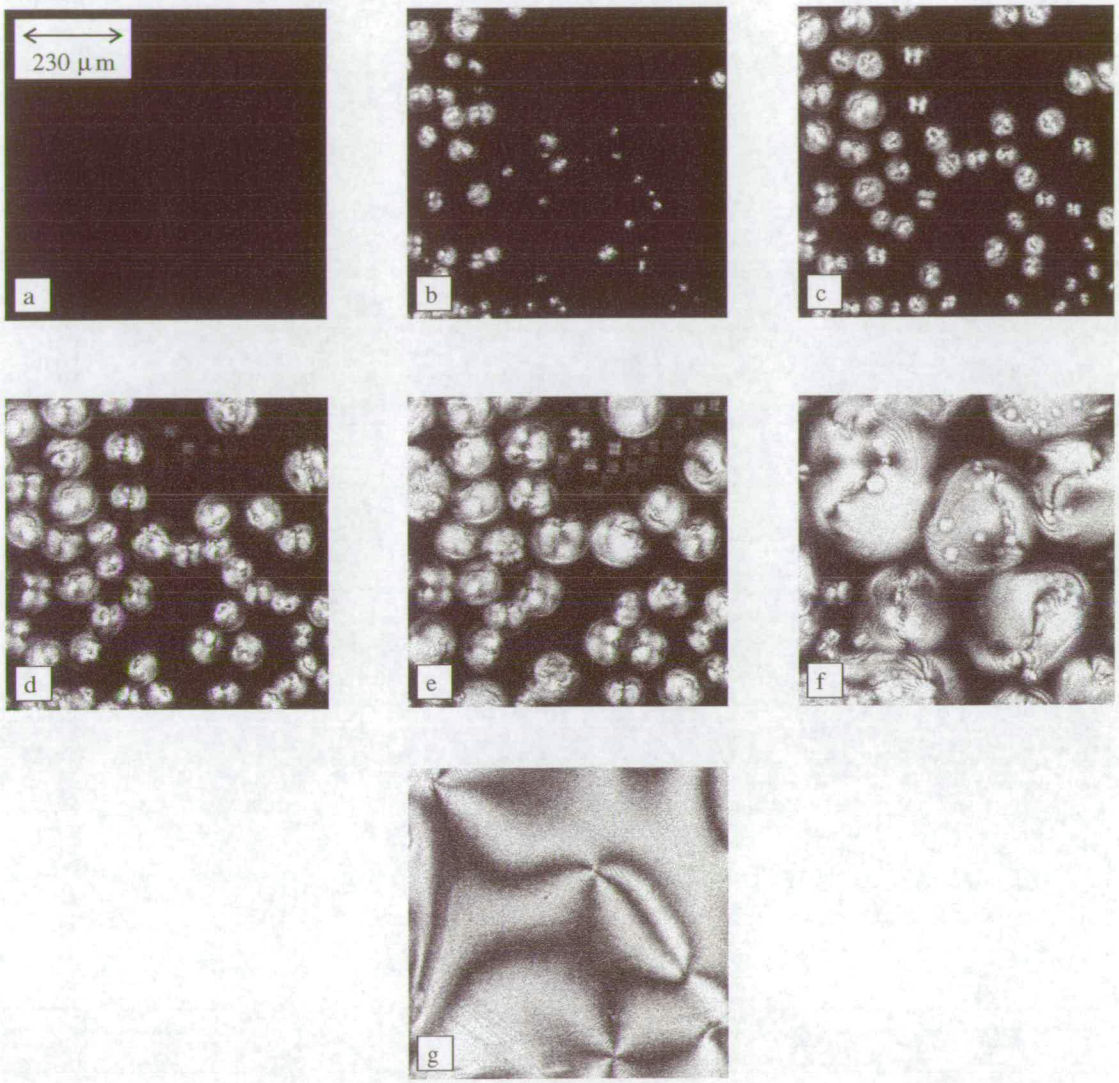

Figure 4.16: Formation and growth of nematic domains in a mixture of 0.02 mole fraction hexane and 5CB observed between crossed polarizers. Time t = (a) 0 s, (b) 15 s, (c) 30 s, (d) 45 s, (e) 1 min., (f) 2 min. and (g) 3 min. Cooling rate = 0.1 °C/min.

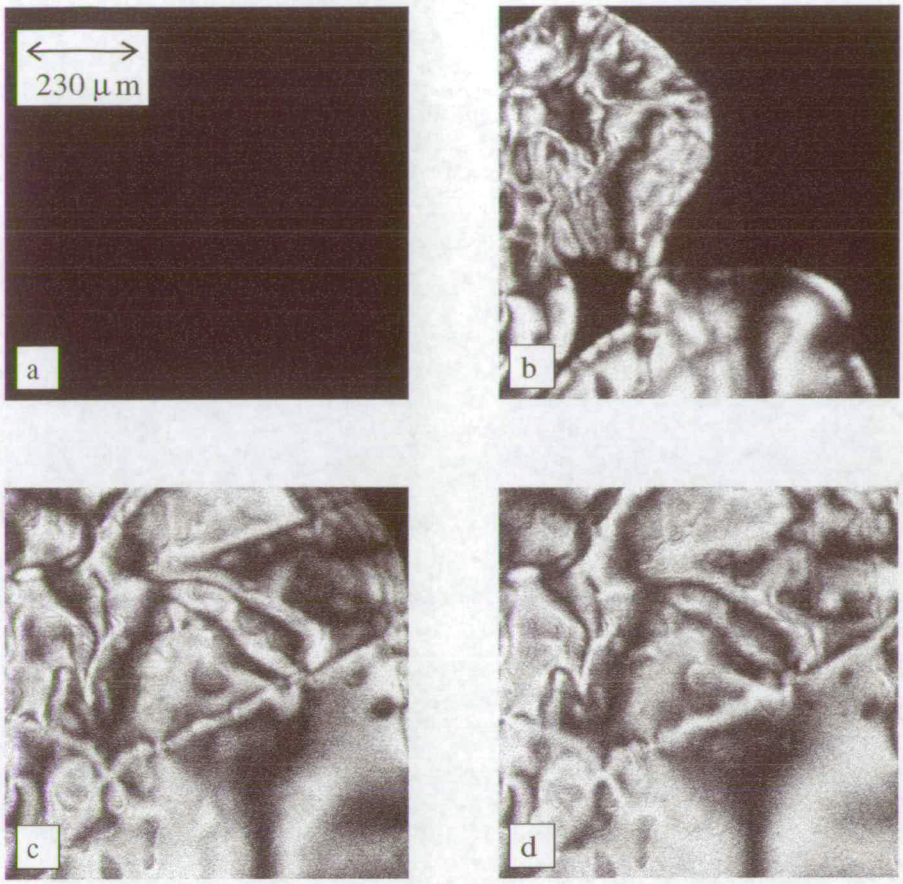

Figure 4.17: Formation of nematic phase in pure 5CB observed between crossed polarizers. t = (a) 0 s, (b) 1 s, (c) 2 s and (d) 3 s. Cooling rate = 0.1°C/min.

~ 50 in the 800μm square sample area shown in Figure 4.16(c). These domains grow slowly and $\approx$ 3 min ($\approx 0.3°$) have passed before the mixture is completely nematic. The interfacial speed measured from this image sequence, $v_{\mathrm{IN}} \approx 5\mu$m/s, is within the range of speeds found for PMMA + 5CB mixtures ($v_{\mathrm{IN}} \approx 1 - 10\mu$m/s), see Table 4.1.

When compared to the same process in 5CB (Figure 4.17) one can see that there is a striking difference in the nucleation and growth of nematic domains with time/temperature. Only one domain is observed growing in the same 800μm square sample area. The entire sample is nematic within 3 seconds of crossing T_{IN}, compared to $\approx$ 3 min for the hexane and 5CB mixture.

System	Interface speed v_{IN}
PMMA+5CB	1-10μm/s
hexane+5CB	5μm/s
5CB	$\gg$ 100μm/s, Theory: $\sim$ 1cm/s
critical speed v_{crit}	1 mm/s - 1 cm/s

Table 4.1: IN interface speeds estimated from microscopy imaging and critical speed estimated by West *et al.* [40] that the interface can move at and still sweep along particles.

In contrast, Figure 4.18 is an image sequence taken of a PMMA and 5CB mixture under identical conditions to that of the 5CB and hexane mixture and of the pure 5CB. The similar way in which the domains nucleate and grow in Figures 4.16 and 4.18, and their difference with Figure 4.17, is apparent. In the case of the PMMA and 5CB mixture, as with the 5CB and hexane mixture, many small domains nucleate and grow slowly and it is $\approx$ 4 min until all isotropic disappears.

Interpretation

But why does hexane slow down the IN interface? As shown in the width of the DSC peak and in the phase diagram, see Figure 4.19, for pure LC there is no biphasic region and the whole of the system wants to become nematic at all $T < T_{IN}$. The undercooling, $\tau = T_{IN} - T$, controls the speed of the interface between growing nematic droplets and the surrounding (shrinking) isotropic material, $v_{IN} = v_{IN}(\tau)$ [74]. Even a very small degree of undercooling will give $v_{IN} \gg v_{crit}$.

On the other hand, mixtures of 5CB and particles with alkane spend large amounts of time in the biphasic region at the time when the network is being formed. For the cooling rates accessible ($\sim$ 0.1°/min - 30°/min) the time spent in this biphasic region of width of order a few degrees is between 1s and 10mins. Thus it can be considered that the system crosses the biphasic region quasi-statically. During this time, at any one temperature the equilibrium state of the system is a fixed amount of nematic droplets

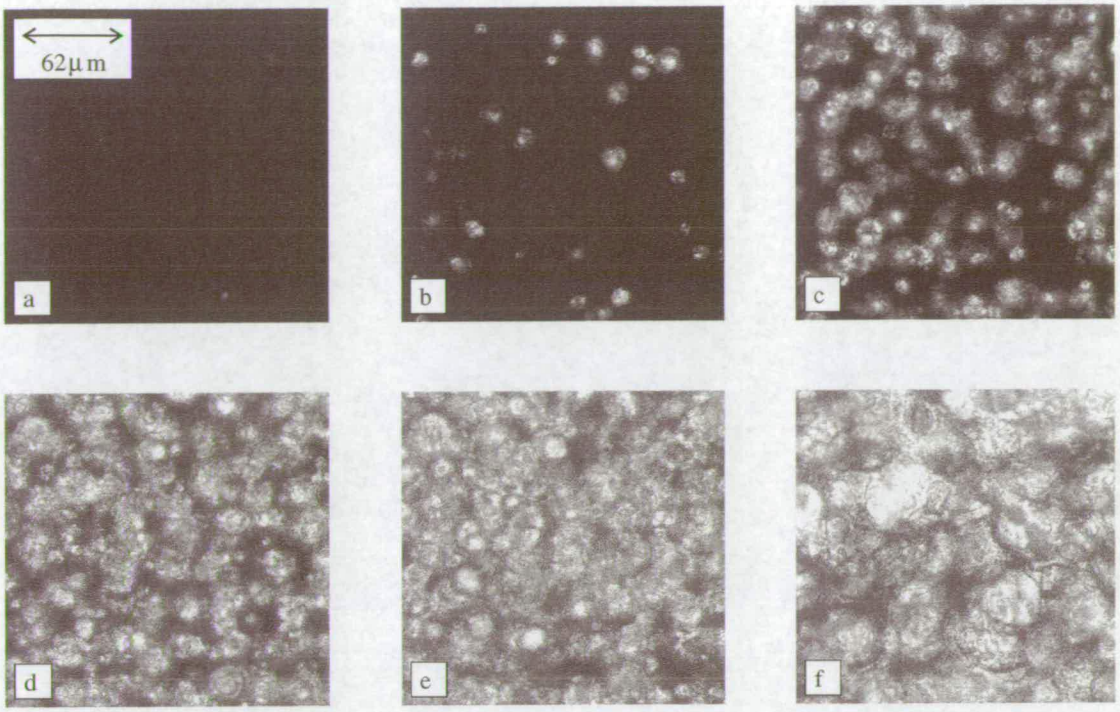

Figure 4.18: Formation and growth of nematic domains in a PMMA+5CB mixture taken under identical conditions to the images shown in Figure 4.16. Time t = (a) 0 s, (b) 15 s, (c) 30 s, (d) 45 s, (e) 1 min. and (f) 4 min. Sample with $\phi_w = 0.05$ of $R = 530$nm particles. Cooling rate $\approx$ 0.1 °C/min.

coexisting with isotropic, determined by the lever rule, see Section 4.3.1.

On cooling a mixture of composition x_0 through the biphasic region quasistatically (dashed arrow in Figure 4.19) the fraction of nematic f grows linearly with the undercooling (see inset), $f \propto \tau$. At T_i when nematic begins to appear $\tau = 0$ and when $T = T_n$ $\tau = \Delta\tau$ and the fraction of nematic = 1.

If the temperature is fixed, $d\tau/dt = 0$, then f is fixed and the IN interfaces will be stationary[6]. This has been confirmed in polarising microscopy observations for both the PMMA and 5CB mixtures and the hexane and 5CB mixtures.

Since $v_{IN} \propto df/dt$ and $f \propto \tau$,

[6]This refers to nucleation before the slower processes of droplet coalescence and Ostwald ripening begin.

$$v_{IN} \propto \frac{d\tau}{dt}. \tag{4.5}$$

Hence the interfacial speed is directly proportional to the cooling rate $d\tau/dt$ and can be controlled experimentally. By this mechanism the existence of impurities and therefore a biphasic region slows down the movement of the IN interfaces.

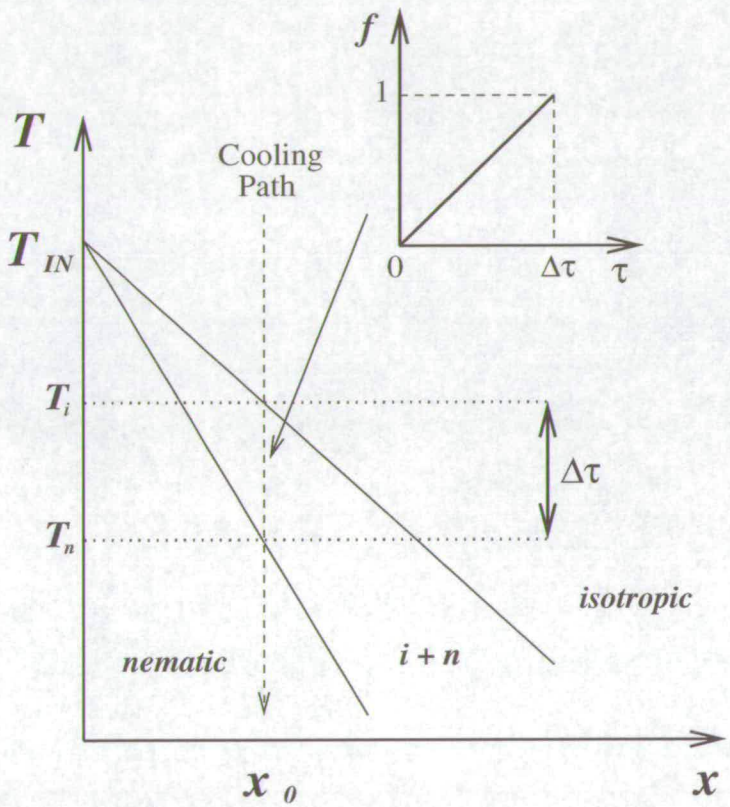

Figure 4.19: Schematic phase diagram of 5CB with small amounts (mole fraction x) of alkane. Pure 5CB ($x = 0$) undergoes a IN transition at T_{IN} with a very narrow biphasic region. A composition of x_0 when cooled through the biphasic region will have nematic fraction $f \propto \tau$ (inset).

When cooling through the biphasic region most of the particles and hexane remain in the isotropic phase. Therefore when the network is formed it is expected that most of the hexane is retained in the walls. NMR data [79] shows that the LC in these walls

is isotropic and it is suggested that a high concentration of hexane within the walls is responsible for this.

4.4 Reversibility

Up to this point only the initial network formation upon cooling has been examined; now the reversibility of the network will be discussed.

Microscopy

Microscopy observations of the network formed in a sample with $\phi_w = 0.05$ of R=390nm particles while being heated at 5 °C/min from $\sim$ 20 °C to $\sim$ 80 °C are shown in Figure 4.20. When heated to just above T_{IN} the particles remain fixed in position and the network remains unchanged (the isotropic nature of the LC has been confirmed with observation between crossed polarisers). As T increases single particles at the edges of walls start to exhibit Brownian motion. With increasing temperature single particles and clusters become free and start to move around the sample, Figure 4.20(b). Large sections of wall remain, but as the temperature increases further they eventually become free and diffuse around the sample as large clusters, Figure 4.20(c)[7].

A network formed in a sample with $\phi_w = 0.05$ of R=390nm particles is heated into the isotropic phase and then cooled back into the nematic. Microscopy observations of this process are shown in Figure 4.21. The original network formed at the bottom of the sample cell, Figure 4.21(a), has LC domains which are ~ 7 μm in diameter. Upon heating the network breaks up into clusters and individual particles, Figure 4.21(b). Higher up in the sample cell clusters (circled) and individual particles are also observed, however the particle density is lower than that at the bottom, Figure 4.21(c).

[7]The temperature of the sample when observed is hard to determine because the objective is in contact.

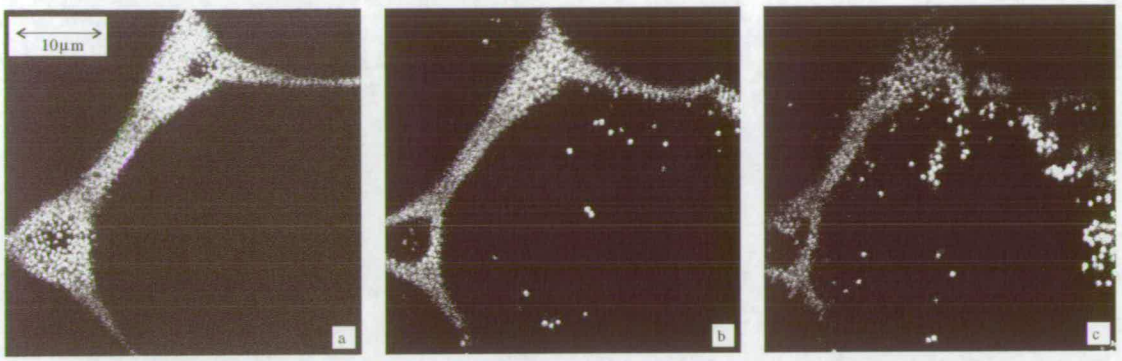

Figure 4.20: Microscopy images of the network with increasing temperature. (a) $T < T_{IN}$, (b) the isotropic phase ($T_a \gg T_{IN}$), (c) the isotropic phase ($T_b > T_a$). Sample with $\phi_w = 0.05$ of R=390nm particles. Heating rate $\approx$ 5 °C/min.

Upon cooling into the nematic phase a new network is formed. The network formed at the bottom of the sample cell, Figure 4.21(d), has LC domains ~ 2 μm in diameter. The particle density is higher than in the original network that was formed and the LC cells are smaller (~ 2 μm compared to ~ 7 μm in the original network). This suggests that clusters of particles sediment to give a higher particle density at the bottom of the sample. The later network also has much thicker walls. Presumably this is because it is clusters of particles being pushed together by the IN interfaces, and not single particles (as was in the initial cooling).

DSC

When a sample is cooled from the initial well mixed isotropic dispersion a single DSC peak has always been observed. DSC measurements, Figure 4.22, were taken under cooling during a series of successive scans cycling through the IN transition. A sample with $\phi_w = 0.05$ of $R = 117$nm particles was cooled and heated between 40°C and 25°C for 4 cycles and then cooled and heated between 60°C and 25°C for 5 cycles. For the measurements in which heating stopped at 40°C only a single peak at ~ 34.1°C was observed which remained very similar in shape and size with successive coolings. After the 4th cooling this peak had shifted by only $\sim 0.05°$ to lower temperatures.

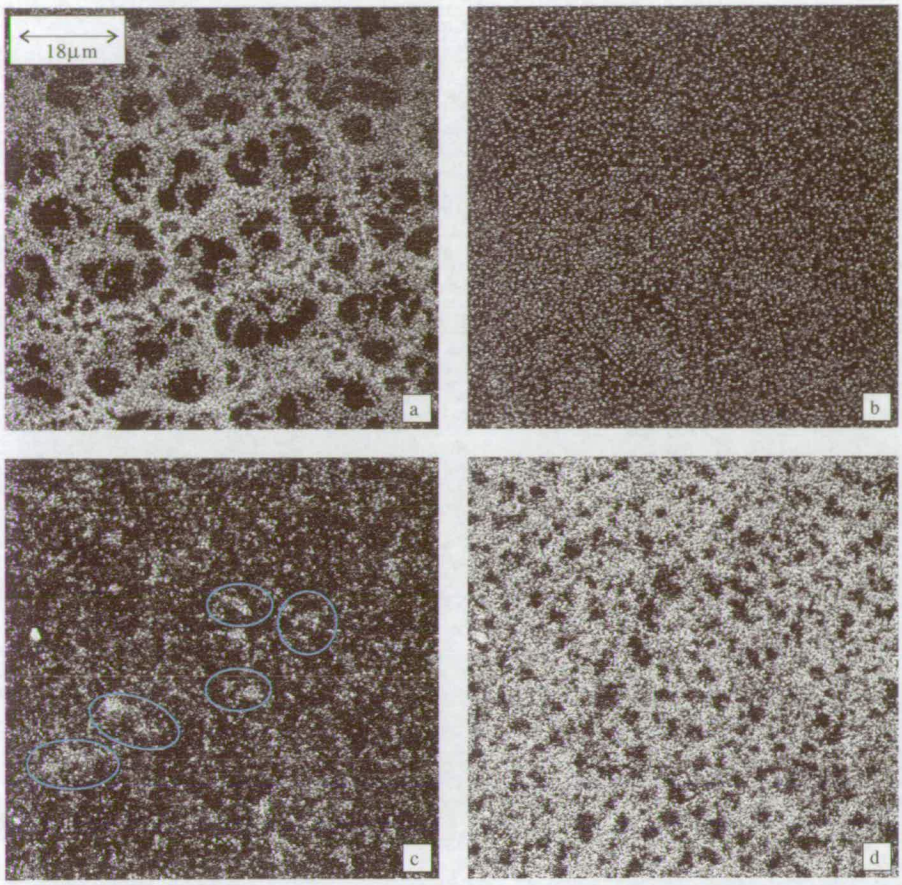

Figure 4.21: Microscopy images of a network upon heating into the isotropic phase ($T \gg T_{IN}$) and then cooling back into the nematic. (a) The initial network formed ($T < T_{IN}$) at the bottom of the sample, (b) the isotropic phase ($T \gg T_{IN}$) at the bottom of the sample, (c) the isotropic phase higher in the sample and (d) the network formed upon cooling ($T < T_{IN}$) at the bottom of the sample. Sample with $\phi_w = 0.10$ of R=390nm particles. Clusters of particles are encircled.

Upon heating to 60°C a second peak appeared at a higher temperature of $\sim$ 34.2°C. The original peak decreased in height and moved to a lower temperature ($\sim$ 33.8°C). The total heat flow remains constant for each thermogram. This suggests that two LC regions with different hexane concentrations have developed and that heating to a temperature deep into the isotropic ($T > T_{IN}$) is important.

Figure 4.23 shows how the thermogram changed with further cycling between 60°C and 25°C. With repeated cooling a second peak appeared, increased in height and moved to progressively higher temperatures (it moves to $\sim$ 34.25°C) and the orig-

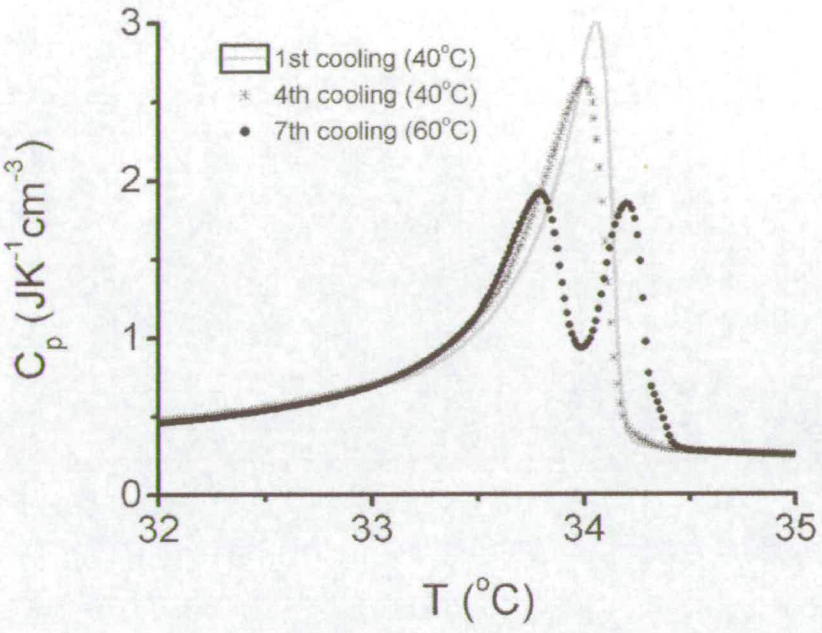

Figure 4.22: Successive DSC scans with decreasing temperature of $\phi_w = 0.05$ R= 117nm particles in 5CB. The cooling rate is 6 °C/h and measurements are taken from 40° C.

inal peak decreased in height and moved to lower temperatures ($\sim$ 33.56°C). One interpretation of this data is that the sample is becoming heterogeneous upon repeated heating/cooling cycles, with one region of LC becoming more concentrated with hexane and another becoming less concentrated with hexane. From Figure 4.11 the concentrations of hexane expected in these regions are $\phi_w = 0.0025$ and $\phi_w = 0.0045$ respectively.

Macroscopic Observations

Visual observations of a sample (cell 2mm width, 10mm length and 4cm height)[8] suspended in a temperature contolled water bath allowed the macroscopic appearance of the sample to be observed as it was repeatedly heated and cooled between 50°C and

[8]Sample cell of volume $\sim$ 0.8ml; comparable to the 0.52ml volume of the DSC sample cell.

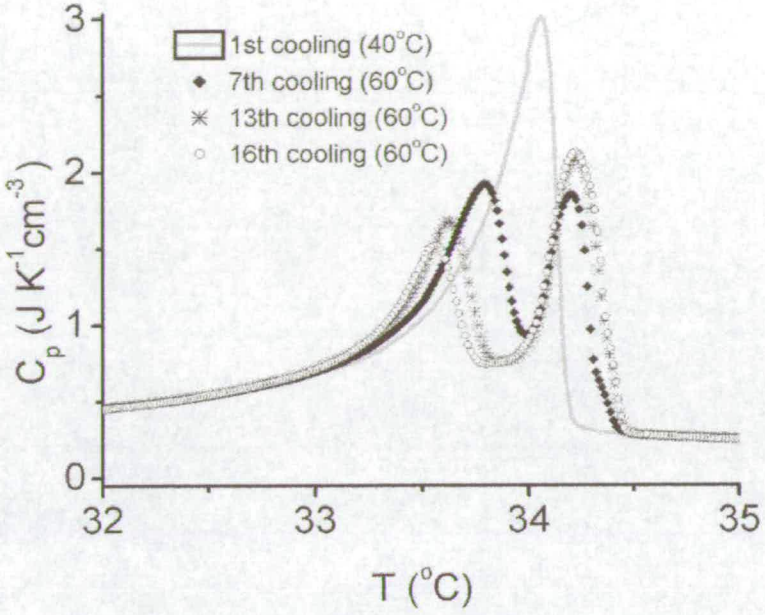

Figure 4.23: Successive DSC scans with decreasing temperature of ϕ_w=0.05 117nm particles in 5CB. The cooling rate is 4.5 ° C/h and measurements are taken from 45° C.

20°C. Several images taken during this process are shown in Figure 4.24. The initial well mixed isotropic state is observed as an opaque homogeneous sample, Figure 4.24(a). After cooling into the nematic phase a network can be distinguished spanning the sample cell, Figure 4.24(b). During the first heating the LC becomes isotropic (and transparent) and the network can clearly be observed across the sample, Figure 4.24(c), just above the transition temperature ($\sim$ 37°C). Further heating deeper into the isotropic phase shows the network 'collapse' and clusters or walls are observed sedimenting. Now, Figure 4.24(d), at $\sim$ 46°C a low density particle phase is observed at the top of the sample and a particle rich phase at the bottom. Upon cooling for the second time into the nematic (Figure 4.24(e)) and then heating into the isotropic (Figure 4.24(f)) the high particle concentration region decreases in size, expelling more LC from between the particles into the low particle density region above it.

This is consistent with the DSC sample, which when removed from the calorimeter

sample cell (in the isotropic phase) after repeated cycling consisted of an almost particle free LC region at the top of the cell and a dense particle phase at the bottom.

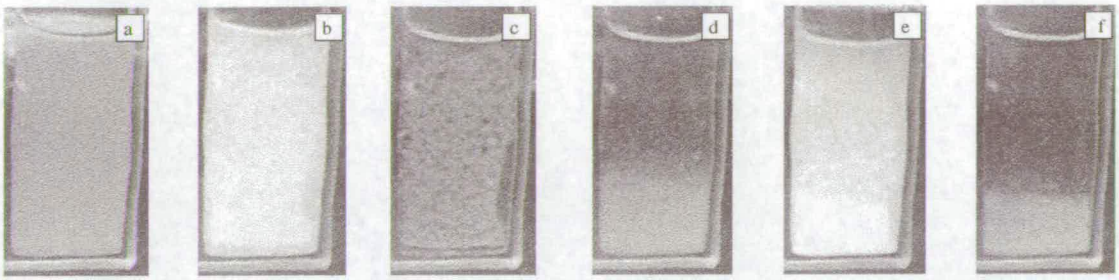

Figure 4.24: The sample composition with successive heating and cooling.(a) Well mixed isotropic (37.5°C), (b) initial network after first cooling (27.2°C), (c) in the isotropic during first heating (37°C), (d) in the isotropic after first heating (46°C) , (e) after second cooling (26.2°C), (f) after second heating (45.4°C). Sample with $\phi_w = 0.05$ of $R = 500$nm particles. Cooling rate $\approx$ 4°C/h, Heating rate $\approx$ 120°C/h.

Interpretation

Putting these microscopic and macroscopic observations together with the thermal data the following picture can be suggested. After the inital network formation when the sample is heated just above T_{IN} the network structure remains and individual particles or clusters become free. Under cooling these particles would be expelled to join the walls of the network again. This is represented by the individual peak in the calorimetry trace.

However, heating further into the isotropic phase ($T \simeq 50$°C) the network breaks up and large clusters or walls of particles sediment. The sedimentation velocity is given by,

$$v_{sed} = \frac{2\Delta\rho g R^2}{9\eta} \tag{4.6}$$

where $\Delta\rho$ is the density difference between the PMMA particle and the isotropic LC, η is the viscosity of the LC and R is the particle radius. Isotropic 5CB at 50 °C has $\eta \sim 0.015$ Pa S [82, 83] and $\rho \sim 1$ g/cm^3 [84, 85]. The density of PMMA particles ~ 1.18 g/cm^3 [73]. For a single particle of radius $R = 390$nm this gives $v_{sed} \sim 4$nm/s but for a cluster of ~ 10 particles this gives $v_{sed} \sim 400$nm/s. The time spent in the isotropic phase during cyclic DSC measurements (cooling rate ≈ 6 °C/h) is $\approx 3 \times 10^4$s, allowing clusters of such size to sediment ≈ 1cm.

This leads to a particle rich phase at the bottom of the sample and a low particle concentration phase at the top. Upon cooling the upper LC becomes nematic at a slightly higher temperature than in the initial cooling; suggesting a lower hexane concentration as well as PMMA concentration. The LC in the particle rich region undergoes the transition at a lower temperature. This is represented by the two peaks in the thermogram. The second peak at the higher temperature represents the upper LC region undergoing the transition and the initial peak is the LC in the lower region going through the transition. Similar splitting has been observed in mixtures of micelles of $R \sim 2$nm with 5CB, in which macroscopic phase separation of a micelle rich isotropic phase and a micelle poor nematic phases was found [42, 44]. Similar calorimetric measurements on mixtures of 5CB and particles performed by Petrov *et al.* [9] were attributed to two successive phase transitions during the process of network formation. The first due to the growing nematic droplets expelling the particles into the isotropic to form 'swollen' walls. The second because the nematic pressure on the 'swollen' walls causes them to collapse and the isotropic LC to be expelled into the nematic phase, thereby undergoing the IN transition. However, calorimetric measurements presented in this thesis and by Anderson *et al.* [7] failed to observe two peaks during the initial cooling.

Repeated cooling causes the particle rich region to become more compactified and less LC remains between the particles. Hence the amount of LC undergoing the transition at the lower temperature decreases, reflected in the decrease in size of the thermal peak, and because the concentration of hexane in this region is increasing the peak shifts to

slightly lower temperatures. Similarly the almost particle free LC region increases in size and the hexane concentration reduces even further. This is reflected in the second peak appearing at higher temperatures and increasing in size as the coolings progress. That there is little change in the DSC trace between the 13th and the 16th cooling is unsurprising if one considers that close packing may already have been achieved in the particle rich phase.

4.5 Rheology

To quantify the change in the mechanical properties of the composite as the network is formed small amplitude oscillatory measurements were carried out. A 4cm 2° cone was used to make the measurements for most of the temperature range, however in the isotropic phase G' was too small to measure with this cone (see section 3.6.4). As a result a 6cm 0.5° cone was used to examine the properties of the composite in the isotropic phase and to make measurements of pure LC.

Figure 4.25 shows the temperature dependence of a) the storage modulus G' (solid diamond) and loss modulus G'' (open diamond)[9] of a sample with $\phi_w = 0.05$ of R=370nm particles cooled at 0.5°C/min, b) the storage modulus G' (solid circle) and loss modulus G'' (open circle)[10] of the same mixture in the isotropic phase and c) G' for pure 5CB (solid line). In the isotropic phase the storage modulus of the composite is small (~ 0.1 Pa) and consequently there is a lot of scatter in the data points. This is an order of magnitude higher than the storage modulus of pure LC ($G'_{\mathrm{LC}} \sim 0.01$Pa) which varies very little with temperature. In the case of the composite at $T \approx 34$°C there is a sudden increase in G' of ~ 4 orders of magnitude to $\sim 10^3$ Pa. G' then continues to increase more slowly with cooling until $G' \sim 3 \times 10^4$ Pa. G'' increases in a similar manner until $G'' \sim 1.5 \times 10^4$ Pa. This increase in $G'(T)$ shows that the network formed by

[9]Measured with a 4cm 2° cone.
[10]Measured with a 6cm 0.5° cone.

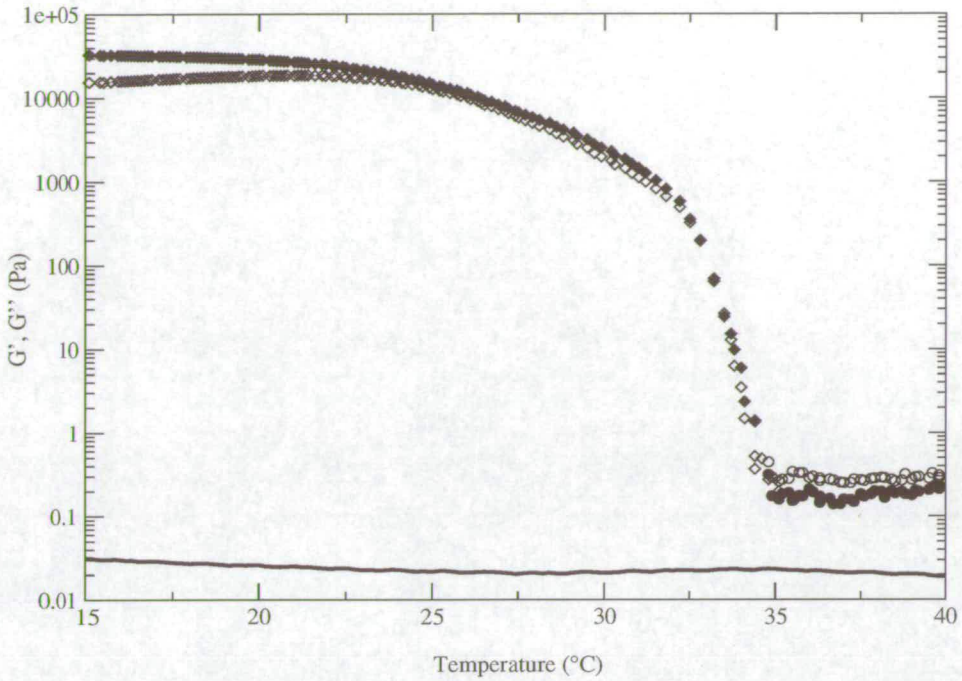

Figure 4.25: The variation of the storage modulus G' (solid symbols) and the loss modulus G'' (open symbols) of the composite with temperature compared to G' of pure 5CB (solid line). Sample with $\phi_w = 0.05$ of R=370nm particles cooled at 0.5°C/min.

the particles increases the mechanical strength of the PMMA and 5CB mixture. Most importantly, above T_{IN} $G' < G''$ and the mixture is a liquid and below T_{IN} $G' > G''$ and the mixture is a solid - as observed macroscopically.

4.6 Summary

Mixtures of PMMA particles and nematic LC 5CB have been studied using time-resolved confocal microscopy, DSC and rheological techniques. Detailed (single particle resolution) microscopy data has enabled the formation of network upon cooling from the initial isotropic dispersion to be observed. As the mixture is cooled below the IN transition, nematic domains grow, expelling particles which are transported and concentrated into boundary regions to form a three dimensional network. The rate of

nematic domain growth was found to be much slower than that in pure 5CB. Calorimetric and microscopy data suggest that this slowing down is due to the presence of hexane impurities, retained from the drying process, opening up a biphasic region in the phase diagram.

Microscopy observations show that the network can be broken up upon heating deep into the isotropic phase but that clusters of particles remain. Sedimentation of these clusters causes a density gradient of particles to form across the sample with varying height. Upon cooling a new network of particles is formed.

Rheology measurements as a function of temperature show that upon the formation of the network the composite becomes much stronger than pure LC and is stress bearing.

In the next chapter the effects of cooling rate and volume fraction of particles on the network morphology are examined.

Chapter 5

Morphology

5.1 Introduction

Upon cooling mixtures of nematic LC and PMMA colloid particles through the isotropic to nematic phase transition the particles are expelled to form the boundaries of a three dimensional network structure, as discussed in Chapter 4. Reflection confocal images [7] and bright field microscopy images [6] of these networks formed with particles of radius 150nm and 250nm respectively have been presented previously. The effects of particle concentration have been examined [7] and the characteristic length scale was found to be inversely proportional to the particle concentration. However a study in three dimensions with detailed measurements had not been carried out.

In this chapter the results are presented of an imaging study of the network structure that is formed in mixtures with $R = 390$nm particles. The use of LSCM enables the particles to be imaged up to $\sim 10^2 \mu$m deep into the sample, depending upon the amount of particles present. Optical sections or 'slices' of the network are obtained at pre-defined depths along the optical or z axis and from these three dimensional images are reconstructed. Analysis of these images allows the shape, size and topology of the cells in the network to be characterised and the properties of the particle walls to be

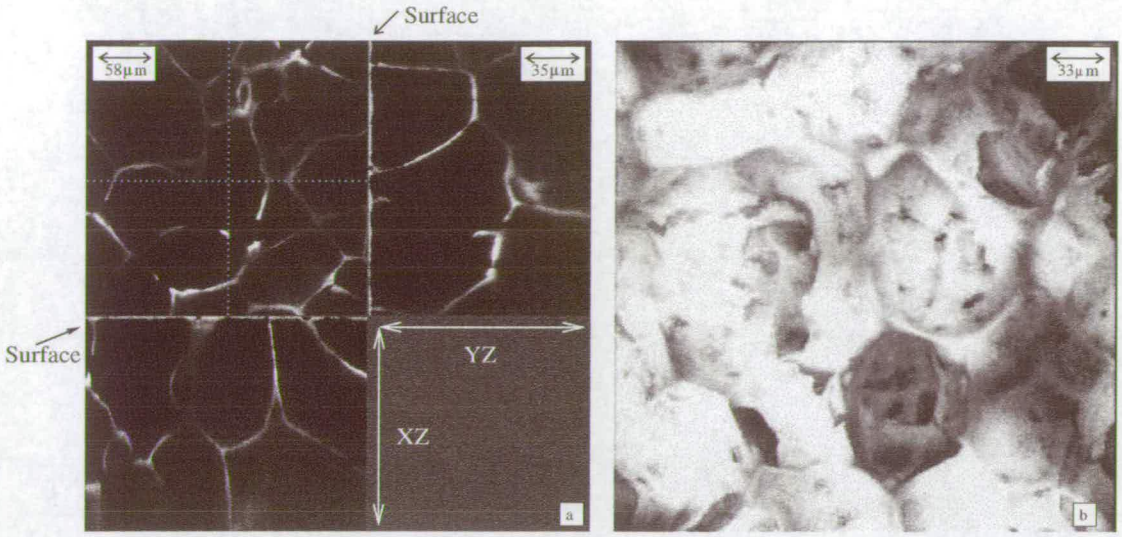

Figure 5.1: Network formation in a sample of 5CB with $\phi_w = 0.05$ of $R = 390$nm PMMA particles cooled at 1°C/min. (a) XY slice taken at 50μm below the coverslip; alongside this the XZ and YZ slices taken along the dotted lines are shown and (b) a stack of 2D slices viewed along the optical axis from the top of the sample.

examined. As the mechanical properties of cellular solids depend directly on the shape and structure of the cells this is an important step [86]. The effects of cooling rate and particle concentration on the morphology of the network that is formed are studied.

5.2 The Network

The network formed in a sample with $\phi_w = 0.05$ of R =390nm particles when cooled at 1°C/min is analysed. An optical slice taken of the network at a depth of 50μm is shown in Figure 5.1(a) and alongside this the XZ and YZ slices taken along the dotted lines are shown. In Figure 5.1(b) the image is a stack of 2D slices looking along the optical axis from the top of the sample. Boundaries of particles (white) enclose regions of LC (black) to form cells and these boundaries form an interconnected network in three dimensions. In Figure 5.1(a), taking into account the different scaling in the XY plane to that in the XZ and YZ planes, one can see that the cell shapes and sizes are similar in

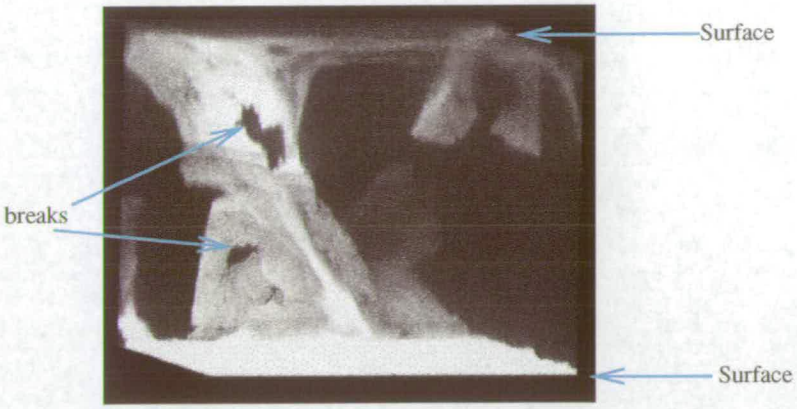

Figure 5.2: A three dimensional reconstruction of the network formed in a sample of 5CB with $\phi_w = 0.05$ of $R = 390$nm PMMA particles cooled at 1°C/min in a small sample cell. The image is a cube of volume $100\mu m^3$.

each plane - suggesting that there is no direction of anisotropy along which elongated cells or aligned cells are observed. The cell walls have random orientations in space indicating that the cells are three dimensional. These cells pack in three dimensions enabling the material to be characterised as a three dimensional cellular solid or as a foam [86, 87].

A significant amount of particles are expelled to the surface as shown by the bright regions along the edge of the XZ and YZ planes in Figure 5.1(a). This layer had been excluded from the 3D reconstruction in order to allow the network deep within the sample to be viewed. In order to examine the distribution of particles throughout the sample more closely a network was formed in a smaller sample cell and a region through the entire sample was imaged. The resulting 3D reconstruction is shown in Figure 5.2; the region imaged is a cube of $100\mu m^3$. A wall of particles is observed extending through the sample and a layer of particles is expelled to both surfaces. Breaks or perforations are observed in the walls as labelled.

Now, it is useful to define the terms used in describing and characterising a cellular solid. In Figure 5.3 a schematic diagram of a cubic cell in a closed-cell foam is shown. The edge thickness, t_e, the wall thickness, t_w, and the cell dimensions in the x, y and

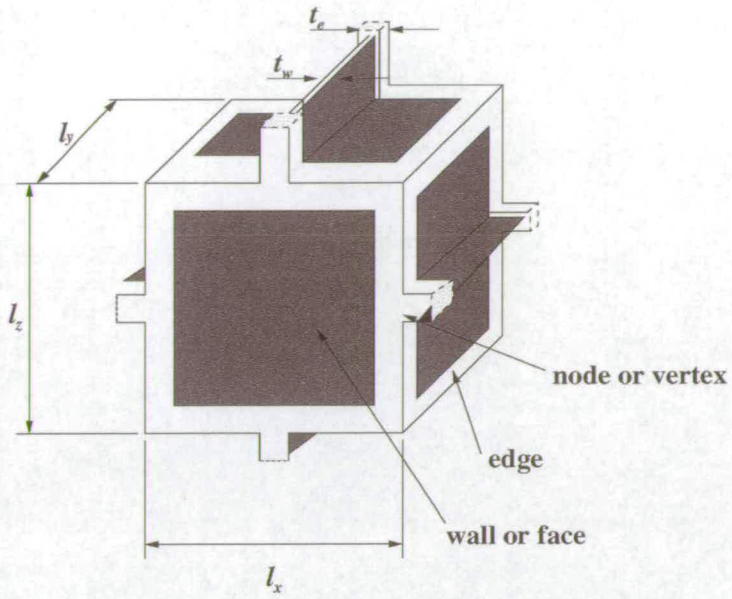

Figure 5.3: A schematic diagram of a cubic cell in a closed-cell foam. The edge thickness, t_e, the wall thickness, t_w, and the cell dimensions, l_x, l_y and l_z are defined.

z directions, l_x, l_y and l_z, are defined. The walls or faces are surrounded by edges and the edges meet at nodes or vertices. In this case the mean number of edges per face, $\bar{n}$, is 4 and the number of walls that meet at an edge, given by the wall connectivity (Z_w), is 2. This structure is described as closed cell because each cell is sealed off from neighbours by membrane-like faces or walls of particles whereas open cells are interconnected and fluid can diffuse between them [86]. In reality the distinction is not always clear; faces may be punctured or removed to some extent. During formation closed cells are formed and then they sometimes break open to form an open-cell structure.

Figure 5.4 is a 3D reconstruction of a LC cell formed in the 1°C/min network which is halved along the XY plane and viewed from this point along the Z axis; the cell appears to be closed. The faces that lie parallel to the optical axis are outlined and the edges are labelled. There are consistently three walls meeting at an edge giving

$Z_w = 3$, Figure 5.4, and there are on average $\bar{n} = 4.7$ edges to a wall or face[1]. There are often breaks appearing in the walls; one can clearly see the breaks or holes in a cell wall that lies in the XY plane in Figure 5.4 and in an optical section taken at 125μm, Figure 5.5(a), breaks in the walls are circled. It is possible that closed cells are initially formed as the sample is cooled through the IN transition and then with further cooling and compactification of the particle walls (see Chapter 4) the cell walls rupture in places. On imaging through the sample it is noticable that the cells are not symmetrical but are often distorted. In places one can clearly see that cells have coalesced towards the end of the network formation causing this asymmetry. This is demonstrated in Figure 5.5(b) in which an elongated cell is observed with a broken wall extending into the cell. The particles in the walls appear to be well packed with no LC domains observable between individual particles on the scale of the image, Figure 5.5(c). Measurements were made of the wall thickness at the centre of walls far away from nodes where thickening sometimes occurred and it was found to vary between $\sim 1.5\mu$m and $\sim 8.7\mu$m. The mean wall thickness, t_w, was calculated[2] to be $\sim 3.5\mu$m and an edge was typically found to be $\sim 4.2\mu$m thick. The diameters of the cells in the network were measured in the X, Y and Z directions at the widest points and the mean diameters were found : $l_x = 91 \pm 12\mu$m, $l_y = 107 \pm 10\mu$m and $l_z = 109 \pm 12\mu$m. The mean cell dimension[3] was found to be $l = 102 \pm 6\mu$m. The ratios of the mean cell dimensions in each direction give $\frac{l_x}{l_y} = 0.85, \frac{l_x}{l_z} = 0.84$ and $\frac{l_y}{l_z} = 0.99$ indicating again that there is no one direction of anisotropy.

It has been observed that in the network that is formed the particles form the well packed walls of a closed cell foam, enclosing particle free LC domains. Cellular structures occur naturally in wood, cork, sponge and coral and man-made structures include polymer foams [88] and metallic foams [89]. Such structures have low densities, low thermal conductivities and a high stiffness-to-weight ratio making them useful insu-

[1]Calculated from the measurement of 15 cells.
[2]20 measurements were used to gain statistics.
[3]Calculated from the measurement of 10 cells.

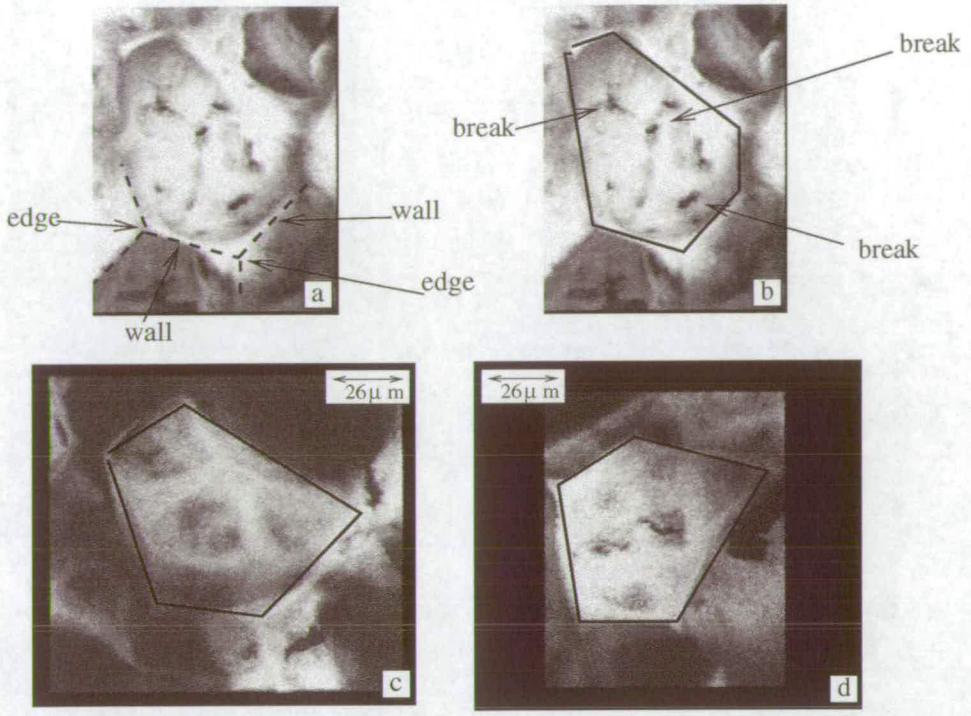

Figure 5.4: Cells in the network formed in a sample with $\phi_w = 0.05$ of R=390nm particles, (a) - (d). In (a) the edges at which 3 walls meet are labelled, in (b) breaks in the cell wall in the XY plane are pointed out and in (b) - (d) the cell walls parallel to the z axis are outlined in solid black lines.

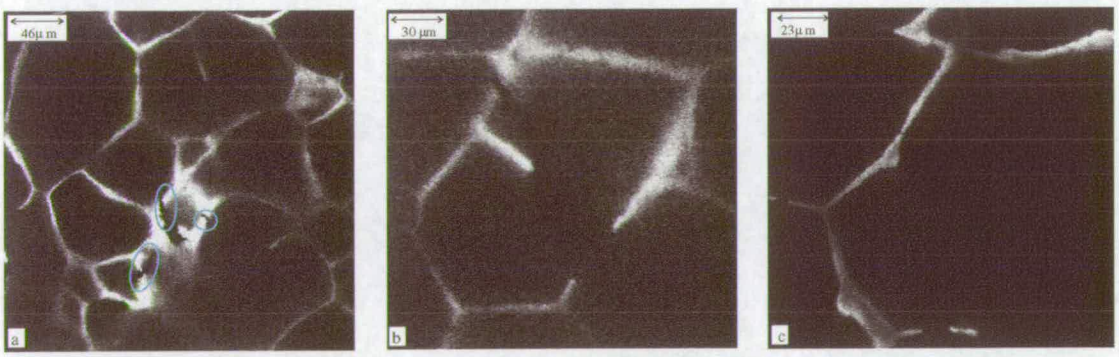

Figure 5.5: The network formed in a sample of 5CB with $\phi_w = 0.05$ of $R = 390$nm cooled at 1°C/min. Images taken at (a) 125 μm, (b) 100μm and (c) 50μm. Breaks in the walls are circled.

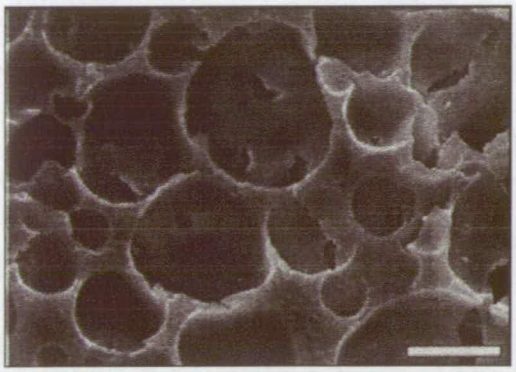

Figure 5.6: Scanning electron microscopy image of the network formed by silica particles in a particle stabilised emulsion after evaporation of the liquid components. Scale bar corresponds to 20 μm. Taken from [90].

lating, energy absorption and lightweight construction materials. One way in which such foams are made is by introducing gas bubbles which grow and stabilise causing the solid or liquid to form a structure which is then stabilised [89]. Everyday examples include bread in which a biological blowing agent, yeast, is used and meringues into which air is mechanically beaten. This process is not dissimilar to the mechanism of network formation in mixtures of PMMA and 5CB. Nematic droplets grow and coalesce in a similar manner to the gas causing the particles to form a structure and upon further cooling this structure has been seen to compactify (see Chapter 4). Similar structures have been observed in particle stabilised emulsions [90], Figure 5.6, in which particles stabilise drops of one phase and form a network which remains when the liquid components are evaporated. Motion of the particles within these networks was not observed over the timescales for which they were studied (up to 2 hours in some cases) - the particles appeared to be frozen in position. It is not understood what holds the particle network together once it is formed. It has been suggested that the force responsible is an isotropic-nematic pressure due to the LC within the walls, between particles, remaining in the isotropic phase [9]. This is a possibility; it has been shown in the previous chapter that the particles remain in the isotropic phase during the process of network formation and nuclear magnetic resonance measurements demon-

strate that a significant fraction of the LC remains in the isotropic phase after network formation [79].

To summarise, using LSCM, the network that is formed in samples with $\phi_w = 0.05$ of $R = 390$nm particles cooled at 1°C/min has been characterised as a closed cell foam. Now, the effects of cooling rate on this morphology are examined.

5.3 Variation with Cooling Rate ($\phi_w = 0.05$)

Samples with $\phi_w = 0.05$ of R=390nm particles were cooled at rates in the range $0.2 - 30$°C/min and the resulting networks were examined using LSCM. The observation is that more particles are expelled to the surface of the sample for slower cooling rates. In Figure 5.7 micrographs taken in the focal plane of the coverslip of the sample cell are shown and this trend is clearly observed. The fraction of the surface covered by particles is measured using image analysis software, Figure 5.8. Note that in samples such as that shown in Figure 5.7(a) several layers of particles form at the surface and only those in the layer at the surface of the cover slip are included in this measurement. That more particles are expelled at a slower cooling rate suggests that the network structure that is formed is a metastable state and that if the sample was cooled slowly enough macroscopic phase separation would occur as observed previously in mixtures of particles and anisotropic solvents [5, 42, 44].

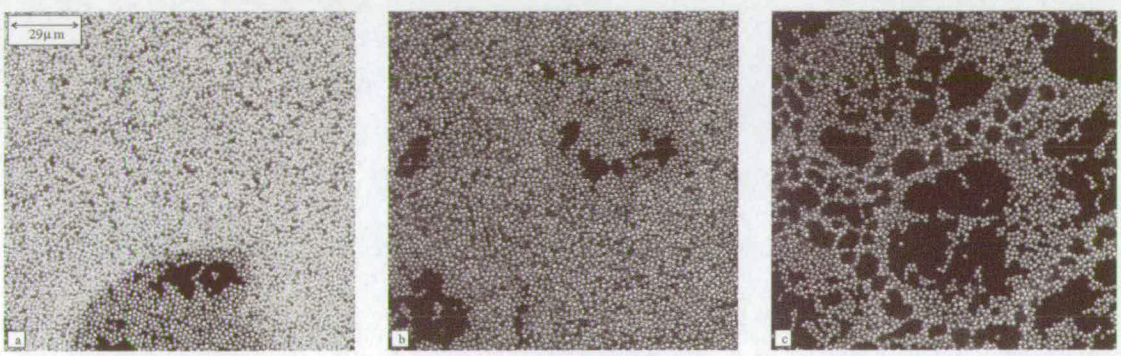

Figure 5.7: Micrographs of the sample at the surface for samples with $\phi_w = 0.05$ of R=390nm particles cooled at (a) 0.2°C/min, (b) 1°C/min and (c) 30°C/min.

The network formed deep within the sample is shown in optical sections taken at a depth of 50μm, in order of increasing cooling rate, Figure 5.9. The most obvious changing feature is the decrease in cell size with increase in cooling rate. For slow cooling rates large LC cells of $\sim 120\mu$m diameter are formed with cell walls in which

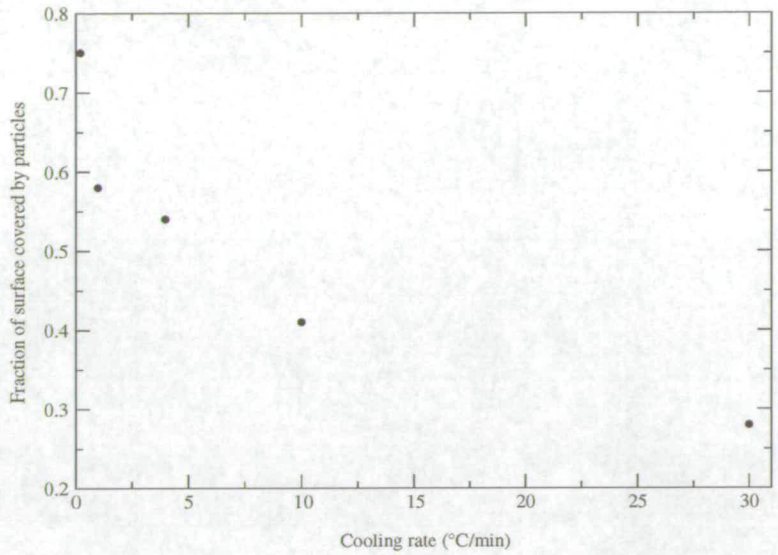

Figure 5.8: The fraction of the surface covered by particles as a function of cooling rate in samples with $\phi_w = 0.05$ of R=390nm particles measured from confocal images.

the particles appear to be well packed whereas for the fastest cooling rate the largest cells are $\sim 70\mu$m.

Measurements were made of the cell diameter in the x, y and z directions at the widest section within several samples[4] and the mean cell diameter in each direction was calculated as shown in Table 5.1. The dispersion in cell size is measured by the standard

[4]Measurement of at least 10 cells were made.

Cooling rate (°/min)	l_x	Δl_x	l_y	Δl_y	l_z	Δl_z	l	Δl	$\frac{\Delta l}{l}$
0.5	132	34	118	34	100	35	117	35	0.3
1	91	31	107	28	109	31	102	30	0.29
2	75	18	80	16	94	14	83	18	0.22
4	69	15	72	19	84	16	75	18	0.24
30	72	14	78	27	75	14	75	19	0.25

Table 5.1: Mean cell dimension l and standard deviation of cell dimension Δl for samples with $\phi_w = 0.05$ of R=390nm particles cooled at various rates. Calculated from mean cell dimensions l_x, l_y and l_z measured in the x, y and z directions respectively from confocal images.

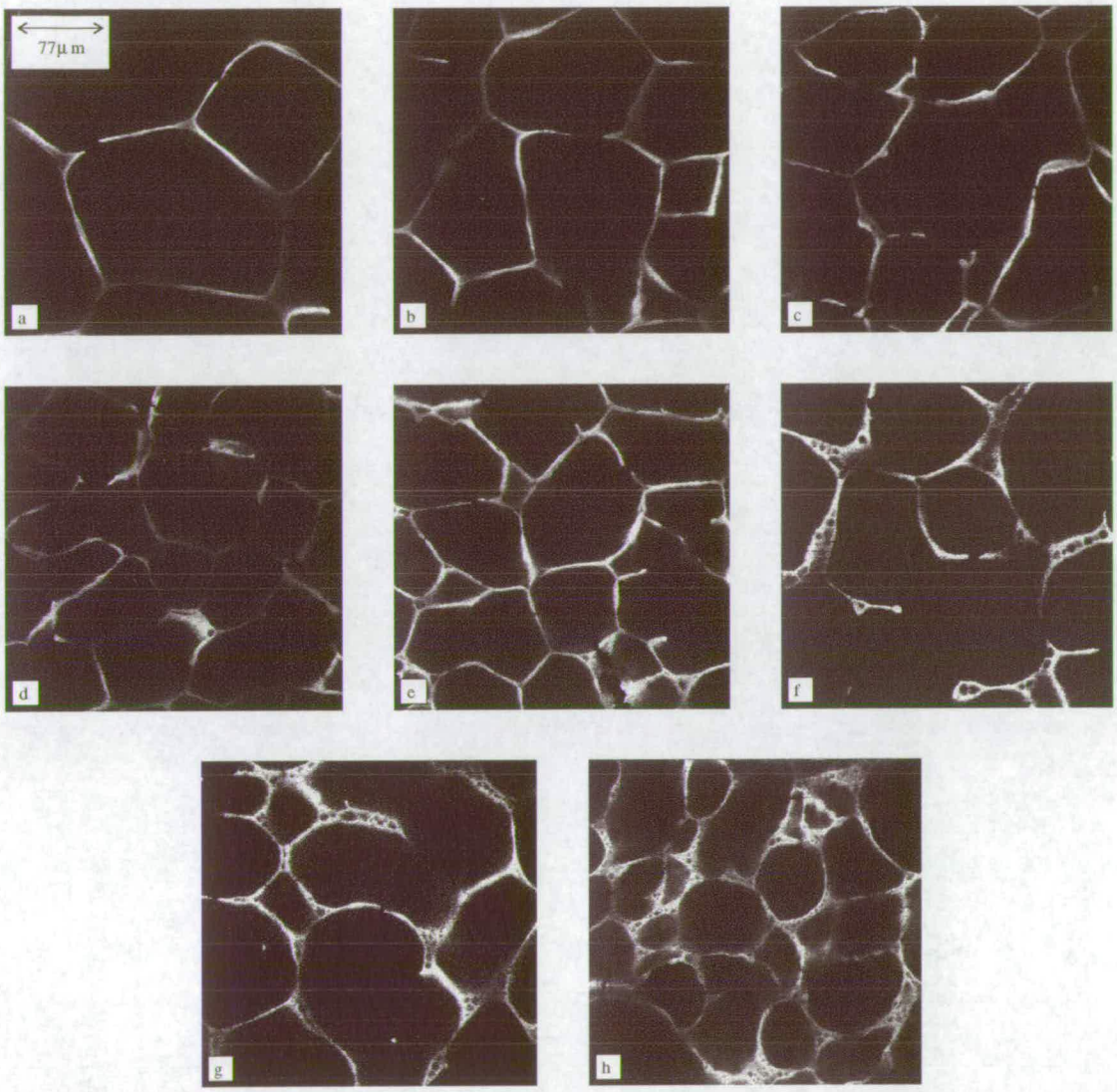

Figure 5.9: Network formed in samples with $\phi_w = 0.05$ of particles with R=390nm cooled at various rates. (a)0.2°C/min, (b)0.5°C/min, (c)1°C/min, (d)2°C/min, (e)4°C/min, (f)10°C/min, (g)20°C/min and (h)30°C/min. The scale bar in (a) applies to all other images in this figure.

Cooling rate (°/min)	$\frac{l_x}{l_z}$	$\frac{l_y}{l_z}$	$\frac{l_x}{l_y}$	mean ratio
0.5	1.32	1.18	1.12	1.21
1	0.84	0.99	0.85	0.89
2	0.80	0.85	0.94	0.86
4	0.82	0.85	0.96	0.88
30	0.97	1.05	0.92	0.98

Table 5.2: Anisotropy in mean cell dimensions l_x, l_y and l_z measured from confocal images. Sample with $\phi_w = 0.05$ of R=390nm particles cooled at various rates.

deviation in the measurements of cell diameters and it is considerable, varying from 22 - 30%. The anisotropy in the cells is characterised by the ratio of the mean cell dimension in one direction to that along another as shown in Table 5.2. This varies between 0.8 and 1.32 indicating that the cells are often asymmetrical. However, there is no ratio that is consistently higher than another demonstrating, again, that the cells are not consistently anisotropic or elongated in one direction. The larger values for the 0.5°C/min cooling rate could be attributed to size or surface effects because the sample cell is now only $\sim 4\times$ the mean cell dimension. The mean value of the diameters in the x, y and z directions was taken to represent the mean cell dimension l, Table 5.1 and Figure 5.10. There is a sharp decrease in cell size from $\sim 130\mu$m to $\sim 75\mu$m with a decrease in cooling rate from 0.5°C/min to 4°C/min, however decreasing the cooling rate by another order of magnitude (4 - 30°C/min) sees the change in cell size become negligible.

Although the cell size hardly decreased any further when the cooling rate reaches ~2°C/min another change is observed. When the cooling rate is increased beyond this point small LC cells begin to be observed in the nodes of the larger cells. Although previous studies [7] have not examined the effects of cooling rate or used three dimensional information, holes within the walls of particles are visible in the micrographs presented. Higher magnification images of the nodes of the networks formed

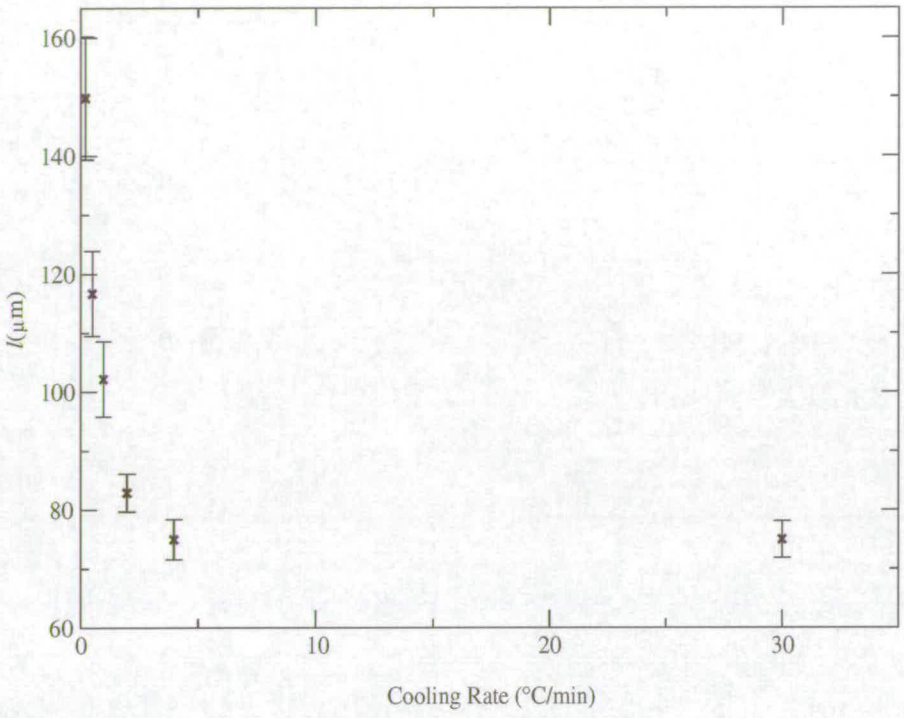

Figure 5.10: Variation of cell size with cooling rate

at various cooling rates are shown in Figure 5.11. For a cooling rate of 0.5°C/min the resulting nodes are shown in Figure 5.11(a) and (b). The walls are made up of close packed particles and are of thickness $\sim 3.4\mu$m and the edges $\sim 4.4\mu$m. When the cooling rate is increased to 2°C/min, Figure 5.11(c) and (d), there are mostly walls of close packed particles but some smaller cells of mean diameter $\sim 11\mu$m appear at the nodes. The wall thickness is $\sim 2.9\mu$m and the edge thickness is $\sim 3.8\mu$m. For a cooling rate of 4°C/min, Figure 5.11(e) and (f), these smaller cells appear more frequently; there are 6 small cells observed in the $308 \times 308\mu$m image shown in Figure 5.11(e) compared to only 1 for the network observed after cooling at 2°C/min, Figure 5.11(d). The cells also decrease in diameter to $\sim 9\mu$m from $\sim 11\mu$m. For the fastest cooling rate of 30°C/min an increasing number of small cells are observed at the nodes and now also within the walls, as shown in Figures 5.11 (g) and (h) and in the three dimensional reconstruction in Figure 5.12. These holes are $\sim 4\mu$m and $\sim 13\mu$m in

diameter[5]. Small LC regions are observed between the particles in the walls of size $\sim 1 - 2\mu$m that were not visible in the well packed interfaces imaged on the same scale in networks formed at slower cooling rates. Including these small LC cells that are observed within the walls and nodes a new mean cell dimension can be calculated and its variation with cooling rate is shown in Figure 5.13. Whereas for the large cells an increase in the cooling rate from 4°C/min to 30°C/min showed negligble change in cell size now a gradual decrease in observed from ~ 38 to $\sim 4.5\mu$m.

The heirarchical order of a structure or a material may be defined as the number of levels, n, of scale with recognised structure [91]. When a material is viewed as a continuum then $n = 0$ and for a foam or honeycomb structure $n = 1$. For a material in which the cell walls contain smaller cells then $n = 2$. The network structure observed at fast cooling rates is therefore a cellular material of heirarchical nature and the heirarchical order n or the number of levels of cells within cells increases with cooling rate. From the images shown in Figures 5.9 and 5.11 it is estimated that for cooling rates in the range $0.5 - 1$°C/min $n = 1$, for the cooling rates of 2 and 4°C/min $n = 2$ and for the fastest cooling rate of 30°C/min $n = 3$. In order to quantify this the distribution of cell sizes for each cooling rate is shown in Figure 5.14. The single peak in the histograms of samples cooled at 0.5°C/min and 1°C/min agrees with the estimated $n = 1$. The appearance of 2 peaks in the distribution for the samples cooled at 2°C/min and 4°C/min is indicative of cells on 2 scales and supports the $n = 2$ estimated from the images. The distribution for the samples cooled at 30°C/min only shows 1 peak because the cell size is dominated by the small cells and the scale between cells at the smaller level is not distinguishable. The $n = 3$ domains are likely to be only slightly larger than the particle size, creating a practical complication.

For all cooling rates examined 3 walls are consistently observed to meet at an edge, giving $Z_w = 3$.

[5]All dimensions were calculated from at least 10 measurements

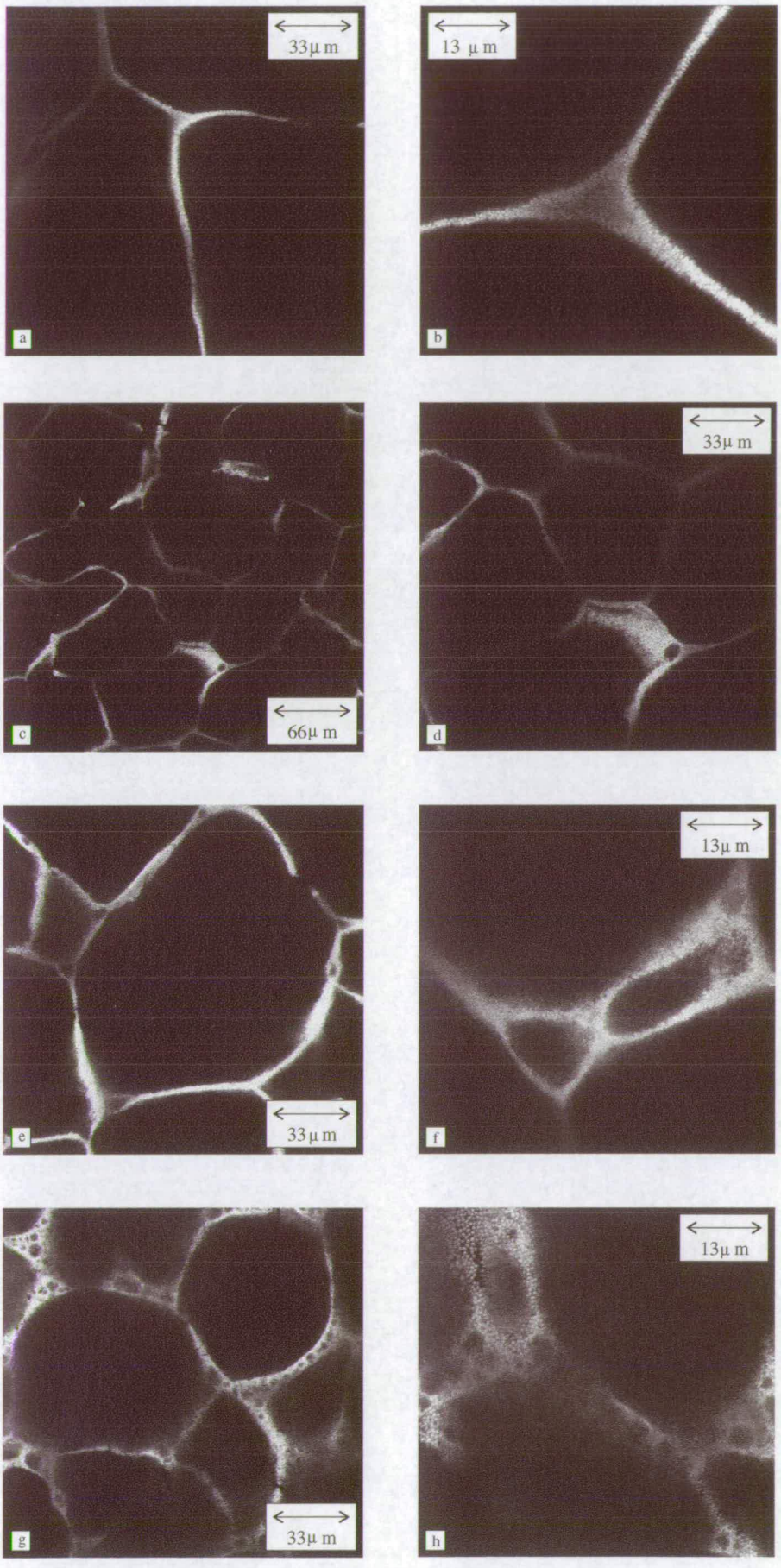

Figure 5.11: The nodes where walls of particles meet in the networks formed in samples with $\phi_w = 0.05$ of R=390nm particles cooled at (a), (b) 0.5°C/min, (c), (d) 2°C/min, (e), (f) 4°C/min and (g), (h) 30°C /min.

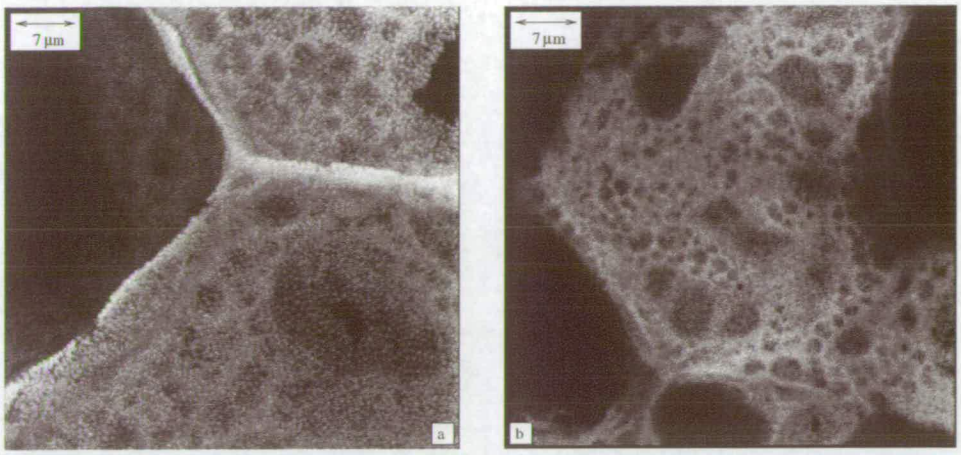

Figure 5.12: 3D reconstruction of nodes in the network formed in a sample with $\phi_w = 0.05$ of R=390nm particles cooled at 30°C/min.

When mixtures of LC and hydrocarbons are cooled they spend time in a biphasic region [51]. When cooled at a slower rate they spend more time in this region than those cooled at quicker rates and the nematic domains have more time to grow and coalesce [92] before they impinge and particles at the interfaces prevent further coalesence (see Chapter 4). This is consistent with the increase in cell size with decrease in cooling rate that is observed. A greater distribution in cell sizes in observed in the networks formed at faster cooling rates, characterised by the heirarchical nature, and this can be understood because the mixtures spend less time in the biphasic region and the particles have less time to move and allow further growth of domains. Hence the size of a particular cell in these networks is dependent upon the particle distribution around the LC domain as it grows in the biphasic region. That Anderson [7] observed a smaller distribution in cell size for faster cooling rates may be due to the limited nature of the microscopy study.

The rate at which a sample is cooled through the IN transition appears to have a significant effect upon the morphology of the network structure that is formed - both in terms of the size of the LC cells formed and the structure of the particulate walls. Now the effects of particle concentration on this morphology are examined.

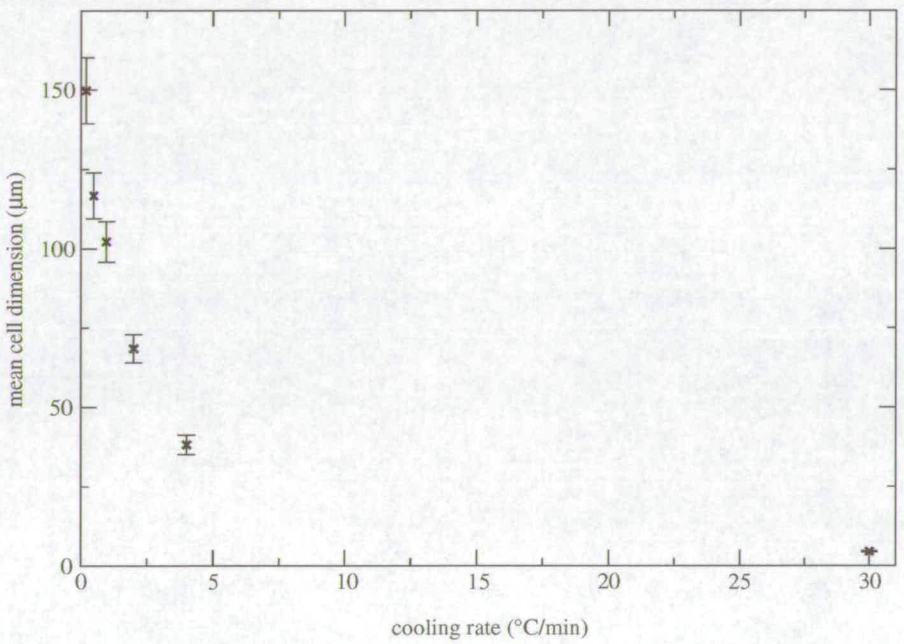

Figure 5.13: Variation of cell size with cooling rate including the smaller cells observed within the walls and nodes.

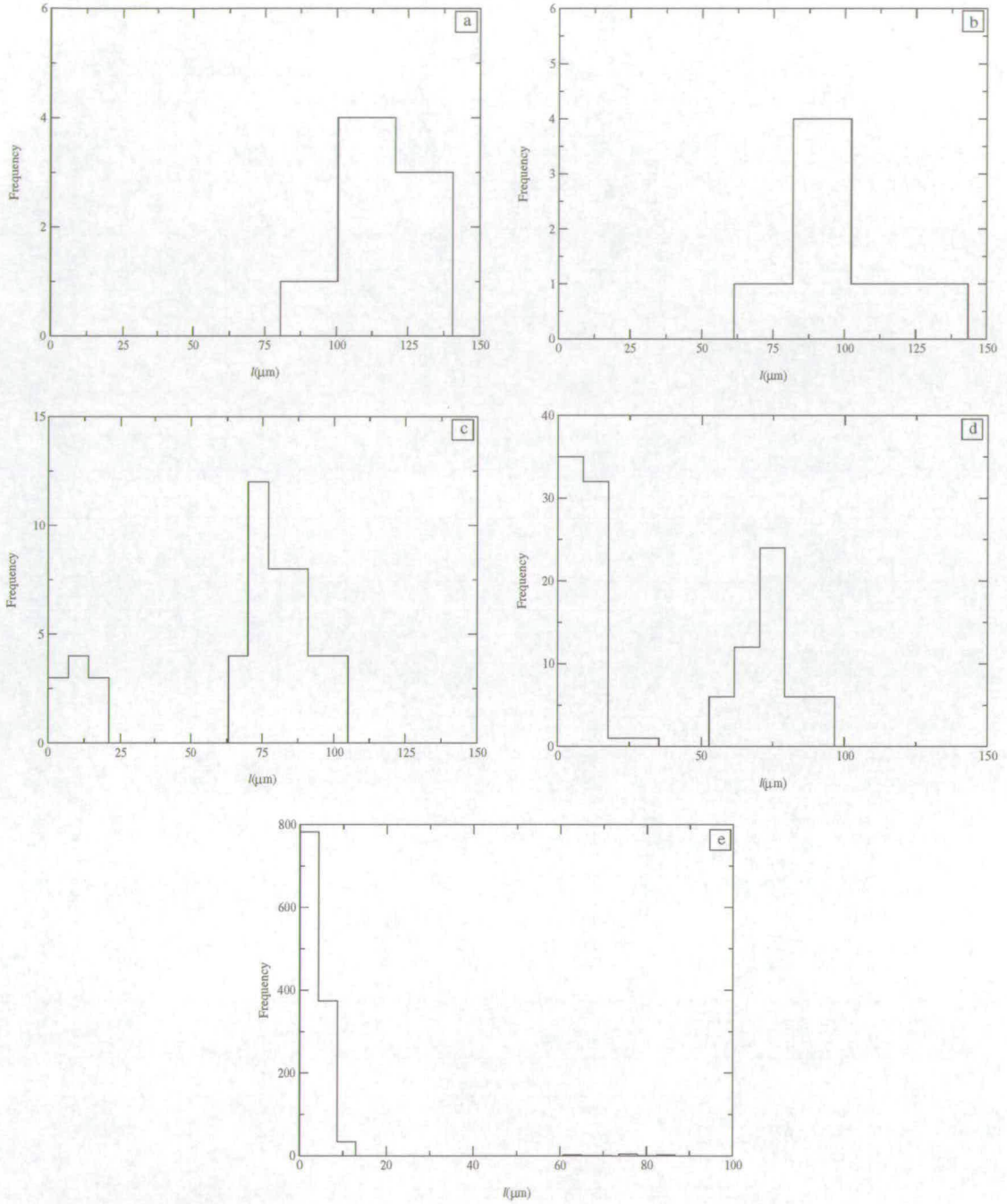

Figure 5.14: The distribution of cell sizes in samples with $\phi_w = 0.05$ of $R = 390$nm particles cooled at (a) 0.5°C/min, (b) 1°C/min, (c) 2°C/min, (d) 4°C/min and (e) 30°C/min.

5.4 Variation with Particle Concentration

Samples with $\phi_w = 0.025 - 0.15$ of R=390nm particles were cooled at rates in the range $0.5 - 30$°C/min and the resulting networks were imaged using LSCM. The network structure deep within the sample is shown in the optical sections of these networks taken at a depth of 50μm in Figure 5.15. These images are shown alongside images of the $\phi_w = 0.05$ networks that have already been discussed, for comparison. The most obvious trends observed are that for a fixed cooling rate the cell size decreases with increasing particle concentration and the walls and edges thicken, Table 5.3. Measurements of the cell diameter as a function of ϕ_w are shown in Figure 5.19 for a fixed cooling rate. The lines of best fit for each cooling rate are $l \propto \frac{1}{\phi_w}$. The data for the slowest cooling rate (0.5°C/min) and therefore the largest cell sizes is not such a good fit; the regression coefficient = 0.73 compared to 0.97 and 0.99 for the cooling rates of 3°C/min and 30°C/min respectively. This is possibly because the sample cell $\sim 4\times$ the largest cell size and surface effects begin to play a role. These relationships between l and ϕ_w are consistent with measurements from single confocal slices [7]; for mixtures of $R = 150$nm particles and 5CB cooled under ambient conditions[6] l was found $\propto \frac{4.88}{\phi_w}$. If it is considered that the number of particles needed to cover the surface area of a cell is $\propto l^2$ and the number of cells formed is $\propto \frac{1}{l^3}$ then a $\frac{1}{l}$ dependence of ϕ_w is sensible.

The same dependence of cell size on cooling rate is observed for all ϕ_w[7]. A sharp decrease in cell size with decrease in cooling rate from 0.5°C/min to 4°C/min and then a slower decrease is observed as was the case for $\phi_w = 0.05$, Figure 5.17.

[6]Experiments show that a sample cooled under ambient conditions passes through the IN phase transition at a rate of $\sim$ 4°C/min.

[7]For $\phi_w = 0.025$ the big cells formed at the slower cooling rates were too big to measure, however the heirarchical nature within the walls could still be observed.

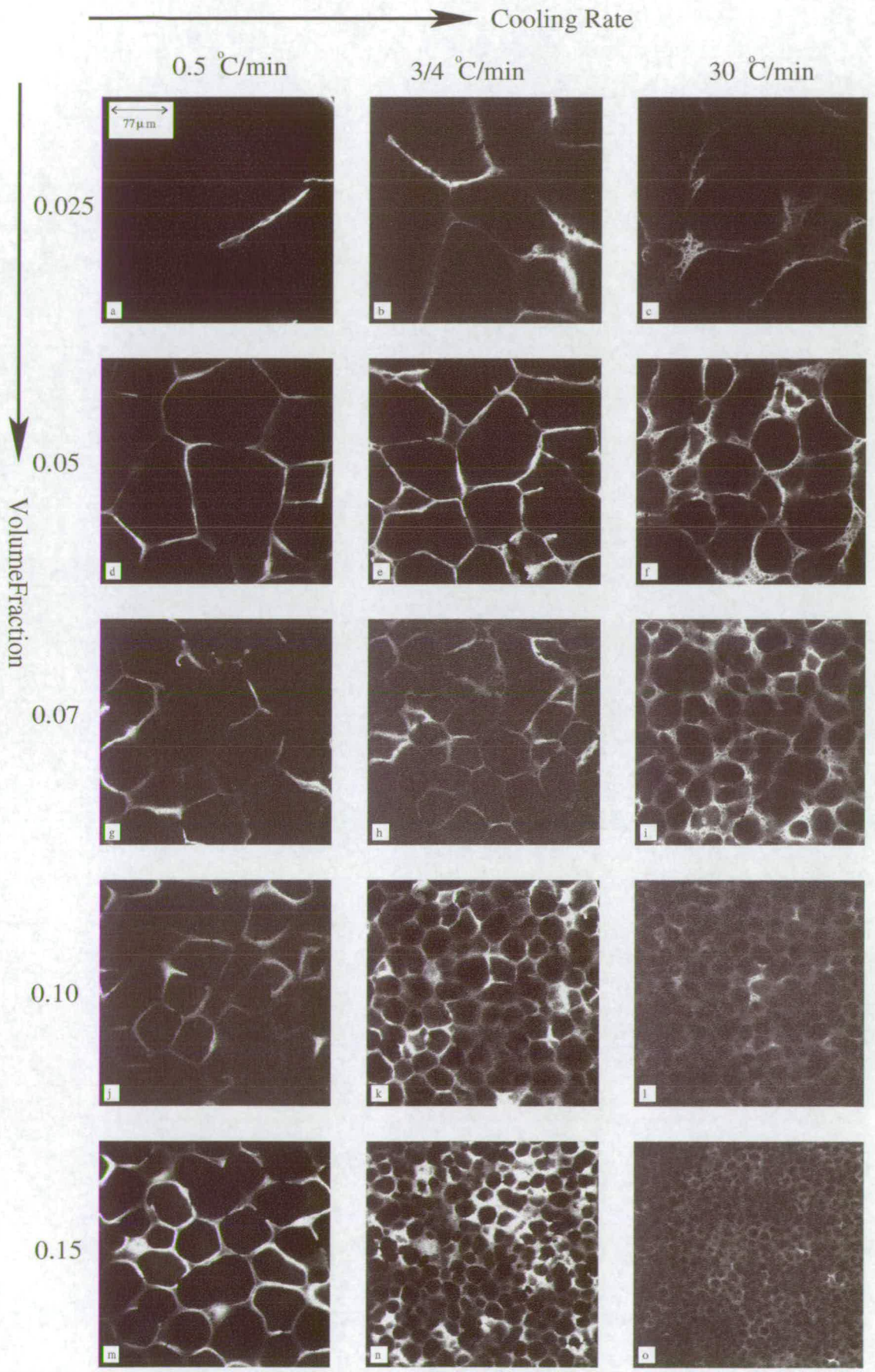

Figure 5.15: Optical sections of the network formed in samples of 5CB and R=390nm particles. (a)$\phi_w = 0.025$, 0.5°C/min, (b)$\phi_w = 0.025$, 3°C/min , (c)$\phi_w = 0.025$, 30°C/min , (d)$\phi_w = 0.05$, 0.5°C, (e)$\phi_w = 0.05$, 4°C/min, (f)$\phi_w = 0.05$, 30°C/min, (g)$\phi_w = 0.07$, 0.5°C/min, (h)$\phi_w = 0.07$, 3°C/min, (i) $\phi_w = 0.07$, 30°C/min, (j)$\phi_w = 0.10$, 0.5°C/min, (k) $\phi_w = 0.10$, 3°C/min, (l) $\phi_w = 0.1$,

ϕ_w	$t_e(\mu\text{m})$	$t_w(\mu\text{m})$
0.05	4.4	3.1
0.07	4.7	3.2
0.1	6.3	4.1
0.15	7.6	4.7

Table 5.3: The thickness of the walls and edges in samples of various ϕ_w cooled at 0.5°C/min. Measured from confocal images.

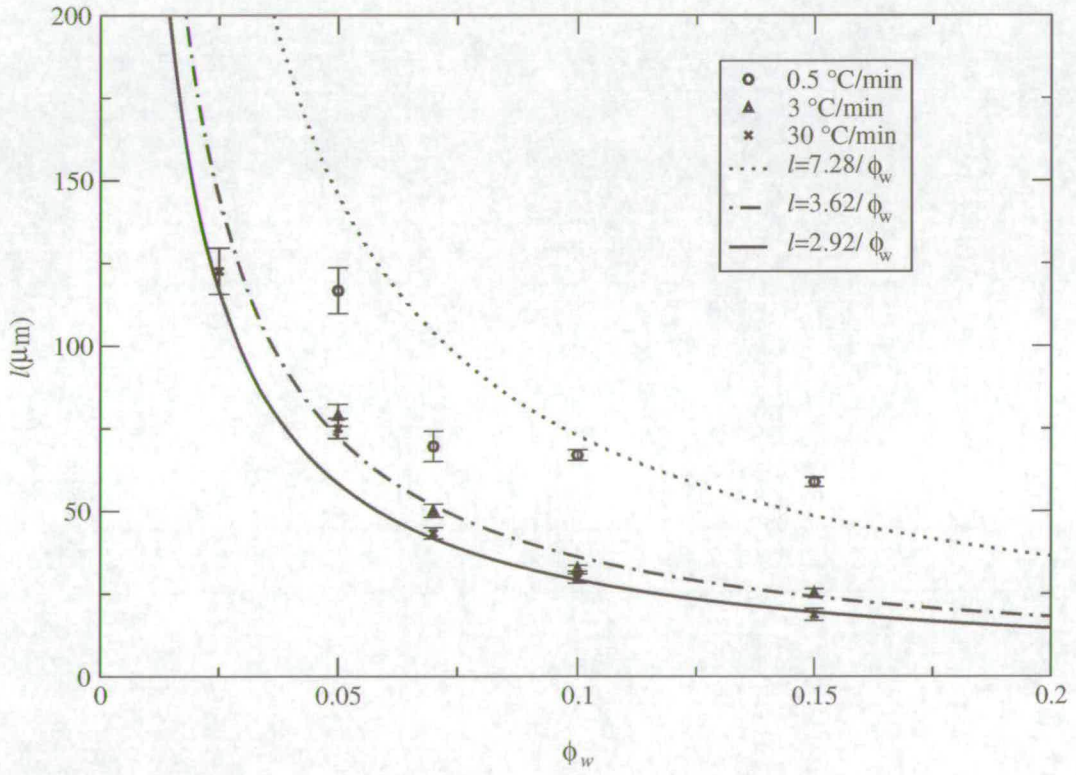

Figure 5.16: The variation of mean cell dimension l with ϕ_w for samples of $R = 390$nm particles cooled at various rates.

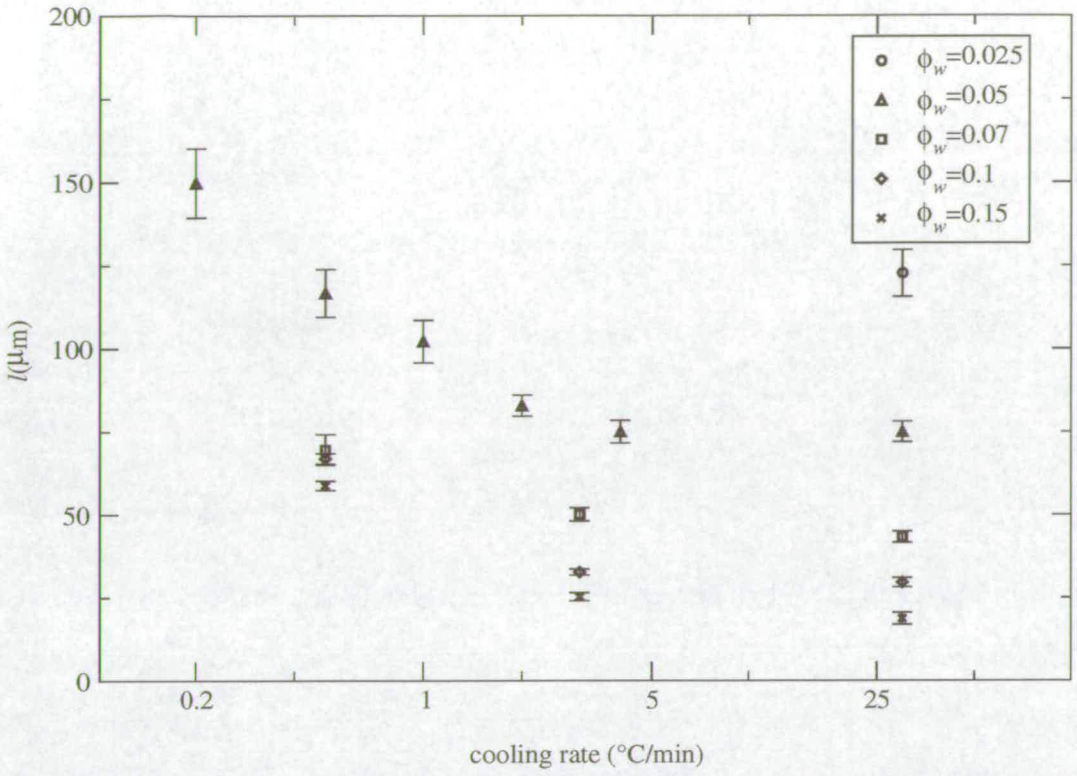

Figure 5.17: The variation of mean cell dimension l with cooling rate for samples with $\phi_w = 0.025 - 0.15$ of $R = 390$nm particles.

The general features of the network morphology for each cooling rate and particle concentration studied are summarised in Table 5.4[8]. For the smallest particle concentration ($\phi_w = 0.025$) struts of particles rather than walls of particles are observed as shown in the optical slice shown in Figure 5.18(a), and then with increasing depth walls develop, Figures 5.18(b) and (c). This is possibly due to a lower particle concentration at the top of the sample as a result of sedimentation, and hence fewer particles being available to form cell walls. The same heirarchical nature is observed for the lower particle concentrations ($\phi_w = 0.025$ and 0.07) as for $\phi_w = 0.05$. One degree of hierarchy is observed for the cooling rate of 3°C/min and two for the fastest cooling rate of 30°C/min. However, for samples with $\phi_w = 0.10$ of particles smaller cells within the nodes are only observed for the fastest rate of 30°C/min. For the highest particle concentration

[8]More detailed descriptions and images are given in Appendix A.

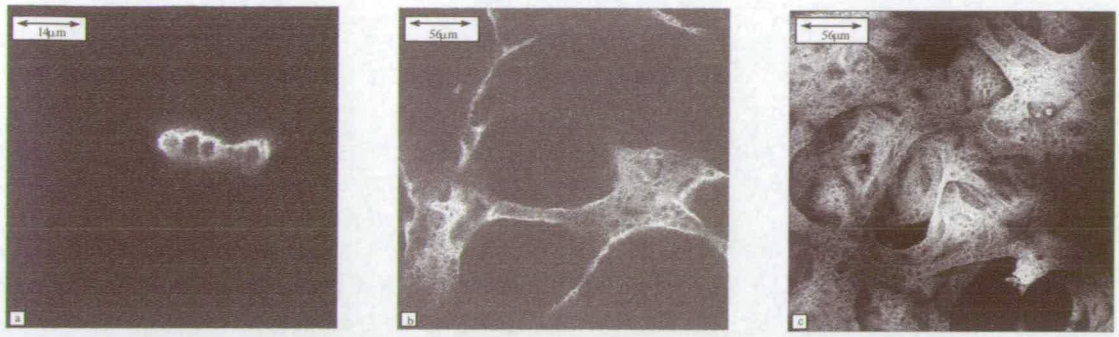

Figure 5.18: The networks formed in samples with $\phi_w = 0.025$ of R=390nm particles cooled at 30°C/min. (a) a strut imaged at 30μm, (b) walls imaged at 100μm and (c) a 3D reconstruction.

($\phi_w = 0.15$) no hierarchy is observed for any of the cooling rates examined. This may be because the particles are too large relative to the size of the nematic domains. However, particles do appear less well packed at the nodes in the $\phi_w = 0.15$, 30°C/min network and gaps of $\sim 1 - 2\mu$m are observed. For each particle concentration studied the distribution of cell size, taking into account the hierarchy present, increased with increasing cooling rate, Table 5.4, as observed for the $\phi_w = 0.05$ mixtures.

The growth of nematic domains when cooling these mixtures is impeded by other domains with particles at the interfaces preventing coalescence. When the concentration of particles increases LC domains in general grow to a smaller size before this occurs. This is consistent with the decrease in mean cell diameter with increase in particle concentration that is observed in these mixtures of PMMA and 5CB.

Figure 5.19 shows the variation of cell shape as a function of ϕ_w at fixed cooling rate 0.5°C/min. The cells appear to become more spherical with increasing particle concentration. This can be observed by examining the change in edge shape for these networks shown in Figure 5.20: the corners do indeed appear to be becoming less angular and more spherical in shape. This is consistent with wet foams [93], in which as the fraction of liquid increases the swelling of the edges leads to the extreme limit of a wet foam in which the bubbles have recovered their spherical shape. The way in which

ϕ_w	Cooling rate (°C/min)	small cells (μm)	n
0.025	0.5	none	1
0.025	3	8.9	2
0.025	30	1 and 10	3
0.07	0.5	none	1
0.07	3	9.6	2
0.07	30	0.5 and 4	3
0.10	0.5	none	1
0.10	3	none	1
0.10	30	2.4	2
0.15	0.5	none	1
0.15	3	none	1
0.15	30	none	1

Table 5.4: Summary of information on networks formed at various rates and with $\phi_w = 0.025 - 0.15$.

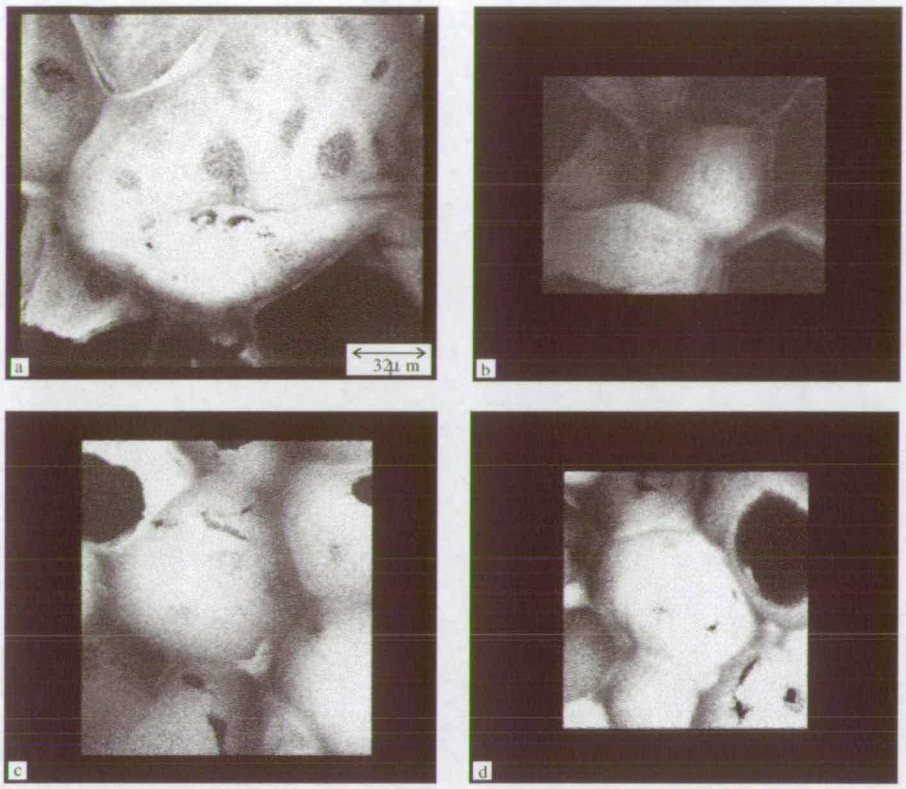

Figure 5.19: 3D reconstructions of cells formed in networks of samples with various ϕ_w of R=390nm particles cooled at 0.5°C/min. (a) $\phi_w = 0.05$, (b) $\phi_w = 0.07$, (c) $\phi_w = 0.1$ and (d) $\phi_w = 0.15$. The scale is the same in all images.

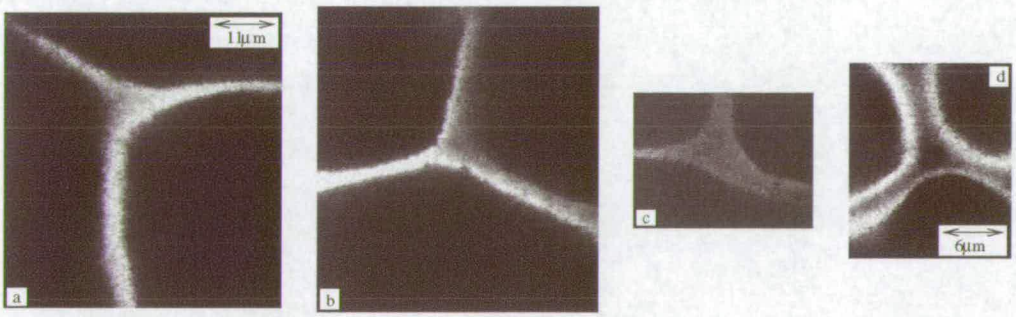

Figure 5.20: Micrographs of the plateau regions formed between cells in networks of samples with various ϕ_w of R=390nm particles cooled at 0.5°C/min. (a) $\phi_w = 0.05$, (b) $\phi_w = 0.07$, (c) $\phi_w = 0.1$ and (d) $\phi_w = 0.15$.

ϕ_w	$t_e(\mu\text{m})$	$t_w(\mu\text{m})$	Z_w	$\bar{n}$	l	ϕ_e
0.05	4.4	3.1	3	4.7	116.7	0.08
0.07	4.7	3.3	3	4.7	69.6	0.13
0.1	6.3	4.1	3	4.8	66.9	0.19
0.15	7.6	4.7	3	5.1	58.8	0.26

Table 5.5: The fraction, ϕ_e, of $R = 390$nm particles contained in the cell edges of the network that is formed in samples with various ϕ_w cooled at 0.5°C/min calculated from dimensions measured from confocal images.

the solid is distributed in the cell faces and edges of the network is an important way in which to characterise the properties of the cellular solid. The fraction of material in the cell edges is given by

$$\phi_e = \frac{t_e^2}{t_e^2 + \frac{Z_w}{\bar{n}} t_w l}, \tag{5.1}$$

where Z_w is the number of faces that meet at an edge and $\bar{n}$ is the mean number of edges per face [86]. This is calculated for samples of various ϕ_w cooled at 0.5°C/min, Table 5.5[9] and with an increase in particle concentration an increase in the fraction of particles contained in the edges of the network is observed.

Three dimensional reconstructions of the network structure formed from samples with increasing ϕ_w cooled at 3°C/min are shown in Figure 5.21. The walls appear to have a large number of perforations for the lowest $\phi_w = 0.025$ but as ϕ_w increases fewer perforations are observed. When compared to various cellular images [86] the cells in the network in Figure 5.21(a) appear to be partially closed and partially open, but with increasing particle concentration the network resembles more closely a closed cell structure. This suggests that for greater particle concentrations the mechanical

[9]Calculated from 40 measurements.

properties are those of a network of edges and walls while for lower concentrations they are those of a network of edges.

It is clear that the fraction of particles present plays a role in determining the structure of the network that is formed - both in terms of the distribution of the solid in the edges and walls and in the size of the LC cells. For high volume fractions the higher hierarchy (small) LC domains become comparable to the particle size creating qualitative changes in structure.

5.5 Summary

The network structure formed when mixtures of PMMA and 5CB are cooled through the IN transition is that of a cellular foam [86]. This network has been found to be cooling-rate and particle concentration dependent. A decrease in cell size with increase in cooling rate was found. At high cooling rates, a hierarchical cellular structure is formed with small cells appearing within the walls and nodes of big cells. Except for the slowest cooling rate studied the mean cell diameter is found to be inversely proportional to the particle concentration. With an increase in the amount of particles present the amount of perforations in the cell walls decreases. As ϕ_w increases the cells become more spherical in shape with the fraction of particles in the cell edges increasing.

The mechanical properties of cellular solids depend upon the morphological characteristics of the cellular structure. In the next chapter the mechanical properties of the structure are examined and discussed alongside the results of this imaging study.

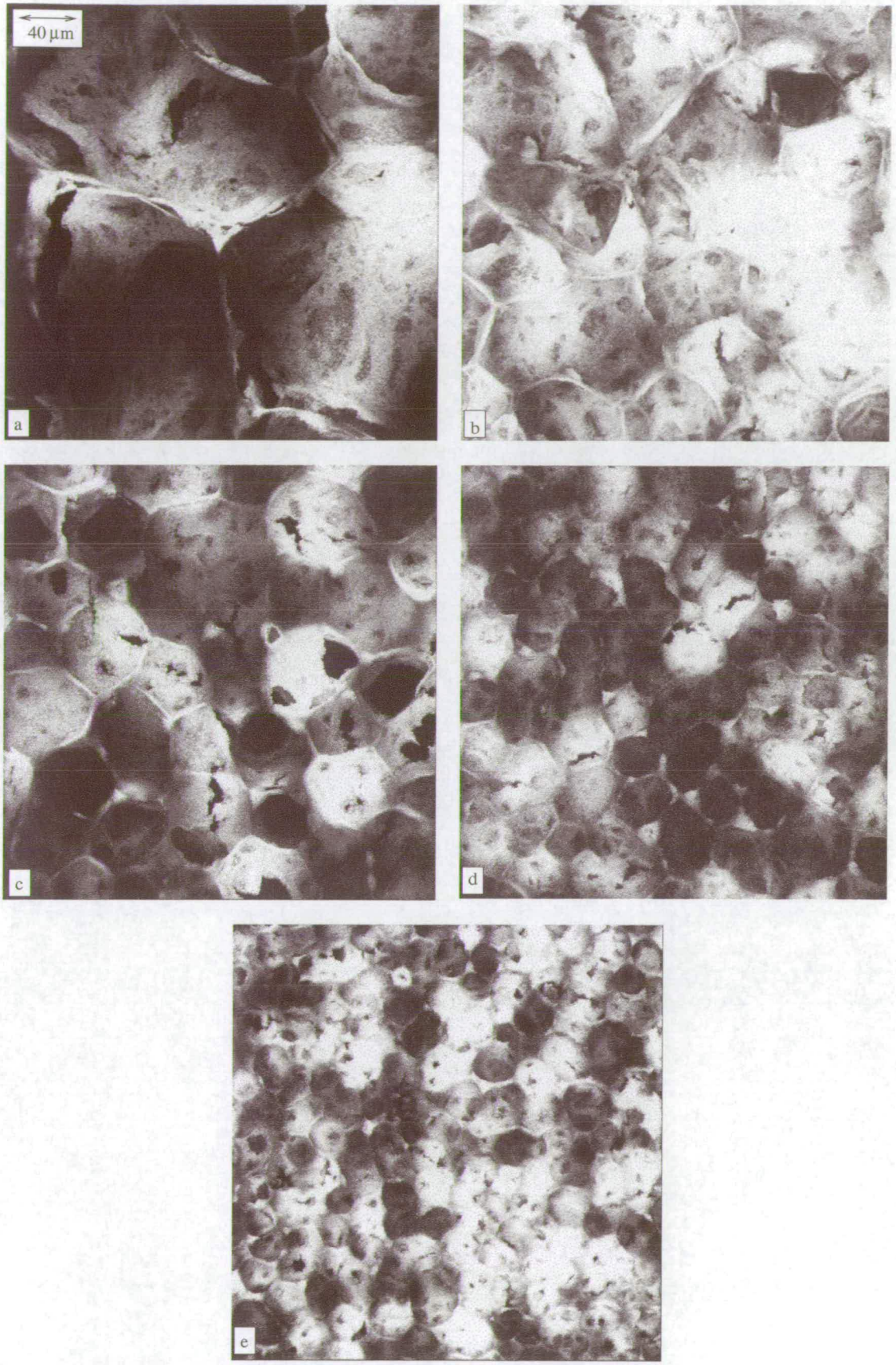

Figure 5.21: 3D reconstructions of cells formed in networks of samples with various ϕ_w of R=390nm particles cooled at 3°C/min. (a) $\phi_w = 0.025$, (b) $\phi_w = 0.05$, (c) $\phi_w = 0.07$, (d) $\phi_w = 0.1$ and (e) $\phi_w = 0.15$.

Chapter 6

Mechanical Properties

6.1 Introduction

When mixtures of PMMA and 5CB are cooled through the IN transition they have been found to form a soft solid which can support its own weight and be engraved [6]. As was shown in section 4.5 the elastic modulus, G', of the composites is much greater than that of pure LC ($\sim 10^4$Pa compared to ~ 0.01Pa). This represents a significant storage of energy in the sample. Rheological measurements to date [6, 8, 9, 79] have been carried out as the sample is cooled from the isotropic to the nematic phase, possibly affecting the network as it formed. The variation with cooling rate had still to be investigated.

The morphology of the network formed in these mixtures has been observed in the previous chapter to be cooling rate and particle concentration dependent; it is therefore expected that G' will be dependent upon the same factors. In this chapter, a preliminary study of the variation of the mechanical properties of these composites with cooling rate and particle concentration is reported. Oscillatory rheological measurements are used to measure the response of the network formed in mixtures with $R = 370$nm particles to small deformations. A strain amplitude of 0.5% and a frequency of 1 Hz

are used to ensure that the elastic response of the composites in the linear visocelastic region is measured. From these measurements values of the elastic and viscous moduli are extracted. These results are then discussed alongside the morphological information extracted from the imaging study reported in Chapter 5.

It should be stressed that the data presented in this chapter represent only a preliminary, exploratory study of the rheology of these composites. While these results offer some support for treating these composites as heirarchical cellular solids, there is as yet no coherent understanding of all results taken together. They are nevertheless included in this thesis for completeness.

6.2 Variation of Mechanical Properties with Cooling Rate

Samples were cooled at various rates in the rheometer. Measurements were made while the sample was cooled from 45°C at time $t = 0$ to 15°C at $t = t_{final} = \frac{30^{\circ}}{cooling\ rate}$, Figure 6.1 (see section 3.6.4)[1]. For cooling rates in the range $0.1 - 2$°C/min $G' \sim 3 \times 10^4$ Pa. For a cooling rate of 3°C/min a decrease in the modulus is observed and $G' \sim 5 \times 10^3$ Pa. A sample cooled at 30°C/min gave G' at least two orders of magnitude lower ($G' \sim 100$ Pa) than that at the slowest cooling rate. It is evident that the cooling rate does affect the mechanical properties of the structure. However, for the faster cooling rates it was not possible to collect sufficient data points during the measurement. Furthermore as the measurements were strain controlled by a feedback mechanism there are concerns that the stress applied to the composite during the isotropic to nematic transition (when large changes in the sample occur quickly) might be too high and cause damage to the network. As a result, further rheological measurements were

[1]Measurements were not possible in the isotropic phase with the 4cm cone, however measurements with a 6cm cone give $G' \sim 0.1$Pa for the composite in the isotropic phase (see sections 3.6.4 and 4.5).

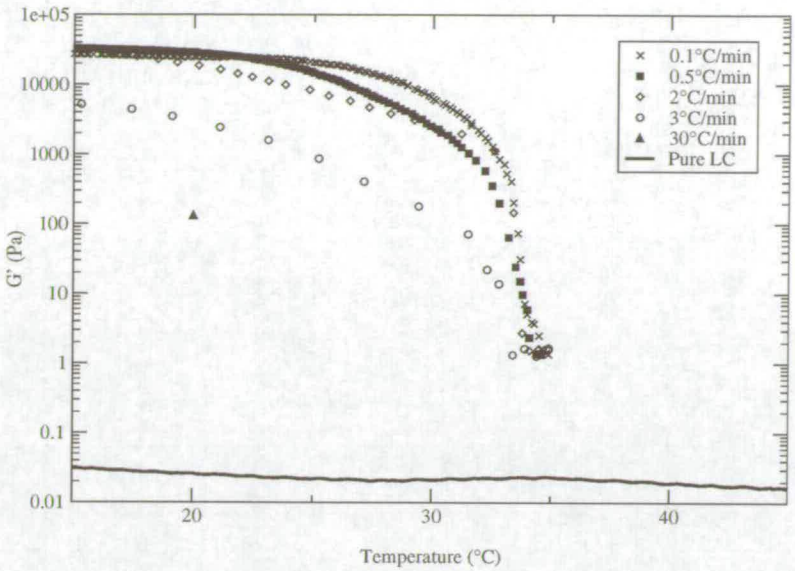

Figure 6.1: The variation of G' with temperature, at cooling rates in the range $0.1 - 30$°C/min. Samples with $\phi_w = 0.05$ of $R = 370$nm particles were used. Measurements were carried out at 1 Hz with a strain amplitude of 0.5% during the cooling process.

only carried out after the sample had been cooled to 20°C and the network had already been formed (see section 3.6.4).

Figure 6.2 shows the variation of G' with time for samples cooled at 0.5°C/min, 3°C/min and 30°C/min; $t = 0$ is the time at which the sample has been at 20°C for 5 minutes. Although the variability between measurements is large, the orders of magnitude remain the same. For the slow cooling rate of 0.5°C/min, G' decreased steadily from $\sim 10^4$Pa to $\sim 3 \times 10^3$ Pa over the 30 minute experiment. Samples cooled at 30°C/min decreased sharply by ~ 2 orders of magnitude from $\sim 10^4$ Pa over the first 1000s and then more slowly over the remaining 800s to ~ 40Pa. The reason for this decrease over the measurement is not clear, nor is the reason for its variation between samples. That the fast cooling rate data shows such a strong time dependence leads us to attach a '?' to all data points taken at this cooling rate to indicate a degree of doubt. Results were averaged over the last 600s to get a value of G' for each measurement. Then the mean and error in the mean were calculated for all samples cooled at the same rate.

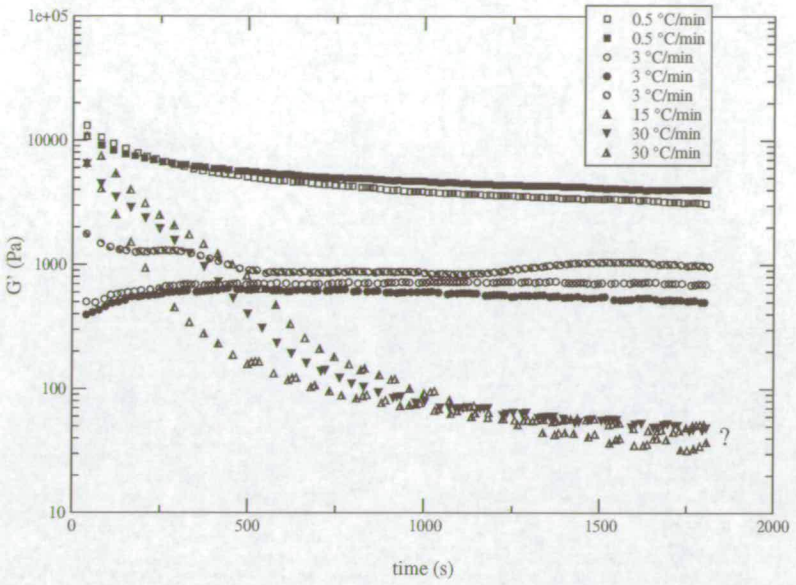

Figure 6.2: The variation of G' with time for samples cooled at rates in the range $0.5-30$°C/min. Samples with $\phi_w = 0.05$ of $R = 370$nm particles were used. Measurements were carried out at 1 Hz with a strain amplitude of 0.5%. At $t = 0$ the sample had been at 20°C for 5 minutes.

In Figure 6.3 the relation of the % strain amplitude to the oscillatory stress applied is shown for samples of various ϕ_w cooled at various rates. Where a linear dependence of the strain to oscillatory stress is observed (see section 3.6.3) then the sample behaves as a linear viscoelastic medium. This is represented by a line with gradient$= 1$ in Figure 6.3 (refer to the solid black line). Such regions are not clearly observed for the samples shown. The smallest possible strain amplitude[2] of 0.5% was used in subsequent measurements [3]. As observed in Figure 6.3, below $\gamma_0 = 0.5\%$ none of the data are far from unit slope and above 0.5% some of the data sets start to deviate significantly. However, caution should be exercised in interpreting all rheology data because of the uncertainty concerning linearity.

The variation of G' with cooling rate deduced from measurements is shown in Figure 6.4. A power law dependence is observed. Similarly, Petrov *et al.* [9] found G' to

[2]The strain amplitude had to be high enough to reduce noise.

[3]This strain is smaller than that used in a previous rheological study of these composites [6].

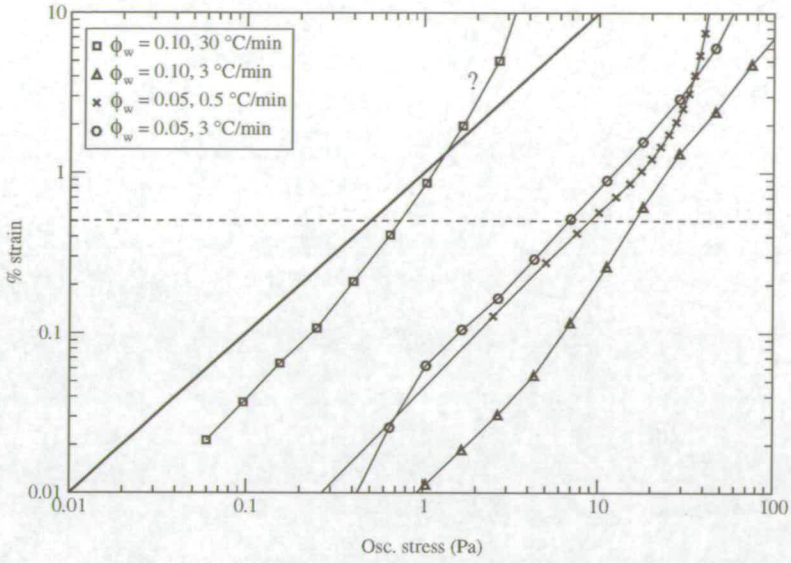

Figure 6.3: The variation of % strain amplitude with oscillatory stress for samples with $\phi_w = 0.05$ and 0.10 of R=370nm particles cooled at various rates. The solid black line is the line $y = x$. The dashed line represents the strain amplitude of 0.5% used in subsequent measurements. The other lines are guides to the eye.

remain around the same order of magnitude for mixtures with smaller $R = 250$nm particles cooled at 0.3°C/min and 0.1°C/min but then found a decrease in G' by an order of magnitude when the cooling rate was increased to 0.8°C/min.

6.2.1 Interpretation

The mechanical strength of these composites seems surprisingly high if one estimates the energy of the effective interaction between the particles. This is the interaction arising when particles clump together in order to minimize the disruption to the nematic order [36, 32, 41]. The interaction energy, U, between 2 particles is $\sim KR$, which for 5CB ($K \sim 10^{-11}$J/m) and $R = 370$nm particles is $\sim 4 \times 10^{-18}$J. From this the energy density and hence the elastic modulus can be estimated;

$$G' = \frac{\phi_w U}{R^3} = \frac{\phi_w K}{R^2}, \tag{6.1}$$

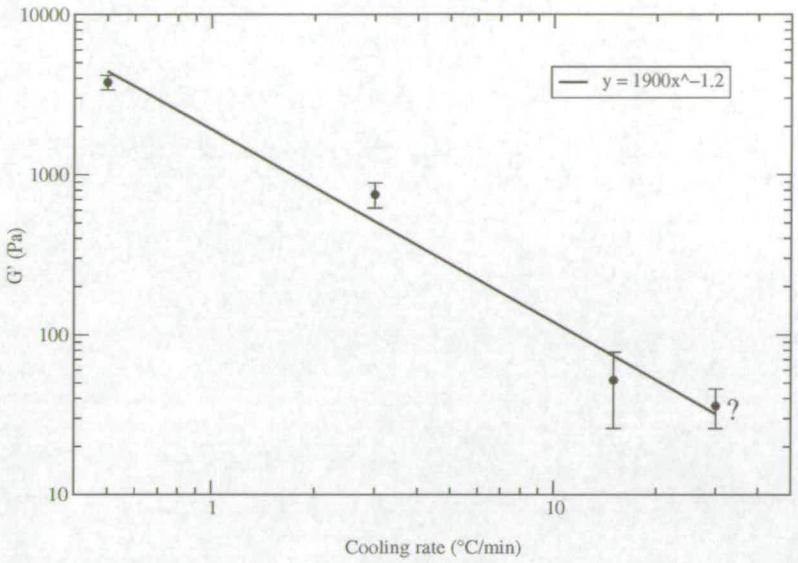

Figure 6.4: The variation of G' with cooling rate. Samples with $\phi_w = 0.05$ of $R = 370$nm particles were used.

which gives $G' \sim 1$ Pa for a sample with $\phi_w = 0.05$ of particles, compared to the $G' \sim 3 \times 10^3$Pa measured for such a sample cooled at 0.5°C/min.

Previously it was proposed that this unusually high storage modulus was due to frustrated nematic order within the edges of particles [6] and subsequently it was reasoned that high effective surface tension at the particle interfaces [8] was responsible (see section 2.4.3). It was determined in the imaging study in Chapter 5 that a cellular foam is formed in these mixtures. In cellular foams the mechanical strength is linked to the structure and the properties of the material in the cell edges and walls [86, 91].

One of the most important structural features in determining the mechanical properties is the relative density of the composite to the solid making up the walls and edges, $\frac{\rho^*}{\rho_s}$, where ρ_s is the density of the densely-packed edges and walls of particles, and ρ^* is the average density of the material as a whole. Equally important is the extent to which the cells are open or closed and the anisotropy of the cells. In the case of these composites $\frac{\rho^*}{\rho_s} \approx \phi_w$. In the imaging study closed cells were observed in all networks examined except for the samples with the lowest particle concentration $\phi_w = 0.025$

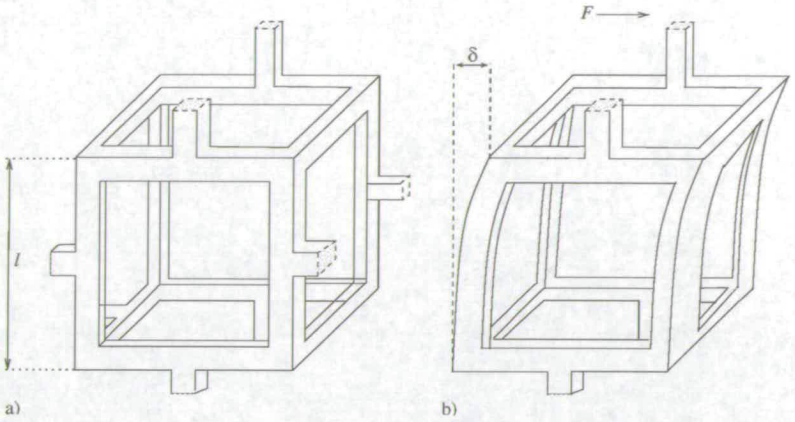

Figure 6.5: a) A cubic cell in an open-cell foam. The mean cell dimension l is defined. b) Cell edge bending when a force, F, is applied resulting in a deflection, δ.

cooled at the fastest rate of 30°C/min. However, differing amounts of perforations in the walls were observed which could affect the role the walls play in determining the mechanical strength of the structure. From detailed measurements of cell dimensions it was determined that there was no one direction of anisotropy in the cell shape (see Table 5.2).

Most closed-cell and open-cell foams have similar stiffnesses; most closed-cell foams behave as if they were open because most of the solid is concentrated in the cell edges and it is the cell edges that generally carry most of the load [94, 95, 96]. For this reason the morphology will be treated as open-cell for the purpose of modelling the mechanical strength, although closed-cell analysis will be discussed in the next section.

When a force is applied to an open-cell foam so as to shear it the cells deform by bending the cell edges, Figure 6.5[4]. From standard beam theory [97] the deflection of the edge, δ, is given by

$$\delta \propto \frac{Fl^3}{E_0 I}, \tag{6.2}$$

where l is the mean cell dimension, F is the force applied, I is the second moment

[4]The analysis uses no asumption of cell shape but cubic cells are used to help visualise the process.

of the area of an edge and E_0 is the Young's modulus of the densely-packed edges of particles. The resulting shear stress $\tau = \frac{F}{l^2}$ and the shear strain $\gamma = \frac{\delta}{l}$ give (see section 3.13),

$$G = \frac{\tau}{\gamma} = \frac{E_0 I}{l^4}. \tag{6.3}$$

Now, the relative density, $\frac{\rho^*}{\rho_s} \propto (\frac{t}{l})^2$ and $I \propto t^4$ so substituting into Equation 6.3 the small-strain shear modulus, G, for an open-cell foam is given by [86, 91, 95]

$$\frac{G}{E_0} = k\left(\frac{\rho}{\rho_0}\right)^2. \tag{6.4}$$

The value of k has been found to be $\approx 3/8$ (see Figure 5.11 in [86][5]) for open-cell foams giving,

$$\frac{G}{E_0} = \frac{3}{8}(\phi_w)^2. \tag{6.5}$$

Equation 6.5 appears to predict that G' should be a function of particle concentration only. In fact, of course, even at constant ϕ_w, a strong dependence on cooling rate was observed (Figure 6.4).

It was observed in the imaging study in Chapter 5 that the cooling rate controls the cell size. Interestingly, there indeed appears to be a strong correlation between cell size and G', Figure 6.6. However, this correlations does not hold across the board. Figure 6.1 shows that G' does not change on increasing the cooling rate from 0.1°C/min to 2°C/min even though the cell size *does* change over this range (Table 5.1). An alternative hypothesis to explain the observed dependence of G' on cooling rate is to appeal to the latter's effect on the structure of the edges. In Chapter 5 (see particularly Figure

[5]When compared to measurements of G' in foams over a wide range of densities.

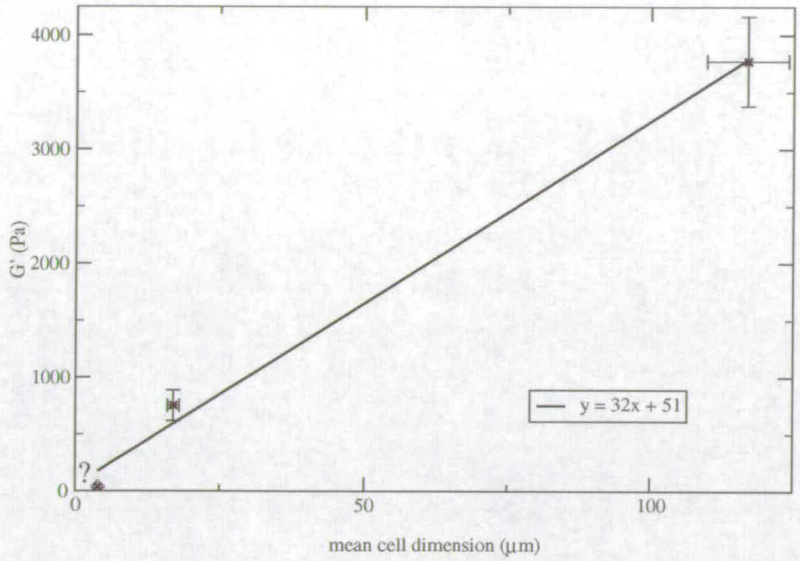

Figure 6.6: The variation of G' with mean cell size as measured from confocal images. Samples with $\phi_w = 0.05, 0.10$ and 0.15 of $R = 370$nm particles were used.

5.11) it was found that the degree of hierarchy, n, of the cellular structure increased with increasing cooling rate, reaching $n = 3$ at the fastest cooling rate of 30°C/min. It is known that for a cellular solid with heirarchical structure, the constant k in Equation 6.4, is changed to k^n, where n is the degree of hierarchy [91]. In the case of these composites, then:

$$\frac{G}{E_0} = \left(\frac{3}{8}\right)^n (\phi_w)^2. \tag{6.6}$$

Thus as $k < 1$ the stiffness will decrease with increasing n, predicting that the storage modulus will decrease with increasing cooling rate.

The degree of hierarchy observed in the structures is shown in Table 6.1 and the predicted values of the storage modulus using this theory are plotted alongside the measured values in Figure 6.7. To obtain an order of magnitude agreement with measured values it is required that $E_0 \approx 3 \times 10^6$ Pa. Although this seems quite high, this is not

CR (°C/min)	k	$\frac{G^*}{E_s}$
0.5	1	0.001
3	2	0.0004
15	3	0.00005
30	3	0.00005

Table 6.1: Degree of hierarchy observed in structures and values for use in open-cell foam theory.

necessarily inconsistent with the particles being at or close to random-close packing (rcp). The equilibrium phase behaviour of hard-spheres has been well characterised [98]; at volume fractions $\phi \sim 0.545$ a phase transition from the liquid state to crystal has been observed. If however the concentration of spheres can be increased quickly enough then a dense metastable state (a colloidal glass) has been observed at $\phi \sim 0.58$ [98, 99] and rcp is observed at $\phi \sim 0.64$. Mason *et al.* [100] found G to diverge as the volume fraction approached 0.56. Recent rheological measurements of colloidal glasses of R=183nm PMMA particles found $G \sim 10^3$ Pa for $\phi = 0.645 = 0.96\phi_{\text{rcp}}$ for this system[6][101]. It is not unrealistic to suggest that the particles can come together quickly enough to form a glass when they become trapped between growing LC domains during the process of network formation. The packing may even be sufficient for the mechanical properties of the stabilizing 'hairs' and bulk PMMA to play a role. E_0 can in principle be as high as G' of bulk PMMA, which is $\sim 10^9$ Pa [86].

The measurements carried out during the cooling process, Figure 6.1, support this analysis as G' shows little variation over the slower cooling rates, consistent with the imaging study which gave $n = 1$ for the same cooling rates.

In summary, G' has been found to be dependent upon cooling rate. Preliminary rheological measurements are not inconsistent with open-cell foam theory in which the heirarchical nature of the particulate edges is responsible for the decrease in mechani-

[6] $\phi_{\text{rcp}} \approx 0.67$ determined by computer simulations for a samples with polydispersity = 12%.

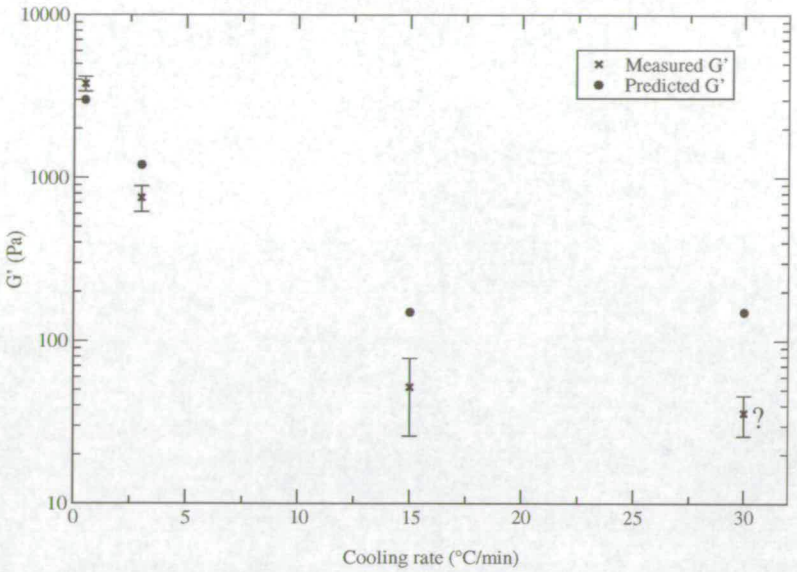

Figure 6.7: G' measured rheologically and G' predicted using open-cell theory. Samples with $\phi_w = 0.05$ of $R = 370$nm particles were used.

cal strength.

In the previous chapter the morphology of the network was seen to vary with particle concentration. Now, this thesis turns to examining the variation of G' with particle concentration.

6.3 Variation with Particle Concentration

For samples with ϕ_w=0.1 and 0.15 measurements were carried out at cooling rates of 0.5°C/min, 3°C/min and 30°C/min. The same trend with cooling rate is observed for samples with $\phi_w = 0.1$ and 0.15 of R=370nm particles as was observed for samples with $\phi_w = 0.05$ of particles, Figure 6.8. However, the same increase in degree of hierarchy with increase in cooling rate was not observed in the mixtures with higher concentrations of particles ($\phi_w = 0.10$ and 0.15), Table 6.2. Therefore the same variation of G' with cooling rate was not expected for these samples, however, this could

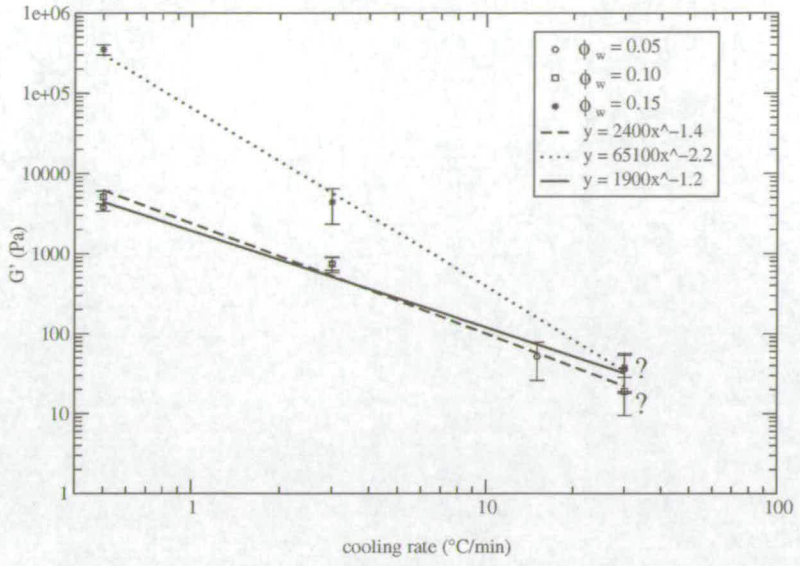

Figure 6.8: The variation of G' with cooling rate. Samples with $\phi_w = 0.05, 0.10$ and 0.15 of $R = 370$nm particles were used. Measurements were carried out at 1 Hz with a strain amplitude of 0.5%.

be because the hierarchy was present but not resolvable in the microscopy images. In fact, the density of particles at the nodes was observed to be lower in the samples with $\phi_w = 0.15$ of particles cooled at 30°C/min (see Appendix A) and this could be interpreted as hierarchy on a smaller scale.

In the case of the slower cooling rates (0.5°C/min and 3°C/min) there is an increase in G' with ϕ_w, Figure 6.9. Between $\phi_w = 0.10$ and $\phi_w = 0.15$ there is a large increase in G'. For a cooling rate of 0.5°C/min G' increases from $\sim$ 5100 Pa for $\phi_w = 0.1$ to $\sim$ 351300 Pa for $\phi_w = 0.15$; this is $\sim \times 70$. There is a similar increase when cooling at 3°C/min where G' increases from $\sim$ 700 Pa for $\phi_w = 0.1$ to $\sim$ 4400 Pa for $\phi_w = 0.15$; only $\sim \times 6$ this time. This differs from the G nearly $\propto \phi_w$ relationship found in mixtures of small PMMA particles ($R = 150$nm) and 5CB in previous work [8], where, however, the cooling rate was not *controlled*.

In Chapter 5 with an increase in ϕ_w a decrease in the amount of perforations in the walls was observed. It is therefore possible that the cell walls play a greater role in

ϕ_w	Cooling rate (°C/min)	small cells (μm)	n
0.10	0.5	none	1
0.10	3	none	1
0.10	30	2.4	2
0.15	0.5	none	1
0.15	3	none	1
0.15	30	none	1

Table 6.2: Summary of information on networks formed at various rates and with $\phi_w = 0.10 - 0.15$, gathered from microscopy images.

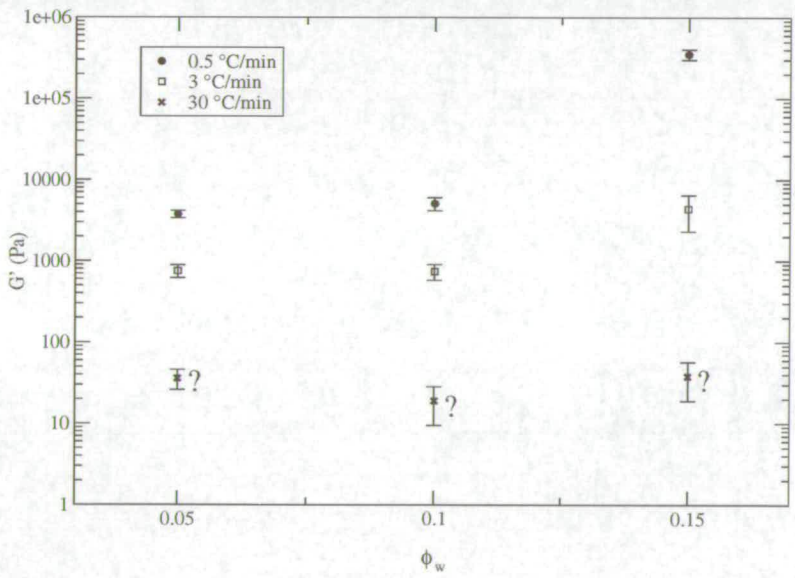

Figure 6.9: The variation of G' with weight fraction of particles, ϕ_w, for samples with $R = 370$nm particles cooled at various rates.

determining the mechanical strength for larger ϕ_w. If the contribution of the cell walls is taken into account and the structure is now treated as closed-cell [86] then G' is given by

$$\frac{G}{E_0} = \frac{3}{8}\left(\phi_e^2(\phi_w)^2 + (1-\phi_e)\phi_w\right), \tag{6.7}$$

where ϕ_e is the fraction of particles contained in the cell edges (see Table 5.5). The first term is the contribution from the cell edges bending which was present in the open-cell foam analysis. The second term arises from the stretching of the cell walls when the edges bend. In Figure 6.10 the variation of G' with ϕ_w for samples cooled at 0.5°C/min is shown alongside the predicted values from open and closed cellular theory[7]. Although it is possible that less perforations in the cell walls are responsible for this large increase in G' between $\phi_w = 0.10$ and 0.15 perforations were still observed for $\phi_w = 0.15$ which raises questions as to whether or not these stresses in the walls would actually occur.

6.4 Frequency Dependence

The frequency dependence of G' and G'' for samples of different ϕ_w cooled at various rates is shown in Figure 6.11. At lower frequencies G'' is dominant. Both moduli increase with frequency; G' increases by $\sim$ a factor of 100 over the 5 decades and $G'' \sim 10$. For each sample the greatest difference in magnitudes of G' and G'' is observed at the highest frequency of 40Hz. As the frequency increases G' becomes larger than G'' and continues to dominate for the remaining frequencies. This behaviour is characteristic of viscous behaviour at long times (when $\frac{G''}{G'} < 1$) and elastic behaviour (when $\frac{G''}{G'} > 1$) at short times (see sections 3.6.1 and 3.6.3). The frequency at which

[7]The fraction of particles in the edges was extrapolated from imaging data.

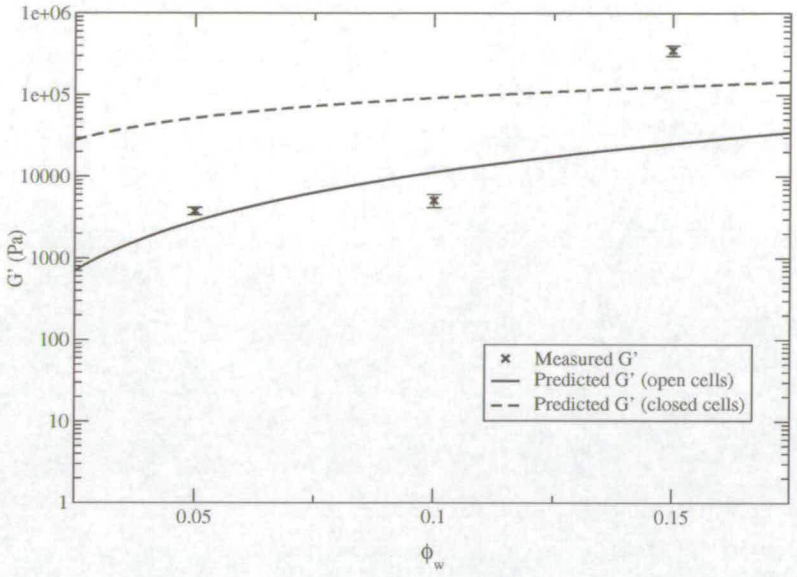

Figure 6.10: The variation of G' with ϕ_w for samples cooled at 0.5°C/min. The predicted variation of G' with ϕ_w from open and closed cellular theory are shown.

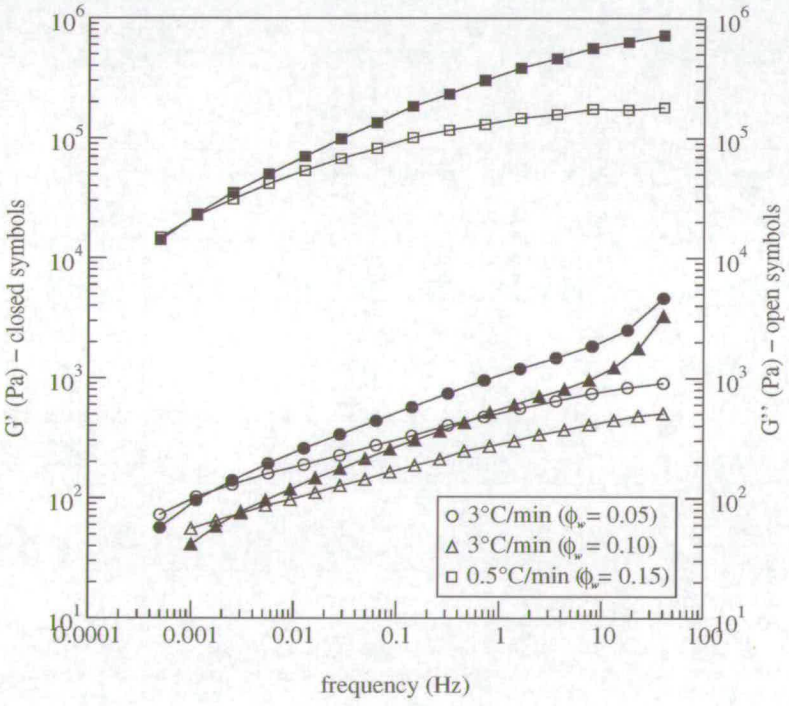

Figure 6.11: The variation of G'(closed symbols) and G''(open symbols) with frequency. Samples with $\phi_w = 0.05 - 0.15$ of $R = 370$nm particles cooled at various rates.

the material makes the transition from viscous to elastic, f_c, appears to decrease with decreasing G' (from ~ 0.008 Hz at $G' \sim 18600$Pa to ~ 0.002Hz at $G' \sim 70$Pa).

6.5 Summary

The variation of the mechanical properties of the network formed in mixtures of PMMA and nematic LC with cooling rate and particle concentration have been investigated using rheological techniques. Preliminary results shows that a decrease in G' with cooling rate is observed for all ϕ_w investigated. These values are not inconsistent with those predicted by open-cell foam theory in which the increasing degree of hierarchy present in the networks is responsible for the decrease in mechanical strength. The same trend with cooling rate is observed for all particle concentrations examined. With an increase in ϕ_w an increase in G' is observed, possibly due to the cell walls beginning to contribute to the mechanical properties as ϕ_w increases. A more detailed rheological study is needed in order to test the hypotheses discussed further.

Chapter 7

Conclusions and Future Work

Mixtures of thermotropic liquid crystal (5CB) and colloid (polymethylmethacrylate) particles were studied using a variety of experimental techniques.

When these mixtures are cooled through the isotropic-nematic (IN) phase transition a three-dimensional network structure of particles is formed. Time-resolved LSCM was used to achieve near-single-particle resolution and observe the kinetics of the network formation upon cooling from the initial isotropic dispersion. As the mixture was cooled below the IN transition, nematic domains began to grow, expelling particles which were transported and concentrated into boundary regions to form the network. The rate of nematic domain growth in these mixtures was found to be much slower than that in pure 5CB. Calorimetric and microscopy data suggest that this slowing is due to the presence of hexane impurities, retained from the drying process, opening up a biphasic region in the phase diagram. Rheology measurements as a function of temperature were used to examine the changes in the viscoelastic properties of the composite as the network is formed. These showed that after network formation the composite became much stronger than pure LC. Most importantly, above T_{IN} $G'' > G'$ and the mixture was a liquid and below T_{IN} $G' > G''$ and the mixture was a solid - as observed macroscopically. Microscopy observations were used to examine the re-

versiblity of this process of network formation. It was shown that upon heating above T_{IN} single particles became free and exhibited Brownian motion. As the sample was heated deep into the isotropic phase the network was broken up but clusters of particles remained. Sedimentation of these clusters caused a density gradient of particles to form across the sample with varying height. Upon cooling a new network of particles or 'clusters of particles' was formed.

LSCM was used to examine the morphology of the network that was formed when mixtures of PMMA and 5CB were cooled through the IN transition. From these images and three-dimensional reconstructions the structure was observed to be that of a cellular foam. The study showed that the morphology of this network was cooling-rate and particle concentration dependent. A decrease in cell size with increase in cooling rate was found. At high cooling rates, a hierarchical cellular structure was formed with small cells appearing within the walls and nodes of big cells. Except for the slowest cooling rate studied, the mean cell diameter was found to be inversely proportional to the particle concentration. With an increase in the amount of particles present the amount of perforations in the cell walls decreased. As ϕ_w increased the cells became more spherical in shape with the fraction of particles in the cell edges increasing.

The variation of the mechanical properties of the network formed in mixtures of PMMA and nematic LC with cooling rate and particle concentration were investigated using rheological techniques. Preliminary results show that a decrease in G' with cooling rate is observed for all ϕ_w investigated. These values are not inconsistent with those predicted by open-cell foam theory in which the increasing degree of hierarchy present in the networks is responsible for the decrease in mechanical strength. The same trend with cooling rate is observed for all particle concentrations examined. With an increase in ϕ_w an increase in G' is observed, possibly due to the cell walls beginning to contribute to the mechanical properties as ϕ_w increases.

7.1 Future Work

Future studies to continue the work presented in this thesis would include further investigation of the role of impurities in the system. DSC measurements in this thesis (for mixtures with $R = 390$nm particles) showed a linear decrease in T_{IN} with particle concentration. An identical study of mixtures with particles of different sizes would determine whether or not the hexane content scales appropriately with particle size. This would be another angle from which to test the hypothesis that alkane molecules are trapped in the PHSA 'hairs' from the drying process [1].

When mixtures with particles that had been dried intensively were examined an almost identical DSC trace to that of pure 5CB was observed; it would be interesting to observe such mixtures using time-resolve LSCM as they pass through the IN transition. Theory [40] suggests that the maximum speed that the IN interface can move at and still sweep along particles is given by

$$v_{crit} \sim \frac{W}{\sqrt{K\rho}}, \tag{7.1}$$

and for this system $v_{IN}^{pure} \gtrsim v_{crit}$. It is therefore questionable whether or not network formation would still occur for particles of this size ($R > 100$nm) if all impurities were removed in the drying process. If a network did form how would the morphology differ from that formed in mixtures of particles that were dried less rigorously?

If the alkane content varies with particle size and therefore the interface speed then it would be interesting to examine how the morphology and mechanical properties of the network also vary with particle size. This work is currently being carried out in the group at the University of Edinburgh by Dr. Paul Clegg, see Figure 7.1.

[1] It would be essential to ensure that a standard procedure for particle washing and drying prior to dispersion in the liquid crystal was used.

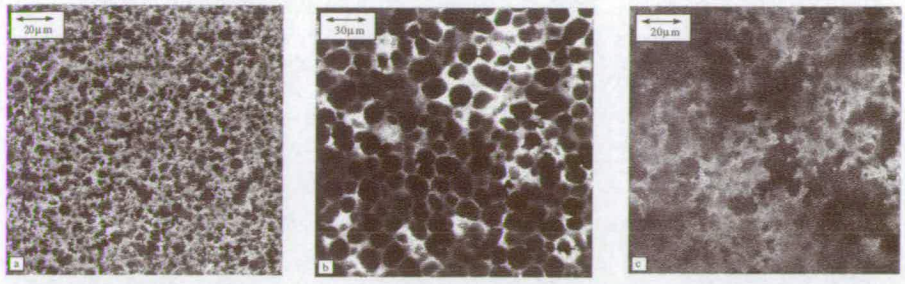

Figure 7.1: LSCM micrographs of the network formed in mixtures with $\phi_w = 0.15$ of particles cooled at 4°C/min. a) $R = 200$nm, b) $R = 390$nm and c) $R = 700$nm. The images shown in a) and c) are courtesy of Paul Clegg.

Although the network structure that is formed in these mixtures has been studied in detail in this thesis the aging effects have not. Microscopy studies carried out at times significantly later than the completion of the network formation would enable the effects of ageing and network stability to be examined. Knowledge about aging is, of course, essential if the colloid-liquid crystal composites studied in this thesis are to find application as display materials.

This thesis has demonstrated that mixtures of 5CB and PMMA are a model arrested system which will reward further study.

Appendix A

Further Characterisation of Network Morphology

In this appendix the networks formed in samples with $\phi_w = 0.025 - 0.15$ of $R = 390$nm particles are characterised in further detail.

$\underline{\phi_w = 0.025}$

It was not possible to measure the size of the large cells in these samples for the slower cooling rates because they were becoming comparable to the size of the sample cell, however it was possible to observe the particle arrangements within the walls and nodes. For a cooling rate of 3°C/min smaller cells of diameter $\sim 6.7\mu$m are observed in the nodes, Figure A.1(a). For a cooling rate of 30°C/min struts are observed at the top of the sample and then walls appear with depth, Figures A.1 (b)and (c). Small cells of $\sim 1 - 2\mu$m and $\sim 5\mu$m are observed within the struts and nodes, indicating that there are 2 degrees of hierarchy. In Figure A.2 the distribution in size of the cells observed in the network of samples cooled at 30°C/min is shown. Taking these smaller cells into account the mean cell size in these networks is $\sim 4.1\mu$m.

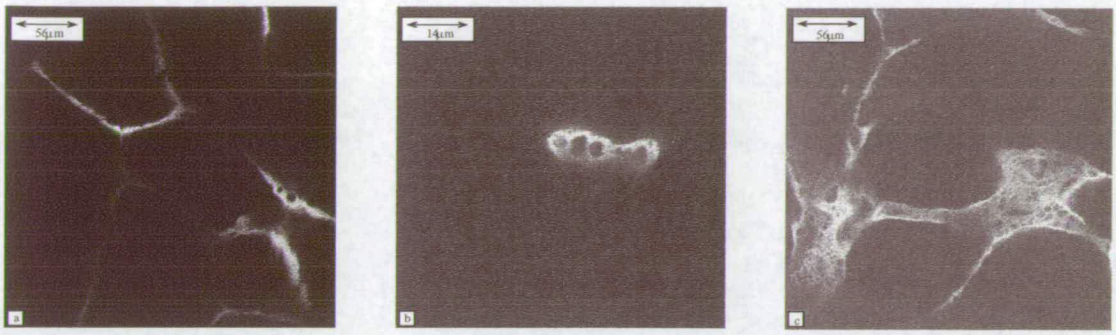

Figure A.1: The networks formed in samples with $\phi_w = 0.025$ of R=390nm particles cooled at various rates observed at various depths below the coverslip. (a) 3°C/min (50μm), (b) 30°C/min (30μm), and (c) 30°C/min (100μm).

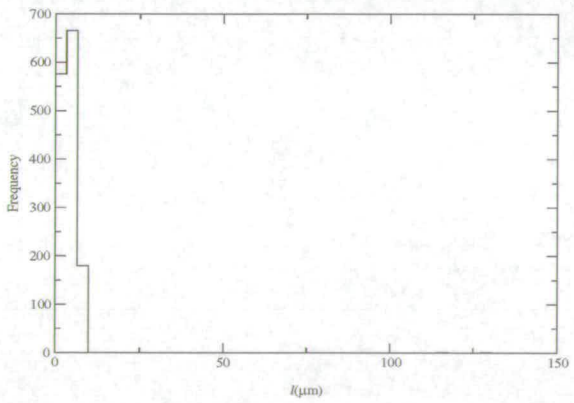

Figure A.2: Distribution of cell sizes in the network formed in a sample with $\phi_w = 0.025$ of $R = 390$nm particles when cooled at 30°C/min.

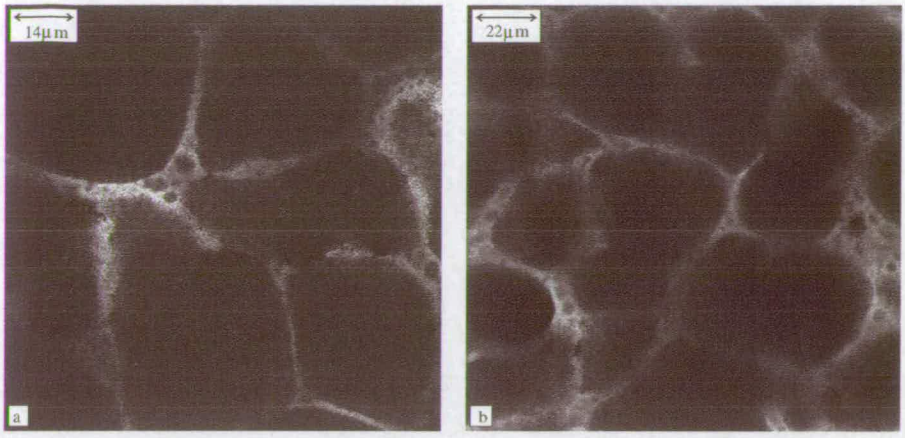

Figure A.3: The nodes where walls of particles meet in the networks formed in samples with $\phi_w = 0.07$ of R=390nm particles cooled at 30°C/min. (a) 30μm and (b) 50μm below the coverslip.

$\underline{\phi_w = 0.07}$

For samples cooled at a rate of 0.5°C/min solid walls of particles and nodes are observed to be of thickness $\sim 3.2\mu$m and $\sim 4.7\mu$m respectively. For 3°C/min, Figure A.3(a), cells of diameter $\sim 9.6\mu$m are observed within the walls and the nodes. For a cooling rate of 30°C/min cells of $\sim 0.5\mu$m and of $\sim 4\mu$m are observed indicating that there are 2 levels of hierarchy present. The distribution of cell sizes in the networks formed at cooling rates of 3°C/min and 30°C/min are shown Figure A.4. In both cases 2 peaks are observed in the distribution indicating at least 1 degree of hierarchy and there are considerably more small cells in relation to large cells in the sample cooled at the fastest rate. As with the $\phi_w = 0.05$ mixtures it is not possible to distinguish between scales for the small cell sizes. The mean cell diameter including these smaller cells is $\sim 39\mu$m for a cooling rate of 3°C/min and $\sim 8\mu$m for a cooling rate of 30°C/min.

** $\underline{\phi_w = 0.10}$

For samples cooled at a rate of 0.5°C/min solid walls of particles and nodes are observed to be of thickness $\sim 4.1\mu$m and $\sim 6.3\mu$m respectively. When the cooling rate is increased to 3°C/min, Figure A.5(a), no hierarchy is observed. For a cooling rate

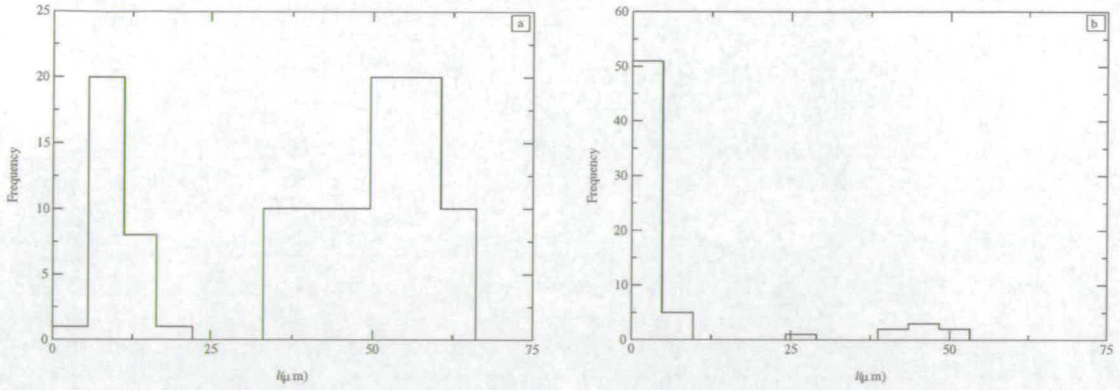

Figure A.4: The distribution of cell sizes in the network formed in a sample with $\phi_w = 0.07$ of $R = 390nm$ particles when cooled at (a) 3°C/min and (b) 30°C/min.

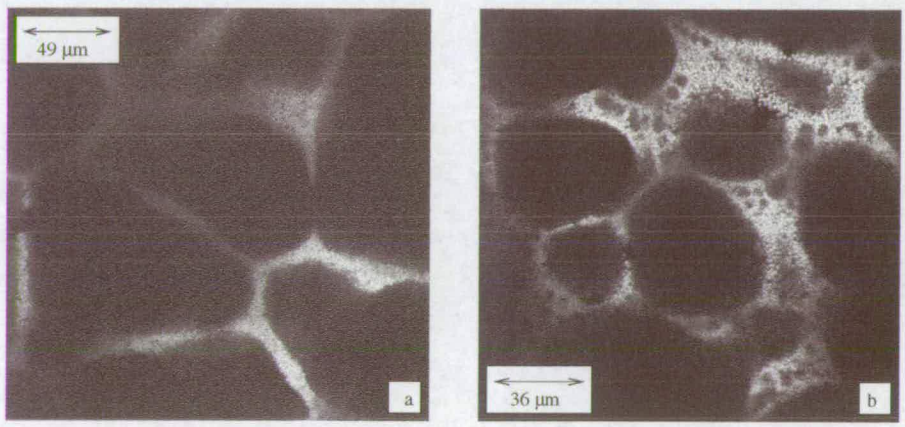

Figure A.5: The nodes where walls of particles meet in the networks formed in samples with $\phi_w = 0.10$ of R=390nm particles cooled at (a) 3°C/min and (b) 30°C /min.

of 30°C/min small cells within the nodes are observed, Figure A.5(b), of diameter $\sim 2.4\mu$m. Image quality was not sufficient to allow a distribution of cell size to be found.

$\underline{\phi_w = 0.15}$

For samples cooled at a rate of 0.5°C/min solid walls of particles and nodes are observed to be of thickness $\sim 4.7\mu$m and $\sim 7.6\mu$m respectively. For a faster cooling rate of 3°C/min no smaller cells are observed, Figure A.6(a). When cooled at the fastest rate of 30°C/min, Figure A.6(b), again no hierarchy is observed, however, the particles

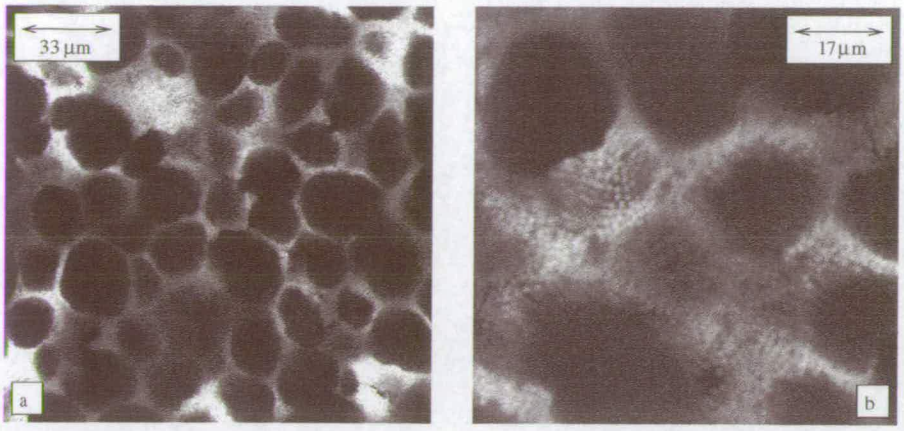

Figure A.6: The nodes where walls of particles meet in the networks formed in samples with $\phi_w = 0.15$ of R=390nm particles cooled at (a) 3°C/min and (b) 30°C /min.

at the nodes do not appear to be so well packed and spaces of $\sim 1 - 2\mu$m are observed. Here the small LC domains would be approaching the particle size.

Appendix B

Published Papers

- J Cleaver, D Vollmer, J Crain and WCK Poon. Self-supporting liquid crystal composite. *Mol. Cryst. Liq. Cryst.*, 409:59-68, 2002.
- J Cleaver and WCK Poon. Network formation in colloid-liquid crystal mixtures studied by confocal microscopy. *J. Phys.: Condens. Mat.*, 16:S1901-S1909, 2004.
- D Vollmer, G Hinze, WCK Poon, J Cleaver and ME Cates. The origin of network formation in colloid-liquid crystal composites. *J. Phys.: Condens. Mat.*, 16:L227-L233, 2004.

List of Figures

List of Tables

Bibliography

[1] PJ Collings and M Hird. *Introduction to Liquid Crystals*. Taylor and Francis, 1997.

[2] MD Haw. Colloidal suspensions, brownian motion, molecular reality: a short history. *J. Phys.: Condens. Mat.*, 14:7769–7779, 2002.

[3] WCK Poon. The physics of a model colloid-polymer mixture. *J. Phys.: Condens. Mat.*, 14(33):R859–R880, 2002.

[4] H Stark. Physics of colloidal dispersions in nematic liquid crystals. *Phys. Rep.*, 351(6):387–474, 2001.

[5] P Poulin, VA Raghunathan, P Richetti, and D Roux. On the dispersion of latex particles in a nematic solution. 1. Experimental evidence and a simple model. *J. Phys. II France*, 4:1557–1569, 1994.

[6] SP Meeker, WCK Poon, J Crain, and EM Terentjev. Colloid liquid crystal composites: an unusual soft solid. *Phys. Rev. E*, 61(6):6083–6085, 2000.

[7] VJ Anderson, EM Terentjev, SP Meeker, J Crain, and WCK Poon. Cellular solid behaviour of liquid crystal colloids 1. Phase separation and morphology. *Euro. Phys. J. E*, 4:11–20, 2001.

[8] VJ Anderson and EM Terentjev. Cellular solid behaviour of liquid crystal colloids 2. Mechanical properties. *Euro. Phys. J. E*, 4:21–28, 2001.

[9] PG Petrov and EM Terentjev. Formation of cellular solid in liquid crystal solids. *Langmuir*, 17:2942–2949, 2001.

[10] E Kaneko. *Liquid Crystal TV Displays: Principles and Applications of Liquid Crystal Displays*. KTK Scientific Publishers, 1987.

[11] LA Goodman. *Introduction to Liquid Crystals*. Plenum Press, 1975.

[12] M Schadt and W Helfrich. Voltage-dependent optical activity of a twisted nematic liquid crystal. *Appl. Phys. Lett.*, 18(4):127–128, 1971.

[13] J van Haaren. Out of the groove. *Nature*, 392:331–333, 1998.

[14] RAM Hikmet. Electrically induced light scattering from anisotropic gels. *J. Appl. Phys.*, 68:4406–4412, 1990.

[15] JW Doane, NA Vaz, BG Wu, and S Zumer. Field controlled light scattering from nematic microdroplets. *Appl. Phys. Lett.*, 48(4):269–271, 1986.

[16] M Kreuzer, T Tschudi, WH de Jeu, and R Eidenschink. New liquid crystal display with bistability and selective erasure using scattering in filled nematics. *Appl. Phys. Lett.*, 62(15):1712–1714, 1993.

[17] M Kreuser and R Eidenschink. Filled nematics. In GP Crawford and S Zumer, editors, *Liquid Crystals in Complex Geometries*, pages 307–324. Taylor and Francis Ltd, 1996.

[18] CD Sheraw, MG Kane, J Francl, and *et al.*. Flexible liquid crystal displays driven by organic thin film transistors on polymeric substrates. In *Device Research Conference*, pages 181–182, 2001.

[19] H Fujikake, T Murashige, and H Sato. Fundamental display properties of flexible devices containing polymer-stabilized ferroelectric liquid crystal between plastic substrates. *Opt. Eng.*, 41(9):2195–2201, 2002.

[20] M van Boxtel, M Wubbenhorst, J van Turnhout, C Bastiaansen, and D Broer. A dielectric study on the relaxation and switching behaviour of liquid crystals confined within a colloidal network. *Liq. Cryst.*, 30(2):235–249, 2003.

[21] H Nakamura, SP Meeker, Y Taira, WCK Poon, and J Crain. Optical properties of colloid liquid crystal composites. *Mol. Crys. Liq. Crys.*, 368:3935–3942, 2001.

[22] M van Boxtel, R Janssen, C Bastiaansen, and D Broer. Viscoelastic liquid crystal colloids for the continuous processing of twisted nematic electro-optical cells. *J. Appl. Phys.*, 89(2):838–842, 2001.

[23] M van Boxtel, R Janssen, D Broer, H Wilderbeek, and C Bastiaansen. Polymer-filled nematics:a new class of light-scattering materials for electro-optical switches. *Adv. Mater.*, 12(10):753–757, 2000.

[24] GP Crawford and S Žumer, editors. *Liquid Crystals in Complex Geometries*. Taylor and Francis, 1996.

[25] DH Everett. *Basic Principles of Colloid Science*. The Royal Society of Chemistry, 1988.

[26] PN Pusey. Colloidal suspensions. In JP Hansen and D Levesque, editors, *Liquids, Freezing and Glass Transition*, pages 763–942, 1991.

[27] PN Pusey and W van Megan. Phase behaviour of concentrated suspensions of nearly hard colloidal spheres. *Nature*, 320:340–342, 1986.

[28] HNW Lekkerkerker, JKG Dhont, H Verduin, C Smits, and JS van Duijneveldt. Interactions, phase transitions and metastable states in concentrated colloidal dispersions. *Physica A*, 213:18–29, 1995.

[29] D Frenkel. Introduction to colloidal systems. In ME Cates and MR Evans, editors, *Soft and Fragile Matter: Nonequlibrium Dynamics, Metastability and Flow*, pages 113–143, 1999.

[30] PG de Gennes and J Prost. *The Physics of Liquid Crystals*. Oxford University Press, 1993.

[31] PM Chaikin and TC Lubensky. *Principles of Condensed Matter*. Cambridge University Press, 1995.

[32] RW Ruhwandl and EM Terentjev. Long range forces and aggregation of colloidal particles in a nematic liquid crystal. *Phys. Rev. E*, 55(3):2958–2961, 1997.

[33] EM Terentjev. Disclination loops, standing alone and around solid particles in nematic liquid crystals. *Phys. Rev. E*, 51(2):1330–1337, 1995.

[34] OV Kuksenok, RW Ruhwandl, SV Shiyanovski, and EM Terentjev. Director structure around a colloid particle suspended in a nematic liquid crystal. *Phys. Rev. E*, 54(5):5198–5203, 1996.

[35] RW Ruhwandl and EM Terentjev. Monte carlo simulation of topological defects in the nematic liquid crystal matrix around a spherical colloid particle. *Phys. Rev. E*, 56(5):5561–5565, 1997.

[36] S Ramaswamy, R Nityananda, V Raghunathan, and J Prost. Power-law forces between particles in a nematic. *Mol. Cryst. Liq. Cryst*, 288:175–180, 1996.

[37] P Poulin, H Stark, TC Lubensky, and DA Weitz. Novel colloidal interactions in anisotropic fluids. *Science*, 275:1770–1773, 1997.

[38] P Poulin and DA Weitz. Inverted and multiple nematic emulsions. *Phys. Rev. E*, 57(1):626–637, 1998.

[39] P Poulin, V Cabuil, and DA Weitz. Direct measurement of colloidal forces in an anisotropic solvent. *Phys. Rev. Lett.*, 79(24):4862–4865, 1997.

[40] JL West, A Glushchenko, G Liao, Y Reznikov, D Andrienko, and MP Allen. Drag on particles in a nematic suspension by a moving nematic-isotropic interface. *Phys. Rev. E*, 66:012702, 2002.

[41] TC Lubensky, D Pettey, N Currier, and H Stark. Topological defects and interactions in nematic emulsions. *Phys. Rev. E*, 57(1):610–625, 1998.

[42] T Bellini, M Caggioni, NA Clark, F Mantegazza, A Maritan, and A Pellizzola. Fluctuation mediated interaction and phase separation of nanoparticles in a liquid crystal solvent. *Phys. Rev. Lett.*, 91(8):085704, 2003.

[43] VA Raghunathan, P Richetti, and D Roux. Dispersion of latex particles in a nematic solution. 2. Phase diagram and elastic properties. *Langmuir*, 12:3789–3792, 1996.

[44] J Yamamoto and H Tanaka. Transparent nematic phase in a liquid crystal based microemulsion. *Nature*, 409:321–325, 2001.

[45] C Pizzey, S Klein, E Leach, JS van Duijneveldt, and RM Richardson. Suspensions of colloidal plates in a nematic liquid crystal: a small angle x-ray scattering study. *J. Phys.: Condens. Mat.*, 16:2479–2495, 2004.

[46] J-C Loudet, P Barois, and P Poulin. Colloidal ordering from phase separation in a liquid crystalline continuous phase. *Nature*, 407:611–613, 2000.

[47] J-C Loudet, P Poulin, and P Barois. Edge dislocations of colloidal chains suspended in a nematic liquid crystal. *Europhys. Lett.*, 54(2):175–181, 2001.

[48] M Zapotocky, L Ramos, P Poulin, TC Lubensky, and DA Weitz. Particle-stabilized defect gel in cholesteric liquid crystals. *Science*, 283:209–212, 1999.

[49] A Jakli, G Kali, and L Rosta. Silica particle aggregates in LC-matrix. *Physica B*, 234-236:297–299, 1997.

[50] V Sequeira and D Hill. Particle suspensions in liquid crystalline media: rheology, structure and dynamic interactions. *J. Rheol.*, 42(1):203–213, 1998.

[51] GA Oweimreen and DE Martire. The effect of quasispherical and chainlike solutes on the nematic to isotropic phase transition in liquid crystals. *J. Chem. Phys.*, 72(4):2500–2510, 1980.

[52] L Antl, JW Goodwin, RD Hill, RH Ottewill, SM Owens, S Papworth, and JA Waters. The preparation of poly(methylmethacrylate) latices in non-aqueous media. *Coll. Surf.*, 17:67–78, 1986.

[53] RS Jardine and P Bartlett. Synthesis of non-aqueous fluorescent hard-sphere polymer colloids. *Colloid. Surface. A*, 211(2-3):127–132, 2002.

[54] AI Campbell and P Bartlett. Fluorescent hard-sphere polymer colloids for confocal microscopy. *J. Colloid. Interf. Sci.*, 256(2):325–330, 2002.

[55] DJ Cebula, JW Goodwin, RH Ottewill, G Jenkin, and J Tabony. Small angle and quasi-elastic neutron scattering studies on polymethylmethacrylate latices in nonpolar media. *Colloid Polym. Sci.*, 261:555–564, 1983.

[56] Merck. 5CB certificate of analysis.

[57] MS Elliot. *The Optical Microscopy of Colloidal Suspensions*. PhD thesis, University of Edinburgh, 1999.

[58] S Bradbury and B Bracegirdle. *Introduction to Light Microscopy*. BIOS Scientific Publishers, 1998.

[59] W Hossack. Modern optics. University of Edinburgh Undergraduate Course.

[60] RH Webb. Confocal optical microscopy. *Rep. Prog. Phys.*, 59:427–471, 1996.

[61] JB Pawley, editor. *Handbook of Biological and Confocal Microscopy*. Plenum Press, 1995.

[62] CJR Sheppard and DM Shotton. *Confocal Laser Scanning Microscopy*. BIOS Scientific Publishers, 1997.

[63] B Herman. *Fluorescence Microscopy*. BIOS Scientific Publishers, 1998.

[64] Bio-Rad. *Radiance2000 MP Operating Manual*, 1999.

[65] ME Brown. *Introduction to Thermal Analysis : Techniques and Applications*. Chapman and Hall, 1988.

[66] A Blažek. *Thermal Analysis*. Van Nostrand Reinhold Co. Ltd, 1973.

[67] WWM Wendlandt. *Thermal Methods of Analysis*. John Wiley and Sons, 2nd edition, 1974.

[68] HA Barnes, JF Hutton, and K Walters. *An Introduction to Rheology*. Elsevier Science Publishers, 1993.

[69] TA Instruments. *Oscillation for CSL Software Manual*, 1995.

[70] M Reiner. *Deformation, Strain and Flow : An Elementary Introduction to Rheology*. HK Lewis and Co. Ltd., 2nd edition, 1960.

[71] GV Vinogradov and AY Malkin. *Rheology of Polymers*. Mir Publishers, 1977.

[72] RG Larson. *The Structure and Rheology of Complex Fluids*. Oxford University Press, 1999.

[73] WG Gall and NG McCrum. Internal friction in stereoregular polymethyl methacrylate. *J. Polym. Sci.*, L:489–495, 1961.

[74] V Popa-Nita and TJ Sluckin. Kinetics of the nematic-isotropic interface. *J. Phys. II France*, 6:873–884, 1996.

[75] B Kronberg, DFR Gilson, and D Patterson. Effect of solute size and shape on orientational order in liquid crystal systems. *J. Chem. Soc. Faraday II*, 72:1673–1686, 1976.

[76] H Orendi and M Ballauff. Analysis of the phase diagrams of mixtures of a nematic liquid with n-alkanes. *Ber. Bunsen. Phys. Chem.*, 96(1):96–100, 1992.

[77] DE Martire, GA Oweimreen, GI Agren, SG Ryan, and HT Peterson. The effect of quasispherical solutes on the nematic to isotropic transition in liquid crystals. *J. Chem. Phys.*, 64(4):1456–1463, 1976.

[78] DE Martire. Thermodynamics of phase transitions. In GR Luckhurst and GW Gray, editors, *Molecular Physics of Liquid Crystals*, pages 221–238. Academic Publishers, 1979.

[79] D Vollmer, G Hinze, WCK Poon, J Cleaver, and ME Cates. The origin of network formation in colloid-liquid crystal composites. *J. Phys. : Condens. Mat.*, 16:L227–L233, 2004.

[80] DR Lide, editor. *Handbook of Chemistry and Physics*. CRC Press, 82nd edition, 2001.

[81] The density of PMMA is 1.18g/cm^3 [73]. The density of hexane at 25 ℃ is 0.6548g/cm^3 [80]. The molecular volume of hexane is 2.20×10^{-22} cm^3.

[82] H Kneppe, F Schneider, and NK Sharma. A comparative study of the viscosity of some nematic liquid crystals. *Ber. Bunsen. Phys. Chem.*, 85:784–789, 1981.

[83] Rheological measurements.

[84] Merck. 5CB safety data sheet.

[85] M Tintaru, R Moldovan, T Beica, and S Frunza. Surface tension of some liquid crystals in the cyanobiphenyl series. *Liq. Crys.*, 28(5):793–797, 2001.

[86] LJ Gibson and MF Ashby. *Cellular Solids*. Cambridge University Press, 2nd edition, 1997.

[87] J Banhart. Metallic foams. *Europhys. News*, 31(1), 1999.

[88] FA Shutov. Foamed polymers, cellular structures and properties. *Adv. Polym. Sci.*, 51:155–218, 1983.

[89] F Baumgärtner, I Duarte, and J Banhart. Industrialization of powder compact foaming process. *Adv. Eng. Mater.*, 2(4):168–174, 2000.

[90] R Aveyard, BP Binks, and JH Clint. Emulsions stabilised solely by colloidal particles. *Adv. Coll. Int. Sci.*, 100-102:503–546, 2003.

[91] R Lakes. Materials with structural hierarchy. *Nature*, 361:511–515, 1993.

[92] L Carpaneto, A Ristagno, P Stagnaro, and B Valenti. Polymer/liquid crystal composites: phase separation and morphology of blends of PBMA or PMMA and E7. *Mol. Cryst. Liq. Cryst.*, 290:213–226, 1996.

[93] D Weaire and S Hutzler. *The Physics of Foams*. Clarendon Press, 1999.

[94] G Menges and F Knipschild. Estimation of mechanical properties for rigid polyurethane foams. *Polym. Eng. Sci.*, 15:623–627, 1975.

[95] LJ Gibson and MF Ashby. The mechanics of three-dimensional cellular materials. *P. Roy. Soc. Lond. A*, 382:43–59, 1982.

[96] MF Ashby. The mechanical properties of cellular solids. *Metall. Trans. A*, 14A:1755–1769, 1983.

[97] SP Timoshenko and JN Goodier. *Theory of Elasticity*. McGraw-Hill, 3rd edition, 1970.

[98] WCK Poon and PN Pusey. Phase transition of spherical colloids. In M Baus, LF Rull, and J-P Ryckaert, editors, *Observation, Prediction and Simulation of Phase Transitions in Complex Fluids Conference*, pages 3–51. Kluwer Academic Publishers, 1995.

[99] PN Pusey and W van Megen. Observation of a glass transition in suspensions of spherical colloids. *Phys. Rev. Lett.*, 59(18):2083–2086, 1987.

[100] TG Mason and DA Weitz. Linear viscoelasticity of colloidal hard sphere suspensions near the glass transition. *Phys. Rev. Lett.*, 75(14):2770–2773, 1995.

[101] G Petekidis, D Vlassopoulos, and PN Pusey. Yielding and flow of colloidal glasses. *Faraday Discuss.*, 123:287–302, 2003.